

POLITECNICO DI TORINO

Master's Degree in Ingegneria Elettrica



Master's Degree Thesis

Test bench development for PoC power transmission magnetic gears

Supervisors

Prof. Maurizio REPETTO

Dott. Luca DIMAURO

Candidate

Nicola LA BELLA

July 2022

Summary

Magnetic gears are a state-of-the-art technology developed in the literature only since few past decades. As the world moves more and more toward sustainability, this wear-free technology can truly be revolutionary. Many prototypes have been developed, and many more will be. This thesis work aims to provide a simple method to build a research environment that satisfies all the necessary requirements to study mechanical energy transmission prototypes, in such a way to be safe, versatile, and affordable. In the first part of the paper, the working environment is presented. It is of paramount importance to first know the object to be studied. Once the working environment boundaries have been defined, the choice of sensors, acquisition system and the rationale behind these choices are presented. Second part, on the other hand, is devoted to the results obtained from the constructed and functioning study system. The work presented is the result of a heterogeneous team composed of members coming from multiple fields of engineering. Many aspects have been analyzed, the solutions found are the result of years of previous studies, and they have all been crucial to the success of the project.

Acknowledgements

Questo per me è il capitolo più difficile della tesi. Non sono mai stato bravo ad esprimere sentimenti o affetto e dopo questi anni di Politecnico credo di essere addirittura peggiorato. Con ogni probabilità non avrò stampato la tesi quindi è possibile che questa pagina non venga mai letta, però mi sento in dovere di restituire qualcosa a tutti quelli da cui ho ricevuto.

GRAZIE

Grazie ai miei genitori, grazie ai miei fratelli, grazie a tutti i miei parenti. So di non essere stata una persona molto "semplice" con cui avere a che fare. Spero negli anni a venire di riuscire a trovare il modo di ripagare tutta la fiducia e il sostegno su cui ho da sempre potuto contare.

Grazie a tutti i miei amici, passati e presenti. Con ogni probabilità non sarei mai arrivato fino in fondo fossi stato da solo, non avrei avuto la motivazione necessaria per farlo. Spero di aver lasciato un'impronta in ognuno di voi perché voi in me l'avete fatto. Sono felice di essere sempre stato molto bravo a scegliere gli amici, ho avuto la possibilità di avere a che fare con persone davvero speciali. Forse ad alcuni dovrei dirlo più spesso e ad altri invece l'ho detto più del dovuto, ma spero dal profondo di aver compensato con i gesti quello non detto a parole.

Un grazie infine va' ad EDISU e al Politecnico di Torino, che mi hanno permesso di vestirmi, sfamarmi e viaggiare fin dall'altra parte del mondo. Grazie anche a molti docenti da cui ho potuto imparare molto sia riguardo alla vita che alla scienza. Una menzione speciale va al mio relatore, il professor Maurizio Repetto, il Dott. Luca Dimauro e al Dott. Paolo Squillari, senza i quali questo lavoro di tesi non sarebbe stato possibile.

Table of Contents

List of Tables	VII
List of Figures	VIII
Acronyms	XII
1 Introduction	1
2 Magnetic Gear	2
2.1 Theoretical framework	3
2.1.1 Mechanical basic operation	3
2.1.2 Magnetic gear working principle	5
2.1.3 Losses	7
2.2 Magnetic gear configuration	10
3 Study environment set up	17
3.1 Choice of the electrical drives	17
3.2 Sensors	19
3.2.1 Torsiometers	20
3.2.2 Encoders	21
3.2.3 Emf test coils	24
3.3 Gear shift mechanism	25
3.4 Switchboard project	28
3.5 Enactment of the project	32
4 Measurements and acquisition system National Instruments	35
4.1 cRio and acquisition cards	37
4.2 Elements of Sampling	38
4.2.1 Counters	38
4.2.2 Clocks	41
4.2.3 Counting frequency signals	42

4.2.4	Synchronization	44
4.3	Test bench LabView environment	44
4.4	Emf sensing coils	49
5	Static tests	51
5.1	DOE	52
5.2	Measurements results	54
5.2.1	Magnetic Flux Acquisition	54
5.2.2	No-load tests	55
5.2.3	Loaded tests	58
6	Dynamic tests	62
6.1	LabView control code editing	62
6.1.1	Ramp implementation	63
6.1.2	Continuous acquisition on file	64
6.2	Expected results	65
7	OpenReserarch	67
7.1	Magnetic gears geometry	67
7.1.1	Magnetic wheels	69
7.1.2	Ferromagnetic wheel	71
7.2	FEMM model	72
7.3	Measurements	74
7.3.1	Magnetic Flux Acquisition	75
7.3.2	No-load tests	76
7.3.3	Loaded tests	78
7.4	Conclusions	80
8	Conclusions	82
A	PoC MG construction tables	83
B	Software versions	88
	Bibliography	89

List of Tables

2.1	Current GearBox poles and transmission ratio configuration	11
3.1	Magnetic gear femm simulated capability results	17
3.2	SVTM A 03-11.5-107 manufacturer parameters declaration	18
3.3	AMK Inverter block parameters declaration	20
3.4	HBM T21WN torque transducer manufacturer parameters declaration	22
3.5	<i>LM10D01</i> – 15 speed transducer manufacturer parameters declaration	24
3.6	Magnetic flux’s measurement coils parameters	25
3.7	Stepper motor declared parameters	26
3.8	Stepper driver declared parameters	27
3.9	Stepper driver declared parameters	29
4.1	Input/Output signals parameters	36
4.2	NI modules declared features	38
4.3	NI modules declared features	41
4.4	Frequency count methods accuracy	41
5.1	Table of the DOE tests performed respectively to the MG possible configurations	53
7.1	MG magnets configuration and transmission ratio configuration . .	68
7.2	MG used materials	69
7.3	Magnetic gear femm simulated capability results	74
7.4	Table of the DOE tests performed respectively to the MG possible configurations	75

List of Figures

2.1	Many types of Magnetic gears developed in literature [1]	2
2.2	Example of mechanical planetary gear	4
2.3	Coaxial magnetic gear transmission example	5
2.4	Linearized section representation of magnetic gear working principle	5
2.5	Ferromagnetic poles contribution to Radial flux density B_r	7
2.6	Example of magnetic flux density norm and eddy current arrow plot resulting from 3D simulation.	8
2.7	Radial flux density B_r comparing 2D and 3D models	8
2.8	Power losses inner yoke, outer yoke, iron poles and permanent magnets power losses varying the rotational speed	9
2.9	Global efficiency, permanent magnets efficiency and specific iron loss plots varying the rotational speed. Highest specific losses are in the iron poles	10
2.10	Magnetic gear angular section's composition	11
2.11	2D planar finite elements MG model mesh plot	12
2.12	2D planar finite elements MG model solution	13
2.13	Four Femm 2d configurations: standard and gap between permanent magnets upside, splitted magnets with and without gap in the middle downside	14
2.14	Resulting Pareto front, value of α set accordingly to the color bar	15
2.15	Greyscale map of the sun-carrier torque upwards. Same torque value referred to the associated periodicity τ_r or τ_s , position of one rotor is fixed	16
3.1	Servotecnica SVTM A series. Two SVTM A 03-11.5-107 were picked	18
3.2	SVTM A 03-11.5-107 speed-torque map	19
3.3	HBM T21WN torque transducer	21
3.4	Renishaw Encoder sensor composition	23
3.5	A, B, Z signal example of the encoder. Resolution limit	24
3.6	Coils wrapped around ferromagnetic poles, phase shifted of around 120°	25

3.7	Stepper drive configuration manufactured at Sanyo Denki Co. Ltd.	26
3.8	Torque - pulses frequency map provided by the manufacturer	27
3.9	Stepper command timing example	28
3.10	Leakage inductance effect on the driver output current	28
3.11	Single line wiring diagram page 1	30
3.12	Single line wiring diagram page 2	31
3.13	Switchboard preliminary spacing of the components	32
3.14	Total project occupied space	33
3.15	Mounted test bench	33
3.16	Mounted switchboard	34
4.1	Example of common mode noise cut-off	36
4.2	National Instruments Compact RIO - 9045	37
4.3	NI acquisition boards	38
4.4	Control logic's of a counter	39
4.5	Single buffer acquisition method compared to circular buffer approach	40
4.6	Quantization error cases	40
4.7	Data flow scheme of the frequency signals [17]	42
4.8	Overview of some frequency torque signals samples	43
4.9	Flow chart of data, RAM and buffer memory usage	43
4.10	Internal common clock output	44
4.11	cRIO onboard project configuration and connections	45
4.12	Motor control - main VI, front panel	46
4.13	Motor control - main VI, block diagram	47
4.14	Acquisition - syncAcq VI, front panel	48
4.15	Motor control - syncAcq VI, block diagram	49
4.16	Example of sensing voltage acquisition	50
5.1	Radial and Tangential Flux, No torque load applied	55
5.2	Radial and Tangential Flux, Maximum torque load applied	55
5.3	Measured results, No-load applied, Gear 1 ,Multiplier configuration	56
5.4	Measured results, No-load applied, Gear 2, Multiplier configuration	57
5.5	Measured results, No-load applied, Gear 1 ,Reducer configuration .	57
5.6	Measured results, No-load applied, Gear 2 ,Reducer configuration .	58
5.7	MG's performance, T_1 torque on Sun side, Gear 2, Multiplier config- uration	59
5.8	MG's performance, T_1 torque on Sun side, Gear 1, Multiplier config- uration	60
5.9	MG's performance, T_2 torque on Ring side, Gear 2, Reducer config- uration	61

5.10	MG's performance, T_2 torque on Ring side, Gear 1, Reducer configuration	61
6.1	Ramp VI simple model. Front panel (up) and block diagram (down)	63
6.2	Continuous acquisition VI simple model. Front panel (up) and block diagram (down)	65
7.1	Geometric configuration of MG	68
7.2	Magnetic wheels construction example	69
7.3	Magnetic wheels dimensioned table and magnet partitioning	70
7.4	Carrier dimensioned table and ferromagnetic poles lamination . . .	71
7.5	2D planar finite elements MG model mesh plot	72
7.6	2D planar finite elements MG model solution	73
7.7	Radial and Tangential Flux, Gear 2, Reducer configuration	76
7.8	Measured results, No-load applied, Gear 2, Multiplier configuration	77
7.9	Measured results, No-load applied, Gear 2 ,Reducer configuration .	78
7.10	MG's performance, T_1 torque on Sun side, Gear 2, Multiplier configuration	79
7.11	MG's performance, T_2 torque on Ring side, Gear 2, Reducer configuration	80
A.1	PoC Magnetic Gear dimensioned tables page 1	83
A.2	PoC Magnetic Gear dimensioned tables page 2	84
A.3	PoC Magnetic Gear dimensioned tables page 3	84
A.4	PoC Magnetic Gear dimensioned tables page 4	85
A.5	PoC Magnetic Gear dimensioned tables page 5	85
A.6	PoC Magnetic Gear dimensioned tables page 6	86
A.7	PoC Magnetic Gear dimensioned tables page 7	86
A.8	PoC Magnetic Gear dimensioned tables page 8	87
A.9	PoC Magnetic Gear dimensioned tables page 9	87

Acronyms

DOF

Degrees of freedom

PoC

Proof of Concept

MG

Magnetic Gear

pp

poles pair

pm

permanent magnet

NI

National Instruments

DOE

Design of Experiments

Chapter 1

Introduction

Development and research are two topics that have been increasingly in vogue in recently. With a view to sustainability, efficiency and reduced consumption, the world is turning its eyes toward technological research.

In light of a new industrial revolution that sees an evolution of the mechanical world due to new studies in the field of electromagnetism, new technologies are appearing in the literature..

One disadvantage that is limiting this process lies on the materials required for the development of those systems: the mining process of rare earth minerals generates large amounts of toxic and radioactive material. This process must be done with extreme caution otherwise it could be harmful for the environment and human health.

Magnetic gears are a perfect example of the mechanical world's revolution: starting from a very well known mechanism, a new version of it has been designed with the purpose of increasing its efficiency and durability.

Efficiency calculus is the ultimate goal of this work. In order to test the PoC prototype of the Magnetic Gear produced within the Politecnico di Torino, it was necessary to set up a test bench starting from scratches. This involved to be fully aware of the prototype, with its limitations and strengths.

Regarding the complexity of the task, it was necessary to put to use all the knowledge acquired during the previous years of study, without which the job couldn't be completed.

Development phase required to make use of the theoretical knowledge of mechanics and electromagnetism for the first part. Ability to relate to manufacturers and suppliers during the construction phase. Flexibility and speed of learning to operate on the National Instruments system. Ability to analyze data and produce effective post-processing results to describe the actual behavior of the studied object.

As such, this article is assumed to be a simple and reliable guide to build a test bench for testing innovative state-of-the-art mechanical mechanisms.

Chapter 2

Magnetic Gear

As explained in section 1, this work is focused on the realization of a test bench for the study and validation of the theorized functionality design of a magnetic gear. In order to do this it is first necessary to know the gear system, then it is possible to define what the quantities of interest are and understand its physical limits. Only after that a suitable test and acquisition system for this application can be designed.

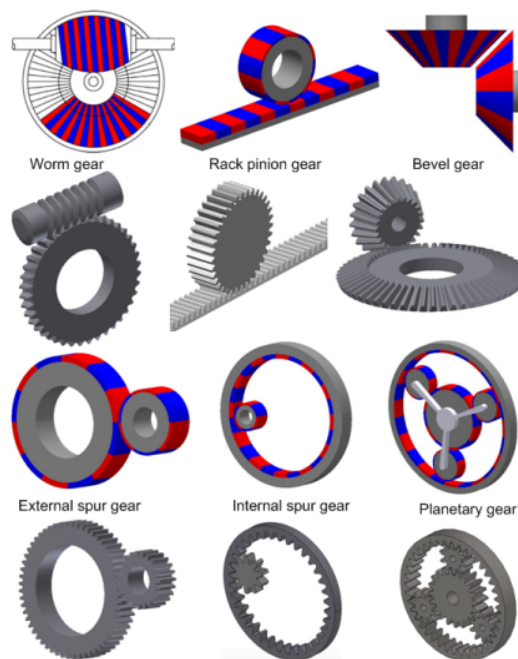


Figure 2.1: Many types of Magnetic gears developed in literature [1]

The transmission of mechanical energy has always been a topic of interest in the industrial field, subject of many studies and investigation. This type of systems is very useful to transfer kinetic energy, in form of speed and torque.

Despite the very high efficiency, those mechanisms are certainly not immune to wear and tear or overheating. This implies the necessity to use lubricants and do maintenance in order to ensure their optimal operation.

Magnetic gears are the natural evolution of mechanical transmissions: exchange and transformation of the motion are no longer addressed to mechanical parts, but to magnets. Few examples are shown in Figure 2.1 This not only makes the mechanics almost wear-free, but should be able to raise the efficiency further once the steady-state condition is reached.

This is the reason why these solutions over the past few years have found application in many compartments, where a greater air-tightness is needed to prevent the infiltration of liquid, gaseous, polluting, toxic or aggressive substances.

2.1 Theoretical framework

In this section all the aspects of a gear are analyzed. Firstly the canonical mechanic version, by means of all the theories developed up to date; leading up to more recent theories and studies. Some simplifying assumptions were made, in order to carry out the project without complicating the computational steps and numerical burden more than necessary.

2.1.1 Mechanical basic operation

A mechanical transmission makes use of a series of gear wheels placed in contact with each other. Each of these cogs has a diameter and number of teeth specifically chosen so that it can transmit the magnitudes "speed" and "torque" suitably to the application.

Mechanical gears are divided into two further groups: ordinary and planetary: meanwhile into the ordinary one the gear axes are always in the same position, the planetary one allows axes to move spatially. Usually the latter has a fixed geometry as shown in Figure 2.2, composed by:

1. Sun gear
2. Planetary gears
3. Ring gear
4. Carrier gear which connects the planetary ones

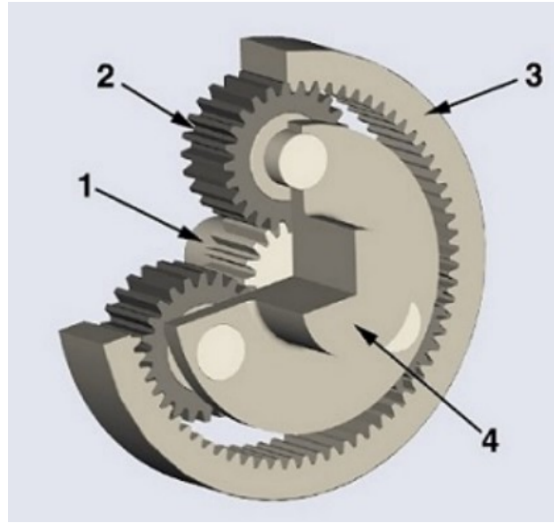


Figure 2.2: Example of mechanical planetary gear

The usual notation used for this type of mechanism refers to the speed of the wheels. Therefore, a gear ratio is defined as τ , which is given by the ratio of the coupled wheels' speed. Referring to 2.1 it's set ω as the wheel speed and Z as the number of teeth.

$$\tau_{in/out} \triangleq \frac{\omega_{in}}{\omega_{out}} = \frac{Z_{in}}{Z_{out}} \quad (2.1)$$

Initially simplifying the physics of the object, it is possible to make use of the "Willis formula", which summarizes the 2 DOF of the gear within a kinematic formula, see (2.2).

$$\omega_1 = \omega_s \quad \omega_3 = \omega_r \quad \omega_4 = \omega_c$$

$$\tau_{s/r} = \frac{\omega_s - \omega_c}{\omega_r - \omega_c} = \tau_{s/p} \cdot \tau_{p/r} \quad (2.2)$$

When designing this type of gear, therefore, the number of teeth is adjusted in order to change the gear ratio τ .

One last preliminary caution to consider is wear. With integer gear ratios there will always be uneven wear of the wheels, since they do not always have the same number of teeth. To get around this problem, a mathematical property suffices: by choosing Z as a prime number, wheel wear will always be homogeneous into the gear.

2.1.2 Magnetic gear working principle

Initially, a planetary model was suggested in the literature by C.Huang in 2004. It has a strong limitation on the torque transmission, that's the reason why this study is more concerned on a coaxial version, shown in Figure 2.3, of the model developed by K.Atallah and D.Howe. [2]

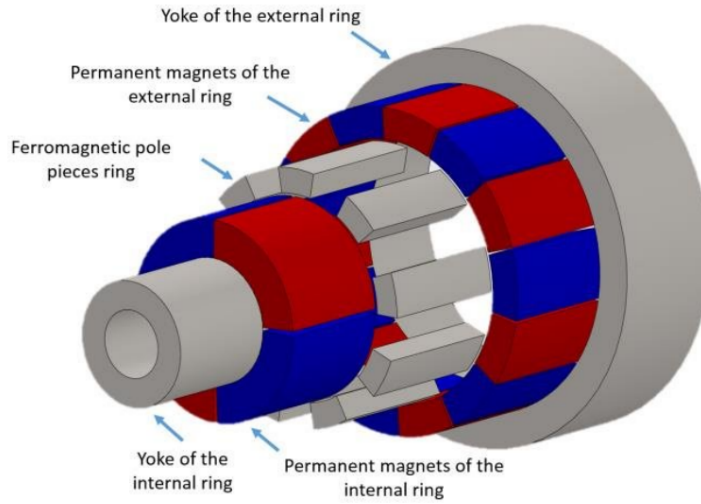


Figure 2.3: Coaxial magnetic gear transmission example

It consists of an inner rotor and an outer rotor. Each rotor has a different number of permanent magnet pp. A certain number of ferromagnetic poles are located between the two rotors. The inner rotor is the high-speed one, while the outer rotor runs at lower speed. Ferromagnetic poles (central rotor) are fixed and modulate the magnetic fields produced by the inner and outer rotors in such a way to create spatial harmonics all along the air gaps. The magnetic fields modulated through the steel poles interact with the magnetic field on the other side to transmit motion.

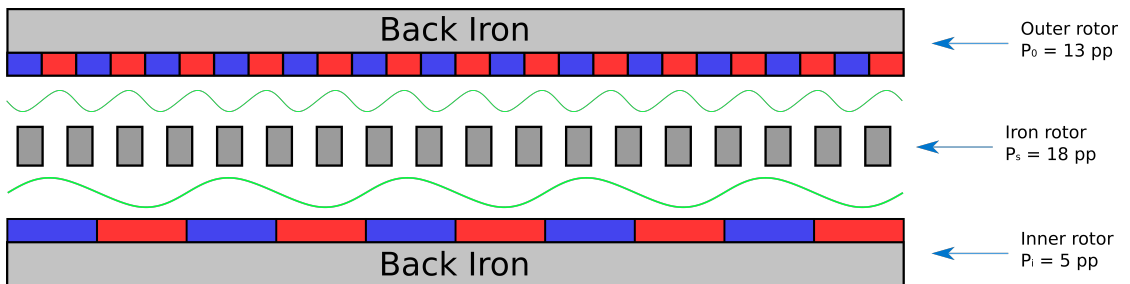


Figure 2.4: Linearized section representation of magnetic gear working principle

Figure 2.4 shows the working principle of a linear magnetic transmission. Notice that same holds for any other type of geometry, such as axial or coaxial. Depending on the number of magnetic pp embedded, an n^{th} harmonic of magnetic field is generated by the inner wheel, modulated by the iron one and finally transformed into a different frequency one, consequently to the outer wheel pp number. The example provided has a 5 pp of magnets on the lower side; that means a dominant 5^{th} harmonic of magnetic field. Such field is then modulated by the 18 ferromagnetic pp to be transformed into a 13^{th} harmonic field. This process generates torque, being that the transformed field coming from the inner wheel is congruent to the outer wheel one.

Magnetic field can be analytically calculated on each magnet. Literature provides us a closed formula for the magnetic flux density distribution B at a radial distance r , separating radial 2.3 and circumferential 2.4 effect.

$$B_r(r, \theta) = \left(\sum_{m=1,3,5\dots} b_{rm}(r) \cos(mp(\theta - \Omega_r t) + mp\theta_0) \right) \times \left(\lambda_{r0}(r) + \sum_{j=1,2,3\dots} \lambda_{rj}(r) \cos(jn_s(\theta - \Omega_s t)) \right) \quad (2.3)$$

$$B_\theta(r, \theta) = \left(\sum_{m=1,3,5\dots} b_{\theta m}(r) \sin(mp(\theta - \Omega_r t) + mp\theta_0) \right) \times \left(\lambda_{\theta 0}(r) + \sum_{j=1,2,3\dots} \lambda_{\theta j}(r) \cos(jn_s(\theta - \Omega_s t)) \right) \quad (2.4)$$

In both equations there are two sides: the first part represents the flux density as long as no ferromagnetic pole pieces are involved; the second part is the "modulating formula", thanks to which ferromagnetic poles are involved. p stands for magnetic pole pairs of the rotor, n_s is the number of ferromagnetic pole-pieces. b_{rm} and $b_{\theta m}$ are Fourier coefficients for the radial and circumferential components of flux density without the ferromagnetic pole-pieces.. Similarly, λ_{rj} and $\lambda_{\theta j}$ are Fourier coefficients for the modulating functions, useful to include the radial and circumferential components of the flux density distribution related to the introduction of the ferromagnetic pole-pieces. [3] Simulations carried out in literature show a strong influence of the ferromagnetic poles on the flux density value at a fixed radial distance, depending on the rotation speed as expected. An example is shown in Figure 2.5.

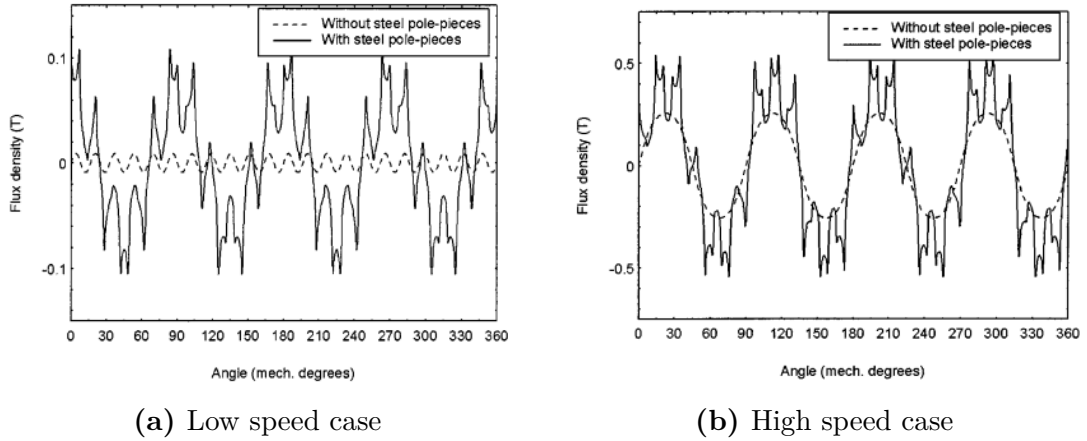


Figure 2.5: Ferromagnetic poles contribution to Radial flux density B_r

2.1.3 Losses

Losses valuation of a component is a key part within a project. Such preliminary studies prevent are necessary in order to understand whether a project can be competitive and thus commercialized or not. In this case only magnetic losses are investigated, since newer models have been recently developed and therefore are of greater academic interest.

Analytical models were coupled with finite element models in order to obtain the most accurate results possible. It remains to be seen whether a simple 2D model can be sufficiently accurate or whether it was necessary to implement one in 3D. This may seem like a trivial choice, but it is actually an essential choice to be made upstream of a geometry optimization process.

Different methods can be exploited: a 2D model can be based on Maxwell quasi-static laws, neglecting eddy currents effects due to iron non-linearity; standard 3d model formulations are instead based on the magnetic vector potential A and on the scalar electric potential V .

Eddy currents can also be very influential in a magnetic system, as well as a cause of demagnetization of permanent magnets if not taken into account. It can be seen an example of magnetic flux distribution in the GearBox together with eddy currents in Figure 2.6.

As the system losses vary, the fluxes involved also vary consequently, so the difference between models was studied in the literature in order to decide whether the error made was acceptable or not. Most of the losses are located into the ferromagnetic poles, being the flux density mostly concentrated there to obtain the rotational effects.

The most important effect is shown in Figure 2.7 that highlights the losses effect

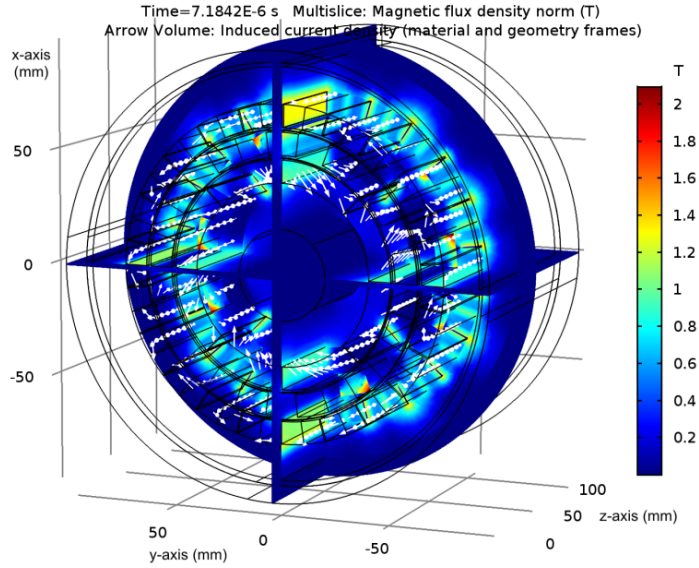


Figure 2.6: Example of magnetic flux density norm and eddy current arrow plot resulting from 3D simulation.

on flux comparing 3D and 2D models.

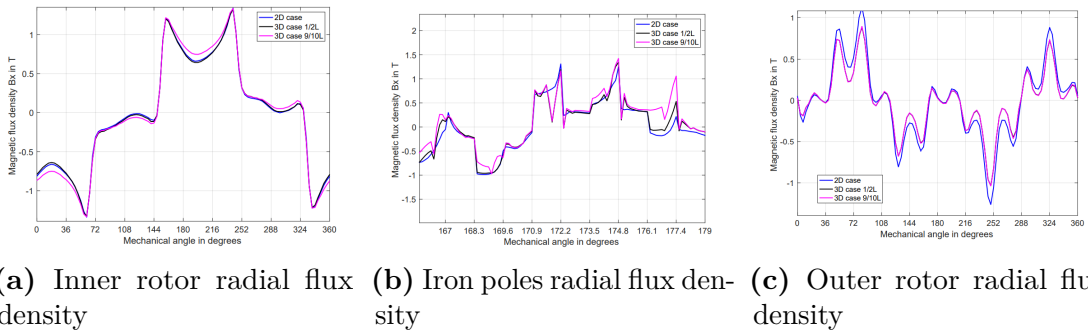


Figure 2.7: Radial flux density B_r comparing 2D and 3D models

In each plot three curves are displayed, one for the 2D and two for 3D cases. Being the 3D model more complex, there might be deviations depending on the position under analysis, that's the reason why flux lines were provided for both the middle and the almost-end of the gear, described in the graph respectively as $z = L/2$ and $z = 9L/10$.

A method based on losses separation for the 2D case is provided by the statistical theory of loss of Bertotti. Total loss W is expressed as the sum of the hysteresis W_{hyst} , excess W_{exc} , and classical W_{class} components, as stated in (2.5).

$$W = W_{hyst} + W_{exc} + W_{class} \quad (2.5)$$

However, it is necessary to consider that the eddy current losses are closely related to the rotational speed, similarly to the electric machines, as well as the load angle θ_L . Therefore, it is considered necessary to further develop the study to estimate the influence of every loss contribution in the efficiency calculus.

Without going too deep into model description, not much of interest within this discussion, the results obtained from its application are presented. First of all, it can be seen in Figure 2.8 how the losses are distributed within the gear: Inner yoke losses are negligible in relative terms. The highest specific loss is obtained in the iron poles, as expected, being those elements subject to the highest magnetic induction at the highest harmonic content.

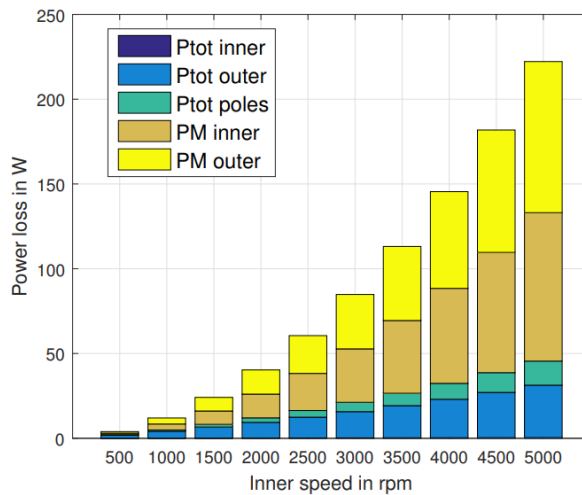


Figure 2.8: Power losses inner yoke, outer yoke, iron poles and permanent magnets power losses varying the rotational speed

A map of global and permanent magnet efficiency at varying applied speed is presented in figure 2.9. The graph is accompanied by the losses of the various portions of the system. It can be seen how the efficiency decays practically linearly once the 1000rpm threshold is exceeded; the greatest losses in specific terms are found in the iron poles, as previously mentioned.

To conclude, magnetic gear is modeled through the finite element method and the equations for the loss calculation with rotational flux loci were discussed. The comparison between 3D and 2D simulations confirmed that the use of a 2D model for finite element calculations is a sufficiently good approximation. So because of this conclusion, an algorithm might be used to optimize the geometric factors of the rotor-craft. [4]

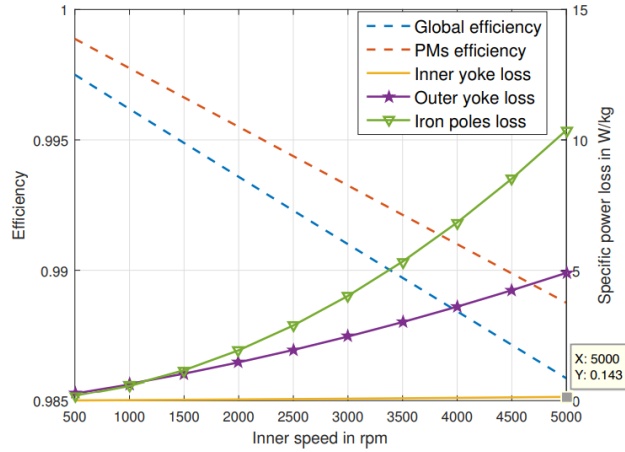


Figure 2.9: Global efficiency, permanent magnets efficiency and specific iron loss plots varying the rotational speed. Highest specific losses are in the iron poles

2.2 Magnetic gear configuration

As shown in Figure 2.10 this magnetic gear is composed by a sun, a carrier and a ring wheel. [4]

Both inner and outer hubs consist of a series of rare-earth permanent magnets that are ground, encapsulated, and bonded to the steel hubs. The middle one, the carrier, is instead made of a plastic material and contains the ferromagnetic poles. By actuating one disk, the torque is transmitted magnetically to the other. The process can be done through air or through a containment barrier made of nonmagnetic material such as stainless steel or fiberglass, allowing complete isolation of the inner magnetic disk from the outer magnetic disk. The parts do not come into contact.

Hence, in order to size the test bench, it is necessary to get a little more specific about the MG. First of all it is a coaxial magnetic mechanism; the only mechanical parts subjected to wear and tear are some bearings. Those are necessary to ensure the relative motion of the wheels. The whole item consists of 2 gear ratios of motion transmission, and it is also possible to use it as a speed reductor same as a multiplier based on whether the supply side is the sun or ring side.

The two ratios of transmission are achieved by coupling a different number of magnetic poles through the same carrier, so gear shifting is done by moving the carrier between pairs in such a way as to "enable" or "disable" the transmission of magnetic flux, and thus motion. Current configuration is described in Table 2.1. [5]

As explained in section 2.1.3, for validation of the design and current configuration 2D finite element calculations were carried out using Octave Femm

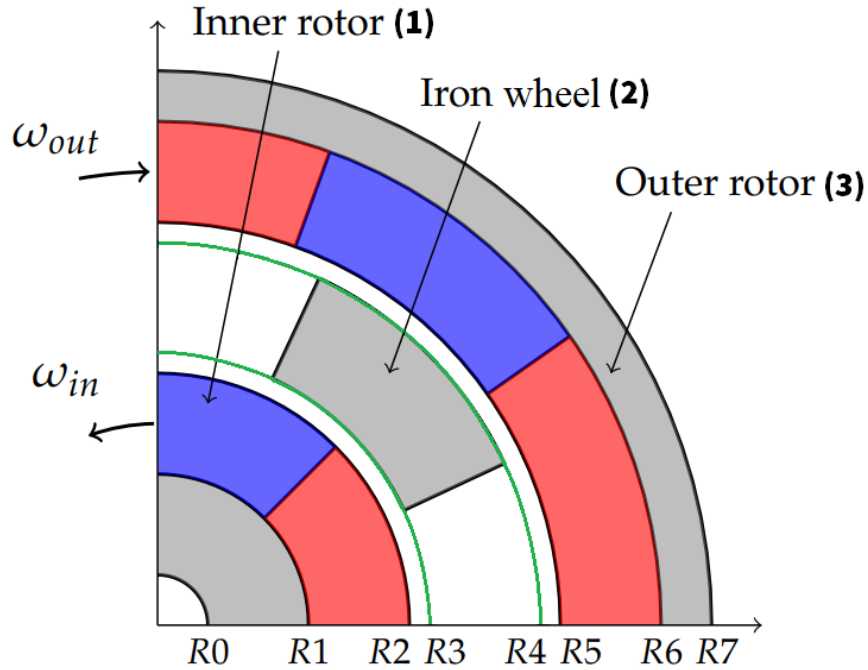


Figure 2.10: Magnetic gear angular section's composition

Gear 1 $\tau_{r/s}$	2.6
Gear 2 $\tau_{r/s}$	1.57
Magnetic Sun wheel pp	[5 ÷ 7]
Magnetic Ring wheel pp	[13 ÷ 11]
Ferromagnetic Carrier wheel pp	18

Table 2.1: Current GearBox poles and transmission ratio configuration

software.

In Figure 2.11 a 2D planar model is proposed. For this to be as reliable as possible, it is necessary to include within the software the specifications of the materials that make up the mechanism: from the steel yokes, to the magnets hooked onto them, to the ferromagnetic poles that modulate the flux. For what concerns non-magnetic materials it is not necessary to implement a custom magnetization curve: those behave very similarly to air.

The most difficult part of these kinds of models is making a good mesh. This must be a compromise between numerical burden on the computer and at the same time accuracy of the results. As shown in Figure 2.11, the mesh made is mixed: at

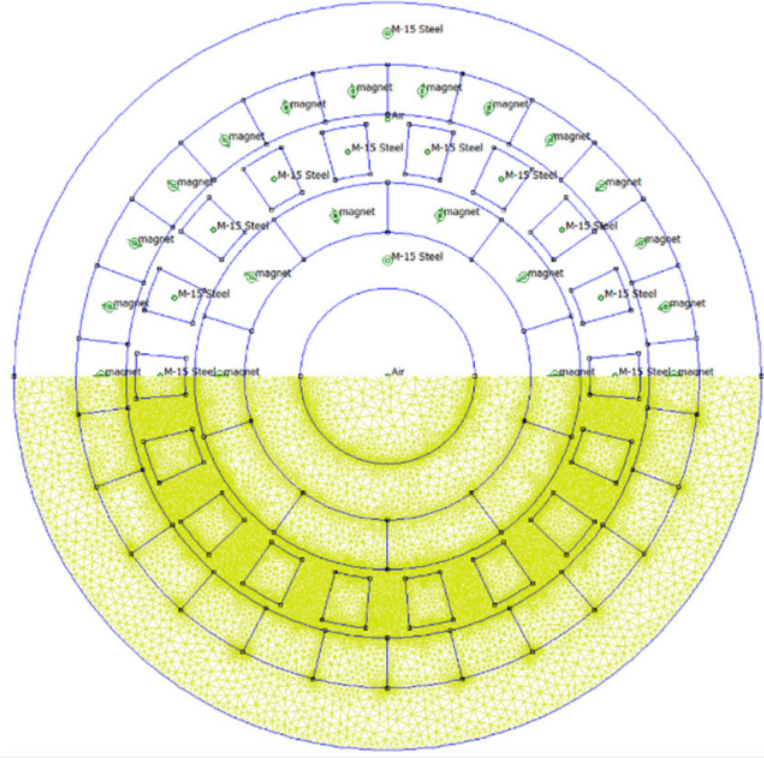


Figure 2.11: 2D planar finite elements MG model mesh plot

the points of greatest interest, such as air gaps and edges, it is finer; for the other inner points it is more relaxed. Doing so it is given a very good approximation of the operation in a relatively short time. This aspect is also crucial from an optimization perspective, for which it may be necessary to iterate the same model many times to obtain satisfactory results.

In order to solve a magnetostatic problem, the software makes use of two fundamental laws: Gauss's law for magnetism (2.6) and Ampere's law (2.7). [6]

$$\nabla \cdot B = 0 \quad (2.6)$$

$$\nabla \times H = J \quad (2.7)$$

It is furthermore fundamental to know the simple relationship (2.8).

$$\mu = \frac{B}{H(B)} \quad (2.8)$$

Femm, in order to satisfy (2.7) and (2.8), uses a vector potential A approach solving for the flux density B, see (2.9).

$$B = \nabla \times A \quad \longrightarrow \quad \nabla \times \left(\frac{1}{\mu(B)} \nabla \times A \right) = J \quad (2.9)$$

Assuming a linear isotropic material, $\nabla \cdot A = 0$, (2.9) can be further reduced into (2.10). At this point, non-linear B-H relationships can be solved.

$$-\frac{1}{\mu} \nabla^2 A = J \quad (2.10)$$

It not a strong assumption to consider the MG as composed by linear isotropic materials. That leads to the model's resolution.

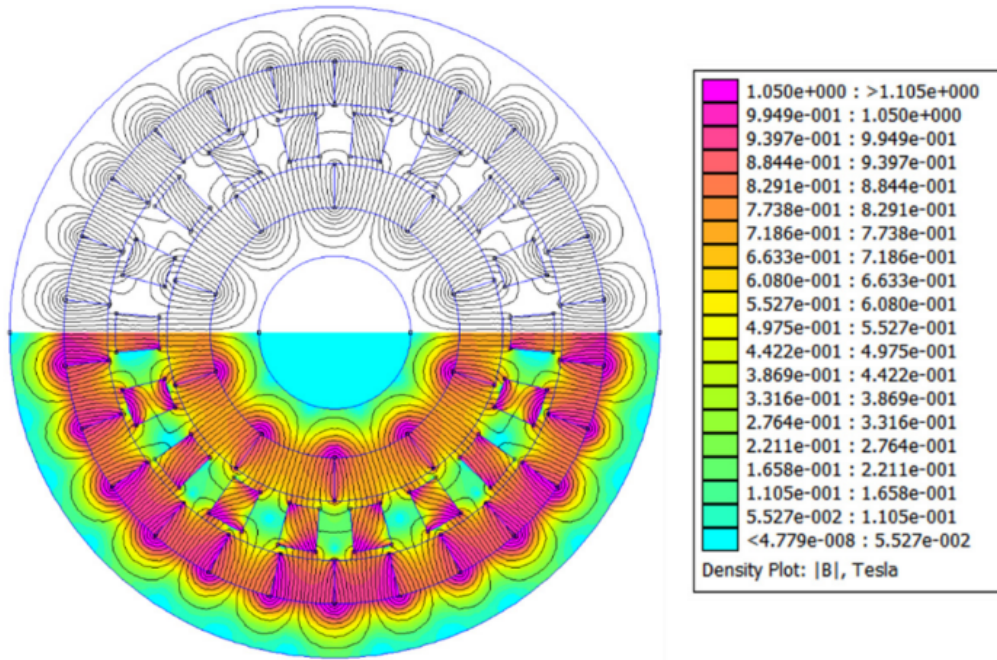


Figure 2.12: 2D planar finite elements MG model solution

The solution of this simulation is shown in Figure 2.12. In the upper part of the figure, the flow lines and their passage are highlighted in blue. In the bottom part, via a colorbar, the saturation level of the magnetic materials is shown. As was desirable, the points most prone to saturation are the edges between the magnets and the ferromagnetic poles. It can be appreciated, however, that it appears from the simulation that the Sun wheel magnets are less stressed than the Ring. At the same time, as was desirable, the steel yokes appear to be affected only in the portions most in contact with the magnets.

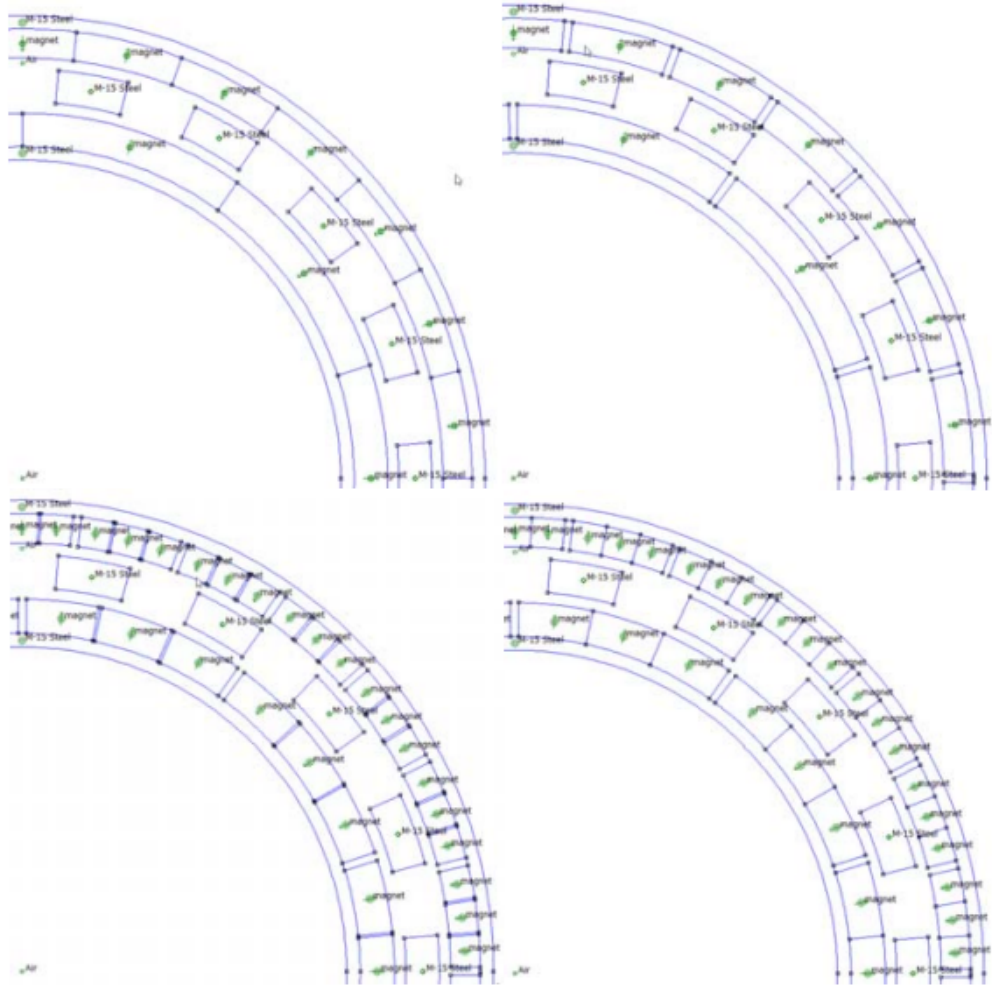


Figure 2.13: Four Femm 2d configurations: standard and gap between permanent magnets upside, splitted magnets with and without gap in the middle downside

The geometric parameters were then incorporated within an optimization process, see Figure 2.13. With the goal of maximizing the torque density of the gear then, a multi-objective function was laid out that included the torque density and inertia of the object, see (2.11) All geometric measurements were varied except from the air gap, imposed as a construction constraint. [7]

$$f(T_\rho, J_{eq}) = \max \left[\alpha \frac{T_\rho}{T_{\rho_{ref}}} - (1 - \alpha) \frac{J_{eq}}{J_{eq_{ref}}} \right] \quad (2.11)$$

T_ρ and J_{eq} are respectively the torque density and the equivalent moment of inertia of the system calculated geometrically; T_ρ and J_{eq} are instead used

to normalize the two components of the objective function. By means of the variation of the parameter α the function is maximized. In order to understand the effectiveness of the improvements and to actually decide which solution found is the best, it was made use of the Pareto front. Variation of the parameter α can be plotted as in Figure 2.14 and corresponding value of calculated mass M and maximum torque T_{sc} are also reported.

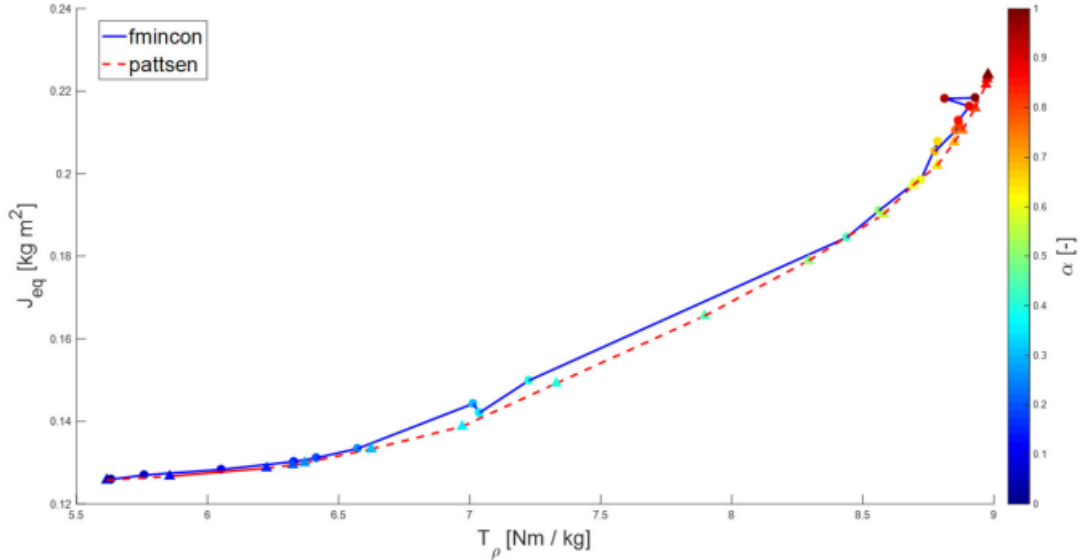


Figure 2.14: Resulting Pareto front, value of α set accordingly to the color bar

Another aspect to be considered regards the torque, being not always constant but still dependent on the position of the three magnetic parts time by time. Numerical calculation can be performed to evaluate torque value for a significant number of angular positions. Under the hypothesis that the steel pole pieces are fixed, each configuration is identified by the angle of the sun θ_s and that of the ring θ_r . The discretization of these two angles should be tiny enough to have a good reconstruction of the torque. The map of the torque as function of θ_s and θ_r for $n_s = 5$ and $n_r = 18$ is posted on Figure 2.15.

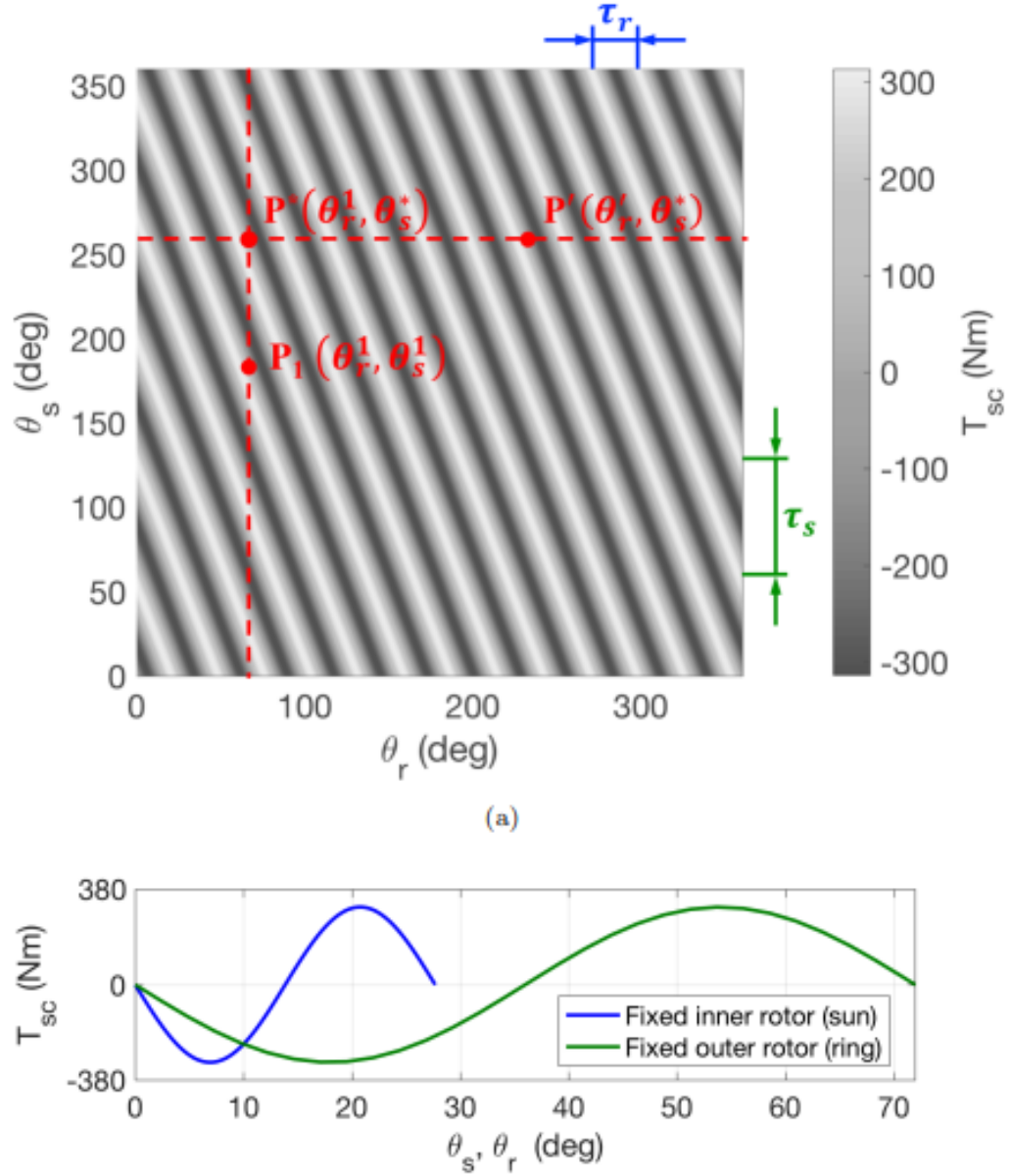


Figure 2.15: Greyscale map of the sun-carrier torque upwards. Same torque value referred to the associated periodicity τ_r or τ_s , position of one rotor is fixed

Chapter 3

Study environment set up

To properly choose the motors it is first necessary to understand the physical limits of the Gearbox. Dimensioning so far has been made in order to maximize the Torque density T_ρ . As explained in section 2.2, results shown in Table 3.1 were carried out by finite elements simulation.

Femm simulation results	Value	Unit
Torque inner rotor (sun) T_{sc}	[2.09 3.02]	Nm
Torque outer rotor (ring) T_{cr}	[5.44 4.74]	Nm
Torque carrier T_c	-[7.53 7.76]	Nm
Weight $m_M G$ (single stage)	0.62	kg
Torque density T_ρ	3.36	Nm/kg

Table 3.1: Magnetic gear femm simulated capability results

3.1 Choice of the electrical drives

In order to study the mechanism to its full potential, it is necessary to choose motors capable to continuously deliver more than the maximum torque allowed by the GearBox. The choice went to two brushless motors manufactured by Servotecnica, see Figure 3.1

The SVTM A series present a type IC 400 construction, which means the motor is totally enclosed and does not need any kind of additional ventilation, and IP65 certified. Neodymium magnets were adopted to ensure high performance and small dimensions, resulting in a sinusoidal electromotive force. Drives are equipped with an internal temperature sensor, mounted on each winding so as to prevent damage



Figure 3.1: Servotecnica SVTM A series. Two SVTM A 03-11.5-107 were picked

from overheating and consequently increasing motor service life. For motor control is also provided a built in Hall-effect incremental encoder, which provides the feedback signal to the inverter. Motor parameters are listed in Table 3.2. [8]

Parameter	Value	Unit
Motor length (L)	218	mm
Nominal voltage V_{DC}	560	V
Continuous stall torque	11.5	Nm
Continuous stall current	6.85	Arms
Nominal torque	9.3	Nm
Nominal current	5.54	Arms
Nominal speed	2800	rpm
Peak torque	30	Nm
Peak current	21	Arms
Torque constant k_T	1.68	Nm/Arms
BEMF constant k_E	107	V _{rms} /krpm
Rotor inertia	10.8	kgcm ²
Thermal protection	PTC	°C
Mass	9.5	kg

Table 3.2: SVTM A 03-11.5-107 manufacturer parameters declaration

To be aware of the motor's torque potential relative to the required speed, the manufacturer also provides a speed-torque map for both S1 and S3 service. As can

be seen in Figure 3.2, it is allowed to exceed the rated speed up to about 3400 rpm provided that the torque output is sacrificed.

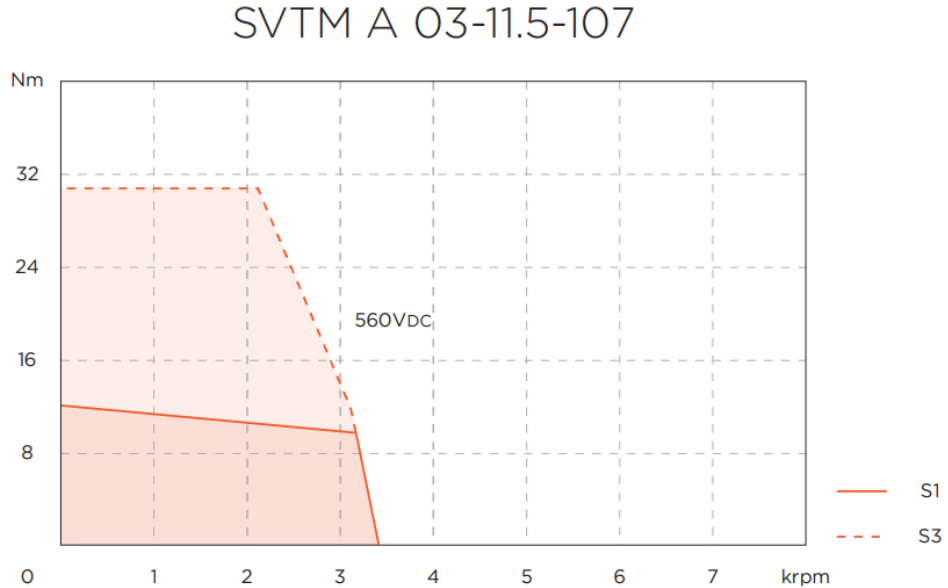


Figure 3.2: SVTM A 03-11.5-107 speed-torque map

In order to properly control the motors, it is necessary to have a suitable inverter. The choice fell on the model recommended by the manufacturer along with the purchase of the motors. The inverter block is modular and consists of several pieces assembled together:

- One power supply KEN 5 - 0N
- One inverter block KWD 5
- Two control boards KW - R25
- One decoupling reactor ALN12

Parameters of interest are listed in Table 3.3. [9]

The assembled block in connects via EtherCAT protocol to the National Instruments system that provides real-time control parameters.

3.2 Sensors

Matter of fact, choice of sensors is the most important part of this thesis. The primary goal of the test bench is the capability to precisely test the functionality

Parameter	Value	Unit
Input voltage	3 x 400	VAC
Input frequency	[47 ÷ 63]	Hz
Input current	12	A
Services input voltage	24	V
DC link voltage	540	V
DC link current	9.25	A
Weight	2.5	kg

Table 3.3: AMK Inverter block parameters declaration

of the magnetic gear, but if the accuracy and resolution of the sensors were not adequate, the construction of the bench would be completely useless. Therefore, in the following sections a detailed explanation of the process of selection for each sensor is given.

Primarily, it is necessary to investigate the mechanical operation of the magnetic gear, which means to find a way to convert mechanical quantities such as torque and angular velocity into measurable quantities. To do so, therefore, it is first necessary to discretize the two so that a digital sampling process can be carried out, which will later be transmitted and processed within the acquisition environment. Secondly, it is the time of magnetic measurements. The magnetic flux circulating within the mechanism is also not directly measurable, but thanks to the effect of the induced electromotive force, it can be achieved indirectly by isolating the mechanical quantities on which it depends.

3.2.1 Torsiometers

Torque measurement is one of the most complex measurements to derive. As said before, is not directly measurable but still the greatest disadvantages are due to sensors: the relative influence on the measure is not negligible and measuring instruments are very fragile and susceptible to pulses.

The effect of sensors on the measurement is a known problem. For what concerns torque transducers, it is a particularly relevant effect to consider. When a torque is applied to the sensor shaft, commensurately with the elasticity of the material, undergoes torsion. This effect causes an angular displacement to occur between shaft ends. Since the problem is well known it can be limited or, basing on the application field, compensated.

For what concerns this particular application field, two different torsiometers are needed. As shown in Table 3.1, torque applied on one side of the MG is different to

the other side, by a factor almost equal to the gear ratio. Maximum difference of torque is expected on Gear 1, as the expected transmission coefficient is $\tau_{r/s} = 2.6$; see Table 2.1.

Therefore, the choice came down to two torque transducers from the manufacturer HBM, one with a maximum applicable torque of $5Nm$ and the other of $10Nm$. An image of the sensors is provided in Figure 3.3



Figure 3.3: HBM T21WN torque transducer

The characteristics of those particular models make it particularly suitable for carrying out torque measurements for MG since the low linearity deviation, excellent measurement resolution, high stability in data transmission thanks to the differential mode signal transmission, and low angular displacement due to torsion. Such informations are summarized in Table 3.4

For greater stability of the signal to be measured, the digital frequency output of the sensor is used. Voltage output would first require an analog signal receiver, not to mention that it would be greatly affected by the length of the cable and may be more prone to electromagnetic interference.

This torque transducer also provides a simple measure of speed, by means of an optical encoder. For the particular case this solution is not acceptable since it is needed an incremental encoder to latch the torque ripple on to, meanwhile the built in encoder is a relative one. Furthermore it has a very low resolution (only 360 pulses per revolution). That's the reason why it is necessary to choose an external speed measurement sensor. [10]

3.2.2 Encoders

Since the speed sensor embedded into the torque transducer is not sufficient, it is necessary to choose another suitable speed transducer. Thus, the key features this new component must include are:

- Incremental measurement;

Parameter	Value	Unit
Precision class	0.2	
Nominal torque	[5 10]	Nm
Nominal speed	19000	rad/s
Relative deviation of linearity including hysteresis	$> \pm 1$	%
Frequency output	[5 ÷ 15]	kHz
Output frequency for $T = 0$	10	kHz
Voltage output	[-10 ÷ 10]	V
Output voltage for $T = 0$	0 ± 0.05	V
Frequency resolution	0.19	Hz
Voltage resolution	0.38	mV
Voltage source	24	V
Weight	0.6	kg
Nominal temperature	[+5 ÷ +45]	$^{\circ}C$
Torsion angle at M_{nom}	[0.32 0.3]	deg

Table 3.4: HBM T21WN torque transducer manufacturer parameters declaration

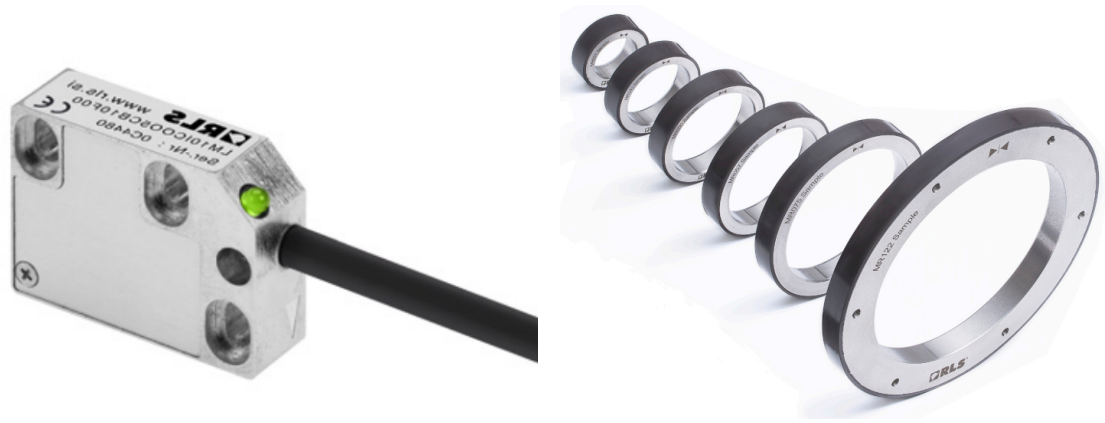
- Referee pulse so to trigger the Torque ripple measurement;
- Good angular resolution

The choice fell on two encoders (one on each side) made by Renishaw; see Figure 3.4.

The LM10 is a contactless high-speed magnetic encoder designed for linear or rotary motion sensing in harsh environments. The LM10 features a compact sealed readhead that rides at up to 1.0 mm from the self-adhesive magnetic scale or ring. Simple to install, the LM10 features an integral set-up LED, wide installation tolerances. A bidirectional reference is provided that can be actuated either by a preset mark integrated within the scale or ring or by adding a reference sticker on top of the scale with the help of a self-aligning installation tool. The non-contact, frictionless design eliminates wear while reducing hysteresis. The LM10 encoders bring reliable solutions to tough, hard-working applications. [11]

In order to function properly, the encoder needs a ferromagnetic wheel, shown in Figure 3.4. This, as it rotates, causes the measurement to come out of the sensor congruently.

Also for what concerns this sensor a frequency output for the signal transmission is used. Since the resolution of the measurement is fixed, frequency may vary a



(a) Renishaw *LM10D01* – 15 incremental magnetic encoder (b) RLS *MR02D01* – 02 incremental magnetic ring

Figure 3.4: Renishaw Encoder sensor composition

lot. It is not possible to consider an infinite range of frequency for the acquisition system, it is so necessary to define an upper and lower bound. First it is necessary to know how many pulses per revolution the sensor may output. The manufacturer declares a formula to calculate this value to be (3.1).

$$Resolution = \frac{n_P \cdot k_{int}}{4} = \frac{160 \cdot 32}{4} = 1280ppr \quad (3.1)$$

n_P is the number of magnetic poles on the wheel, the k_{int} is the coefficient of interpolation and it is different basing on the chosen sensor. Once known the ppr value, it is immediate to define an upper bound of frequency to acquire since the nominal speed of the motors is known to be $\omega_N = 2800rpm$. That means the maximum frequency of the signal can be calculated as (3.2)

$$f_{max} = \frac{1280ppr \cdot 2800rpm}{60s} \approx 60kHz \quad (3.2)$$

A summary of the main characteristics of this model is provided in Table 3.5

Like many encoders, there are three output signals: A, B and Z. For greater stability, these signals are sent in differential mode. That means dealing with twice as many signals, which are therefore A+, A-, B+, B-, Z+, Z-.

Every signal is a square wave and the resolution is due to the edge separations of the A and B signals, as shown in Figure 3.5

Parameter	Value	Unit
Power supply	[4.7 ÷ 7]	VDC
Response time	<10	μs
Signal level High UH	≥ 2.5	V
Signal level Low UL	≥ 0.5	V
Switching time (10% to 90%)	<30	ns
Max cable length	100	m
Nominal temperature	[-10 ÷ +80]	$^{\circ}C$
Maximum expected output frequency	60	kHz

Table 3.5: LM10D01 – 15 speed transducer manufacturer parameters declaration

Timing diagram

Complementary signals not shown

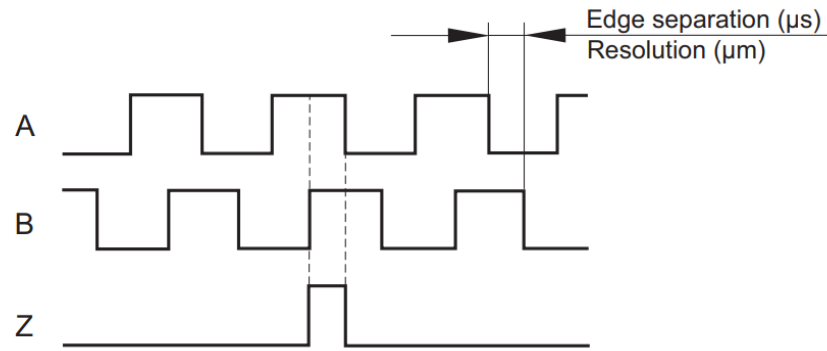


Figure 3.5: A, B, Z signal example of the encoder. Resolution limit

3.2.3 Emf test coils

Once the measurements of mechanical quantities have been defined, it is the turn of magnetic measurements. Unlike the mechanical ones that can be made once the prototype's "box" is "closed," it is not possible to see the magnetic flux from the outside. The only way is to wrap coils on the ferromagnetic poles of the carrier. By exploiting Faraday Lenz's law, it is possible to obtain an electromotive force applied to the two ends of each coil in the presence of varying magnetic flux. The magnetic flux is static when the mechanism is stationary, however, it becomes variable while the prototype is rotating. On this principle is based what is done in Figure 3.6, are in fact placed six coils on the carrier, three able to concatenate the tangential and three the radial flux respectively.

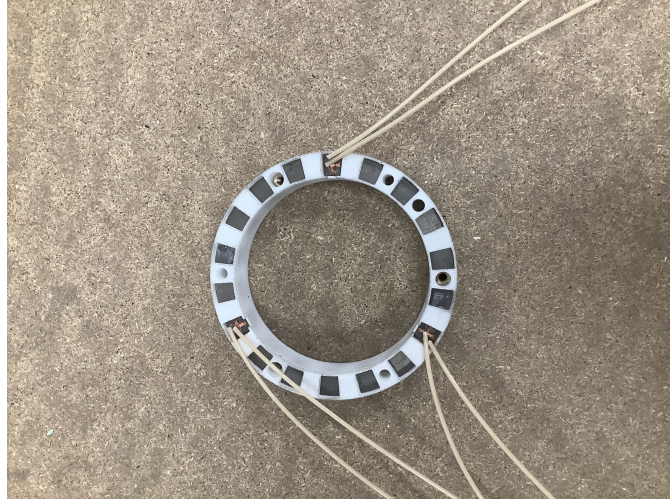


Figure 3.6: Coils wrapped around ferromagnetic poles, phase shifted of around 120°

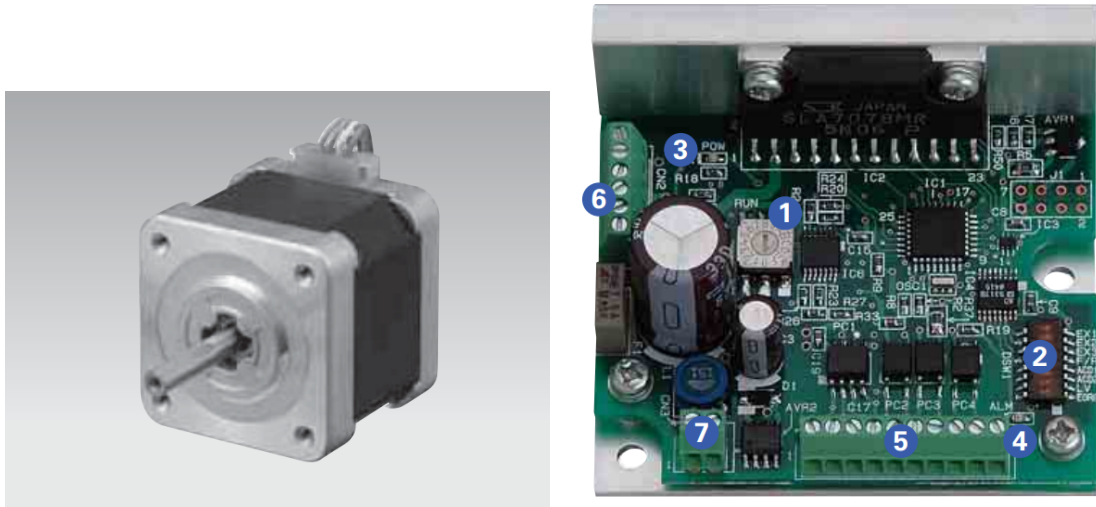
As for the other sensors, the values of interest are summarized in Table 3.6.

Parameter	Value	Unit
Angular position shift	120	deg
Winding number N	18	turns
Wire resistance R	17	Ω
Cross section tangential winding area A_T	73.59	mm^2
Cross section radial winding area A_R	65.81	mm^2

Table 3.6: Magnetic flux's measurement coils parameters

3.3 Gear shift mechanism

Gear shifting is another important aspect regarding MG testing. As mentioned in section 2.2, two different gear ratios are possible. Thanks to an innovative gear shifting mechanism, it is possible to automatically change from one transmission ratio to the other. A stepper motor must be driven to operate this shift. By commanding the motor to make a defined number of revolutions (or rather to pass through a given number of angular positions), it is possible to switch from one ratio to the other safely even while the MG is rotating. The chosen motor is the model 103H5208-5210 produced by Sanyo Denki Co. Ltd. shown in Figure 3.7.



(a) Stepper motor model 103H5208-5210 (b) Stepper driver model US1D200P10

Figure 3.7: Stepper drive configuration manufactured at Sanyo Denki Co. Ltd.

This particular model is particularly suitable since it has bipolar windings, is small in size, and has a basic maximum resolution of 1.8° . A driver, in this case model US1D200P10, shown in Figure 3.7, is attached to it to control this motor. By using this driver, the resolution of the motor can be further increased. By suitably configuring the driver, each step of the motor can be further divided into n sections, depending on the required precision. Table 3.7 and Table 3.8 lists respectively the main motor [12] and driver characteristics. [13]

Parameter	Value	Unit
Power supply voltage VDC	24	V
Rated current motor	1	A
Rotor inertia	$5.6 \cdot 10^{-6}$	kg/m^2
Motor length	39	mm
Recommended torque T	0.22	Nm
Recommended pulses frequency f_s	1.6	kpulse/s
Motor operating temperatures	$[-10 \div +50]$	$^\circ C$

Table 3.7: Stepper motor declared parameters

For motor control, the manufacturer provides a torque-pulse frequency map, shown in Figure 3.8. It is so possible to adjust the control accordingly so that you always have enough torque to do your assigned job.

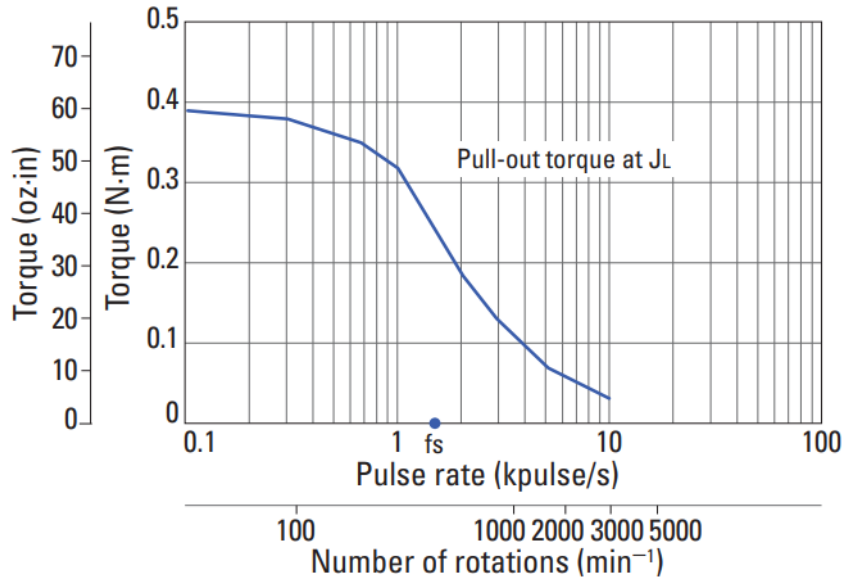


Figure 3.8: Torque - pulses frequency map provided by the manufacturer

Parameter	Value	Unit
Power supply voltage VDC	$24 \pm 10\%$	V
Max input current	3	A
Possible operating currents	[0.5 : 0.1 : 2]	A
Step angle partitioning	[1, 2, 4, 8, 16]	divisions
Stall current percentage	[100, 60, 50, 40]	%
Input modes	CK and U/D	
Min wire size towards motor	0.3	mm^2
Max wire length towards motor	<3	m
Operating temperatures	[0 ÷ +50]	$^{\circ}C$

Table 3.8: Stepper driver declared parameters

For simplicity, the CK, U/D command method was chosen, see Figure 3.9. In this way, one pulse marks the direction of rotation while the other sanctions the "steps," i.e., the change of rotor position from one pole of the motor to the other.

Finally, it is important to place the driver and stepper motor as electrically close together as possible. Long cables cause the inductance seen by the driver transistors to grow. This effect can be very influential since the greater the inductance, the longer it will take for the current to cancel out in the Turn-Off phase, see Figure

1 input mode (CK, U/D)

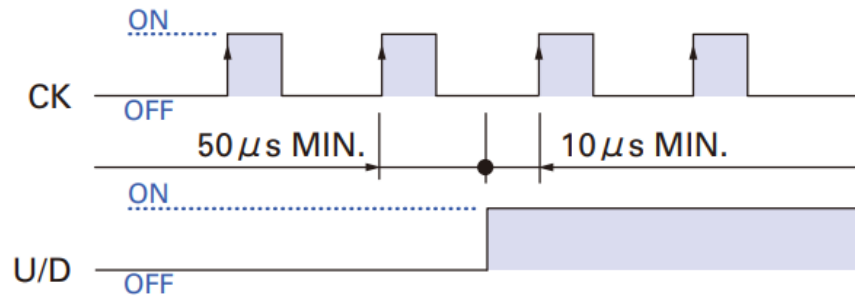


Figure 3.9: Stepper command timing example

3.10. In extreme cases, the current may not cancel completely, so the rotor would always remain in the same position without being able to switch from one pole to the other.

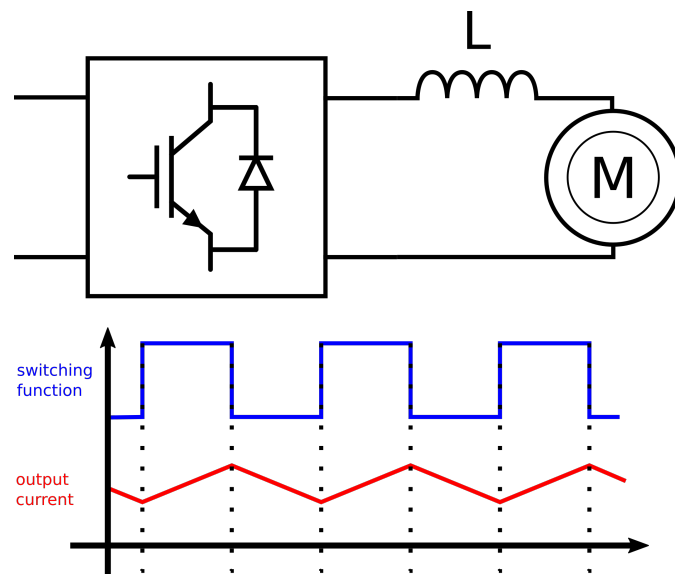


Figure 3.10: Leakage inductance effect on the driver output current

3.4 Switchboard project

In order to power all the components discussed so far in a logical and safe manner, it is necessary to wire an electrical panel. In any electrical power system, there are safety and reliability requirements that must necessarily be met so that accidental

accidents do not occur. The three-phase branch is connected to the electrical panel, within which the various protections and derivations are inserted until every necessary electrical element is supplied in a safe, efficient and insulated way.

First, to design an electrical panel, it is necessary to know the loads to be supplied. These are simplified to simple PV (Power - Voltage) loads so that the various upstream components can be sized with respect to the total power they must be able to deliver. In Table 3.9 all the elements that require supply and their characteristics are synthesized.

Component	Supply Voltage	Power Consumption
Inverter Power Supply KEN 5-0N	400 VAC	5 kW
Inverter auxiliary services for KEN 5-0N	24 V	5 W
Inverter auxiliary services for KWD 5	24 V	24 W
Inverter Heat-sink	24 V	5 W
Stepper motor driver	24 V	48 W
NI acquisition Compact RIO 9045	24 V	100 W
Encoder	5 V	175 mW
Torsiometer	24 V	12 W

Table 3.9: Stepper driver declared parameters

Once known all the loads to be powered, all that remains is to choose the right power supplies and protectors to perform this task. In order to power the DC low voltage components some AC/DC converters are required, basing on the supply voltage and amount of power required. On the AC side on the other hand no power converters are needed, but some more protections.

Figures 3.11 and 3.12 show the wiring diagram used and the list of components needed. Starting from the left, Figure 3.11 first shows the 5-pole three-phase branch (three phases, neutral and ground). Immediately after is connected the main circuit breaker (1).

From this point on, the first line required to supply the inverter starts. The first object encountered is a "fuse disconnect switch" (2), placed as the first element to prevent fault currents from propagating to the load. As can be seen from the 4 lines drawn above the object, this has to be a four-pole component.

Right after, together with the contactor, a stop emergency button is placed (3). The contactor is a main safety element due to its working principle: an excitation coil is placed between row A1 and A2 of the scheme, whether the coil is "excited" or not, the contactor closes or opens. A contactor can be Normally Open (NO) or Normally Closed (NC). In this case a NO version is required. The emergency button is placed to manually force the circuit to open in order to prevent damages on the components.

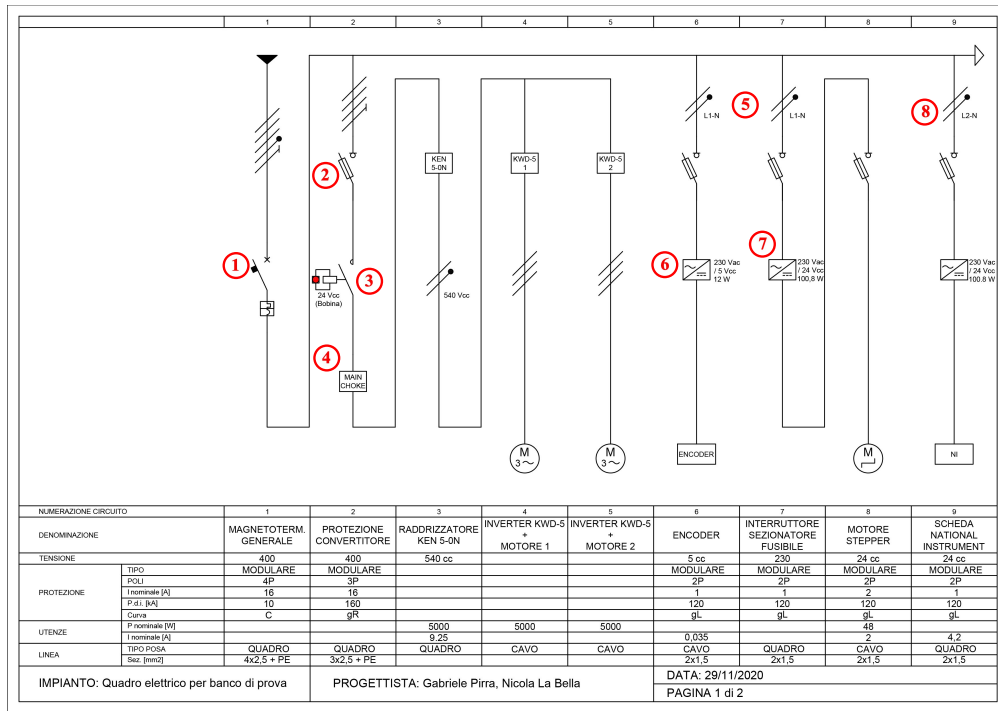


Figure 3.11: Single line wiring diagram page 1

Main choke (4) is a filter reactor, placed upstream of the inverter in order to improve the current distortion due to the inverter processing. It is fundamental to properly chose a suitable reactor in order not to excessively attenuate the input voltage but at the same time improve the current THD. This component, ALN12, is provided by the inverter’s manufacturer.

For what concerns the rest of the line, AC/DC rectifier for the inverter is supplied and subsequently the two DC/AC converters, so the two motors.

From this point on, it is no longer necessary a three-phase power supply. Only one line at time, together with the neutral one are picked. Loads have to be distributed as equally as possible on the lines in order not to create unbalances. Line 1 and Neutral one are picked (5) to supply the encoder and the stepper motor.

Firstly a protection is necessary: a two-poles fuse disconnecter switch is picked for every line. Being those two DC components it is necessary to convert the AC line into a DC one: $230V_{AC}/5V_{DC}$ is required for the encoder (6); $230V_{AC}/24V_{DC}$ for the stepper motor (7).

An isolated derivation of Line 2 (8) is dedicated to the NI acquisition system. A fuse disconnecter switch is as well placed as protection of the electronics.

The schematic continues in Figure 3.12, with a derivation of Line 3 (9) also protected by a fuse disconnecter switch. As can be easily seen, this last portion is

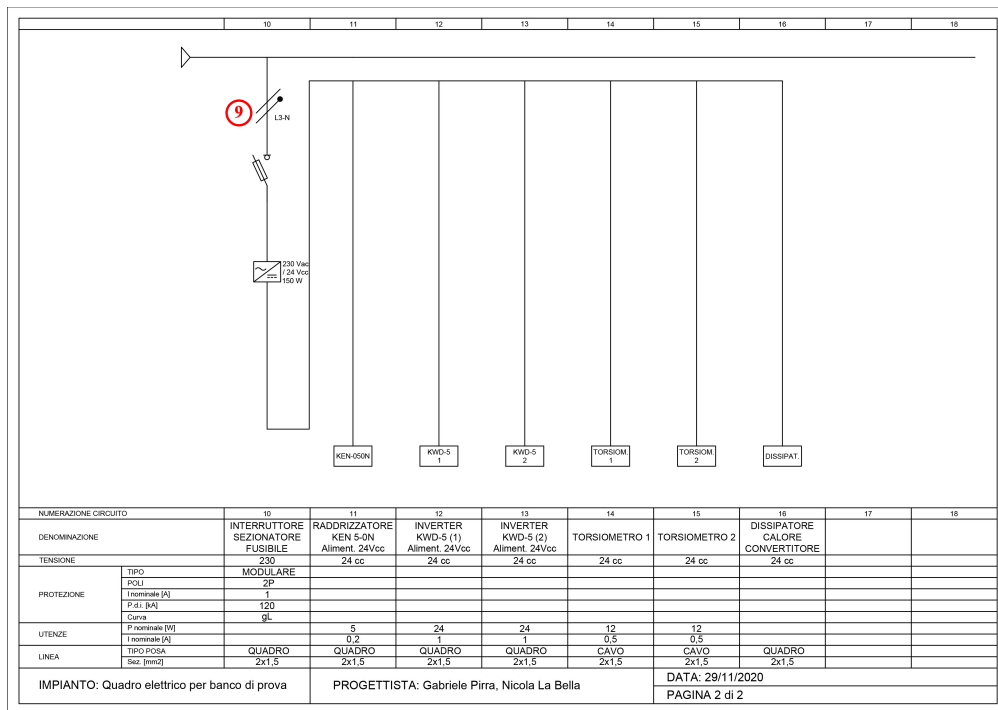


Figure 3.12: Single line wiring diagram page 2

dedicated to powering the auxiliary services of the inverter, heatsink and torque transducers.

Once defined all the components that need to be connected for a reliable and safe power supply, all that remains is to make an estimate of the space they occupy in order to purchase an appropriately sized electrical panel. A preliminary model to get an idea of the spaces needed for assembly is shown in Figure 3.13. There are some additional mounting aspects to consider:

- Terminal blocks for safe connections
- Spaces required for physical assembly
- Spaces for cable routing
- The possibility of power components emf disturbances influence on the electronic ones

For those reasons, this diagram represents only the minimum space required for assembly.

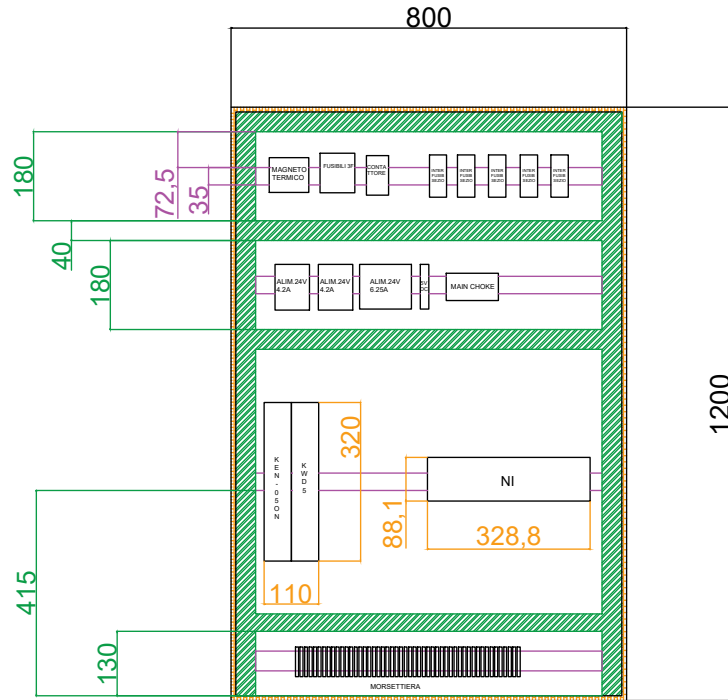


Figure 3.13: Switchboard preliminary spacing of the components

3.5 Enactment of the project

This section describes broadly the practical implementation of the design steps described in the previous sections.

The preliminary step is to assess the total floor of all the components chosen so far. The easiest and quickest way to get a realistic idea of how much physical space would be occupied is to make a simple 3D model, like the one in Figure 3.14.

The directly consequent step then is the actual assembly of the test bench. That means to create a metal structure able to firmly support all rotating components, namely the MG, motors, and sensors. Composite section aluminum profiles can be used, being particularly suitable for creating laboratory furniture. The result is shown in Figure 3.15.

Having finished the mechanical parts assembly, it is the turn of the electrical parts: the wiring of the switchboard. This step requires great care and must be done by strictly following the plan shown in Section 3.4. Compared with the design phase, a larger control cabinet was chosen, so the arrangement of components is varied to be made as convenient and accessible as possible during the assembly phase. Some important components not mentioned in the design stage were also added:

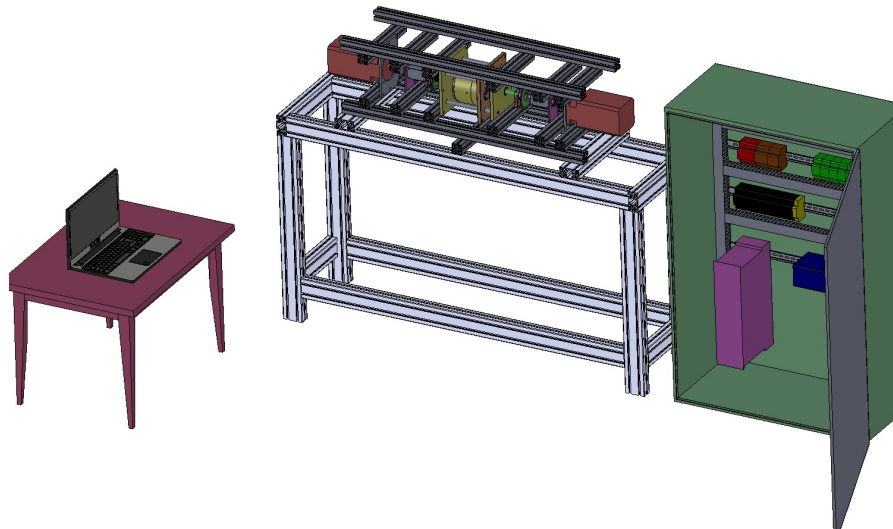
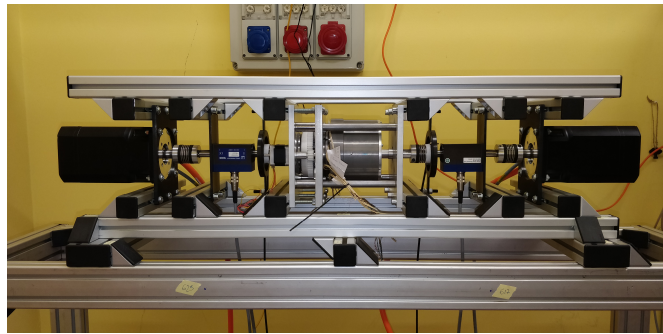


Figure 3.14: Total project occupied space



(a) Mounted Aluminum profiles



(b) MG along with the motors and sensors

Figure 3.15: Mounted test bench

- The voltage presence light
- Two switches to turn on and off inverter and stepper motor.
- The already mentioned emergency button
- A voltage socket for external devices

Final result is shown in Figure 3.16.

In the top part, it can be seen that the terminal block has been placed. There the 5-pole socket is led so that ground, neutral and the three phases wires can be connected.



Figure 3.16: Mounted switchboard

Correct grounding is a critical step in securing the system. In fact, every non-energized component within the switchboard must be properly grounded, so in the event of a fault, the current is safely discharged. Some dedicated grounding terminals have been places for this reason. In the second row all, starting form the left the main general switch, followed by the fuse disconnector switches and the contactor. On the third row were placed the DC power suppliers together with another terminal block. Fourth row is dedicated to the Nation Instrument environment; on the left were placed the cardboard pin-out terminals right before the cRIO 9045. Last section is dedicated to the inverter. On the left the inverter block together with its power supply. On the right it is placed the main choke. Notice that this input reactor has been placed on a certain distance to the inverter: this distance of at least 50cm is specified into the dustsheet and it is said as "necessary" for the proper operation of the inverter. This is understandable since a strong magnetic field is generated inside a such big sized inductor, which is very likely to cause electromagnetic interference issues on the inverter control electronics.

Chapter 4

Measurements and acquisition system National Instruments

A National Instruments environment was chosen for the measurement and acquisition system. The digital control and acquisition environment must be able to perform many functions in parallel and reliably:

- Acquire data from the sensors
- Send control signals to the inverter and to the services
- Identify the error signals and behave consequently to those

This means that it cannot all be carried out by one NI acquisition card but it is necessary to take several, each suitable for the type of signals it has to deal with. This means that first you need to make a list of the inputs and outputs and determine whether they are analog or digital. Table 4.1 lists all the signals the NI system has to deal with.

A clarification about signals nature is necessary. Differential frequency signals are very common into the measurements field. This is the most efficient system to transport data from the sensor to the processing system. Analog signals suffer the electrical nature of cables such as resistances and inductance, which make the signal very unreliable. Measuring frequency of a signal instead makes the difference: amplitude measurement is inevitably affected by voltage drops, frequency is not. Another consideration is about the waveform: frequency is measured once a signal has hit twice the zero amplitude. Square wave has very definite levels of amplitude, reached very quickly so it can be approximated as an impulse. Easy to realize by

Signal	I/O Type	Signal V level	Number	Frequency
2x Torsiometer	Digital Input	5V	2 (differential)	[5 ÷ 15] kHz
2x Encoders	Digital Input	2V	6 (differential)	[0 ÷ 60] kHz
emf Test coils	Analog input	[0 ÷ 5] V	6	[0 ÷ 36] kHz
2x Limit switches	Digital Input	24V	2	NaN
Emergency	Digital Input	24V	1	NaN
Inverter	EtherCAT I/O	NaN	NaN	NaN

Table 4.1: Input/Output signals parameters

means of transistors technology.

Distortion of the signals may be possible anyway, so a first countermeasure lays into the duty cycle setting: by setting duty cycle equal to 0.5, even harmonics are surely cut out, as stated into (4.1). That's a Fourier transform feature which states that into the perfectly square signal, only odd order harmonics can distort the sinusoidal signal.

$$f(x)_{sq} = \frac{4}{\pi} \sum_{k=1}^{\infty} \frac{\sin \frac{k\pi}{2}}{k} \cdot \cos(kx) \quad (4.1)$$

To avoid any other signal distortion the differential method applies: the sensor outputs both the signal and the negate of itself, then the NI card compares the two signals returning the “difference” between the two, cancelling any “common mode” disturb as shown in Figure 4.1

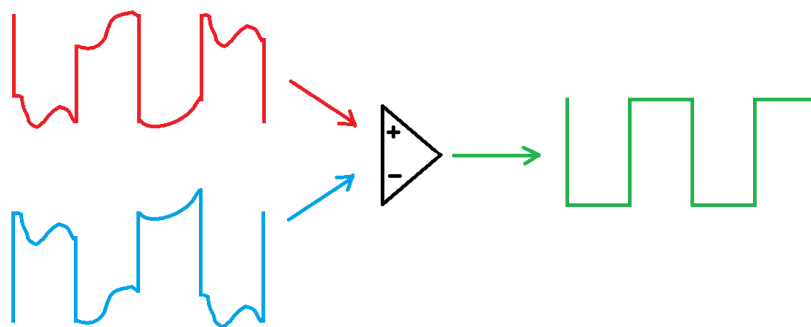


Figure 4.1: Example of common mode noise cut-off

Once the signals have been defined, the next crucial step is the choice of the NI acquisition system.

4.1 cRio and acquisition cards

This system must necessarily consist of a chassis and several acquisition boards capable of being able to receive the various types of signals. The choice fell on the cRIO 9045, shown in Figure 4.2



Figure 4.2: National Instruments Compact RIO - 9045

For what concerns the acquisition cards some further considerations are necessary:

- Whether the card capable of Input or Output signals
- Whether the signal can be Digital or Analog
- The Voltage level the board can stand
- The update rate the board can be capable of
- The number of channels
- The possibility to handle a differential signal

After all this reasoning, the choice fell on the three boards shown in Figure 4.3. The acquisition of signals from the torque transducers and encoders is allocated to the NI9411 boards. Perfectly suited for capturing differential frequency signals with adequate resolution. [14]

For what concerns limit switches and emergency signals, it is not necessary to have a very "fast" board, but still it has to deal with a 24V level signal. Perfect job for the NI9421 module. [15]

Analog signals are the last to consider. It is necessary a good resolution and an ADC converter. NI 9205 is picked up for this task. [16]

Table 4.2 summarizes all those considerations made so far.



Figure 4.3: NI acquisition boards

Module name	Module type	Signal level	Channels n.	Update rate
NI 9411	Digital Input	± 5 differential	6	500 ns
NI 9421	Digital Input	12, 24 V differential	8	100 μs
NI 9205	Analog Input	± 10	37	250 kS/s at 16 bits

Table 4.2: NI modules declared features

4.2 Elements of Sampling

The step after choosing hardware is inevitably the software one. This section discusses the techniques used to acquire frequency signals. Predominantly, "counters" and "clocks" have been used. The problems encountered at high frequencies and the problem of "synchronization" of measured quantities so that they can be correlated to derive results at the post-processing stage are analyzed.

4.2.1 Counters

For the measurement of signals output frequency, it is possible to use a LabView feature: a counter (see figure 4.4). A counter has the following main components: [17]

- Count Register: This register has the task to store the current count of the counter. It is possible to query the count register
- Source: Input signal which meets the requirements to change the current count stored in the count register. The counter looks for rising or falling edges on the source signal. The type of edge selected is called the active edge of

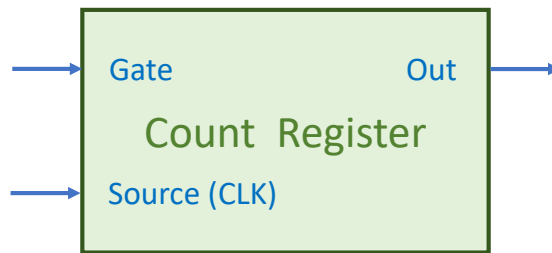


Figure 4.4: Control logic's of a counter

the signal. When an active edge is detected on the source signal, the count changes

- Gate: An input signal that determines whether an active edge detected on the source has to be stored or not.
- Out: An output signal that generates pulses (or a series of pulses), respectively to the programmed function.

Furthermore there are four different approaches to count edges depending on the chosen hardware:

- Simple
- Pause trigger (gated)
- Continuous buffered
- Finite buffered

Buffer, is a very fast memory comparable to cache, built into the NI modules. It is generally not very large, but at the same time it is very fast. This determines the approach to use to acquire data: make acquisitions of limited duration that do not saturate the buffer or make a series of short acquisitions continuously using the buffer circularly, see Figure 4.5. [17]

In order not to occur into a buffer saturation error, it is fundamental to extract data periodically. The period of extraction depends on the signal's frequency, on the number of samples of interest and on the capability of the system to fulfil the requests.

For example, torsimeters work between $5 \div 15$ kHz, so it is reasonably to set 1kHz as the frequency of data extraction from the buffer.

A non negligible issue may occur: error coming out of quantization. As the gate frequency approaches the source frequency, period measurements suffer from quantization error. That means that first and last source edges may or may not

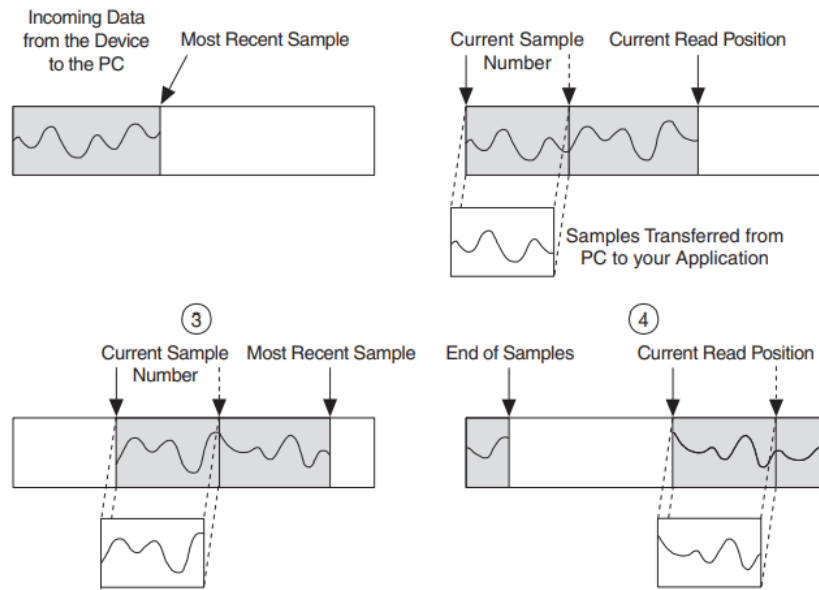


Figure 4.5: Single buffer acquisition method compared to circular buffer approach

be included in the period measurement. Three cases can happen, as described in Figure 4.6.

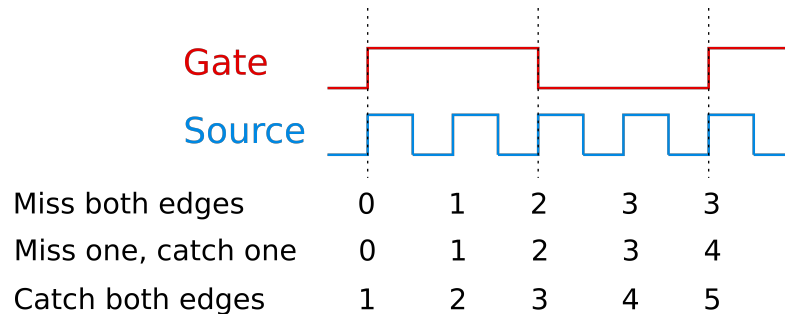


Figure 4.6: Quantization error cases

This error inevitably affects the measured quantities and depends on the frequency of the signal, as is shown in Table 4.3. [17]

The NI 9411 cards have built in counters which permits to process very large amounts of data at very high speed. All the data are stored into an internal buffer of the dimension of 128 bits. An example of the memory usage which applies in case of using a counter is brought in figure 4.9.

Input signal frequency	Measurement time	Quantization error
10 kHz	1 ms	10%
100 kHz	1 ms	1%
1 MHz	1 ms	0.1%
5 kHz	1 ms	0.02%

Table 4.3: NI modules declared features

4.2.2 Clocks

Event counting is the most important process of counter operations while measuring the source signal. It basically counts the number of active edges that have arrived on the source of the counter by polling the count register with software commands. Each active edge corresponds to an event for that signal.

It is fundamental to consider the frequency range of the signal to acquire: does exist many different methods to count, each applying only for the specific case whether signal's frequency is low or high. Using an unsuitable counting method leads to totally inaccurate results. Table 4.4 summarizes some approaches and in which cases they are preferable to be used.

	Counters n.	High frequency signals accuracy	Low frequency signals accuracy
Low frequency	1	Poor	Good
High frequency	1 or 2	Good	Poor
Large range	2	Good	Good
Sample clock (average)	1	Good	Good

Table 4.4: Frequency count methods accuracy

The last possibility is particularly interesting. Some hardware can use a "sample clock" for counter measurements. This clock enshrines when a measurement is stored into the on-board memory. In such This way the data rate and the read latency are decoupled from the frequency of the signal being measured. Here are listed two of the main methods used for counting frequencies:

- Sample clock timing (averaging disabled)
 - Good for low frequencies
 - Uses 1 counter

- Sample clock timing (averaging enabled)
 - Good for high frequencies and varying range of frequencies
 - Uses 1 counter

4.2.3 Counting frequency signals

The method applied for counting the frequency signals of torque makes use of Sample clock timing, with averaging enabled. This method is good when measuring high frequencies and varying range of frequencies and only uses 1 counter channel. When using this method, for each sample clock pulse, it is stored into the memory both the number of completed periods within a sample clock pulse and the period measured during those completed periods. DAQmx calculates the average frequency using those measurements, as shown in Figure 4.7.

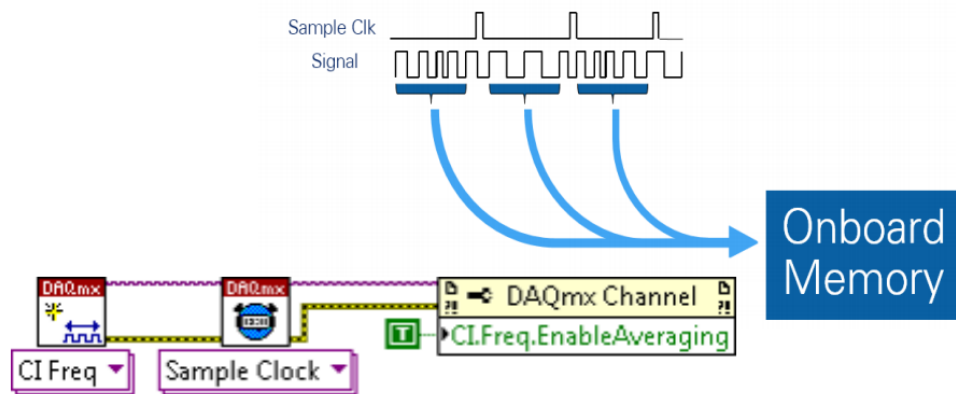


Figure 4.7: Data flow scheme of the frequency signals [17]

Referring to the torsionmeter case, the output has been defined upon a range of frequencies: and as long as the torque changes, it is expected the period to vary too (see figure 4.8). In order to create a stable and strong measuring systems, it is mandatory to ensure that all the needed measurement field is fulfilled: the counter has to be able to measure 5 kHz as long as 15 kHz.

By using a counter with a sample clock, it is required to set a maximum time in which the system "waits for data". The maximum required time lies on the lower frequency bound. That means it is necessary to wait the slowest possible signal to arrive before collecting data. It is immediate to calculate which is the minimum possible time to wait, see (4.2).

$$T = \frac{1}{f} \quad f \in [5,15] \text{ kHz}$$

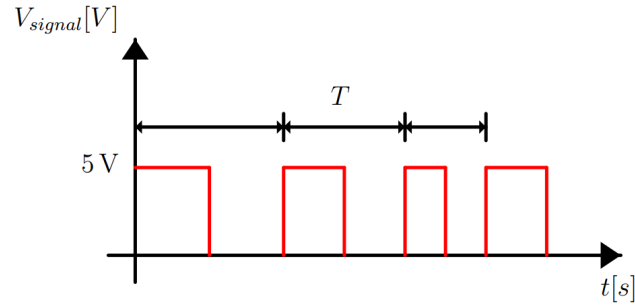


Figure 4.8: Overview of some frequency torque signals samples

$$T_{Max} = \frac{1}{f_{min}} = \frac{1}{5 \text{ kHz}} \geq 0.2 \text{ ms} \quad \rightarrow \quad f_{sampling} = 1 \text{ kHz} \leq f_{min} \quad (4.2)$$

Once calculated the sampling frequency which better fits the case, it is possible to proceed to the setting up of the code. Data flow logic is shown in figure 4.9.

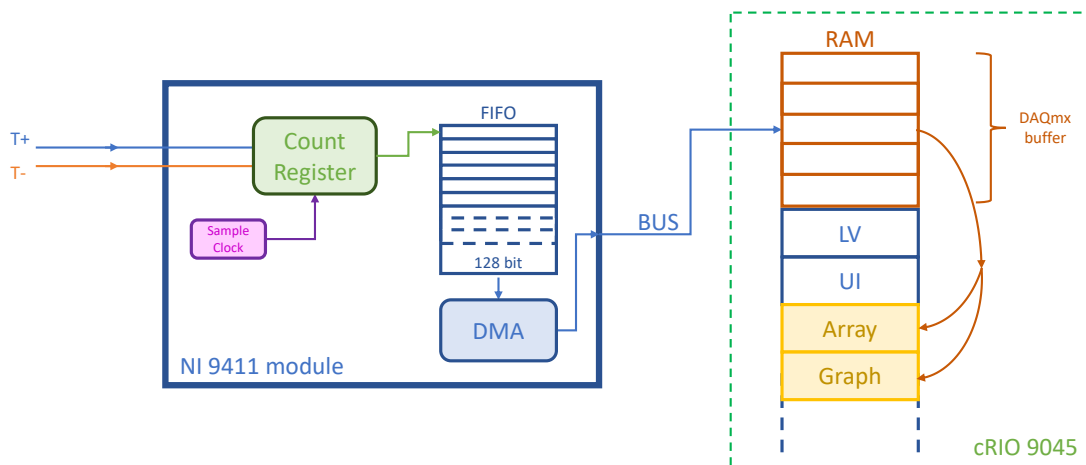


Figure 4.9: Flow chart of data, RAM and buffer memory usage

Digital signal route is the following: first is acquired, it is stored into the counter register. Once each sample clock trigger the average value of the samples is calculated to be then sent into a DMA's queue. Direct Memory Access (DMA) is a type of FIFO-based data transfer between an FPGA target and host processor. FIFO is a logistic term which stands for "First In First Out", so no data can remain stuck enqueued. Once the queue is full, informations are transmitted to the buffer memory to be graphically plotted.

4.2.4 Synchronization

Acquisition of many different frequency signals coming from different parts of the system, may need a further level of complication. To make it possible to relate every signal to each other, it is fundamental to let all the acquisitions begin at the same time.

Speaking about torque, the system is composed by two torsionimeters which requires to be synchronized to relate the 2 measurement outputs. It is possible to realize such relationship in LabView by using the same clock for every acquisition system. This is done by setting an internal output clock, as it has been done in figure 4.10.

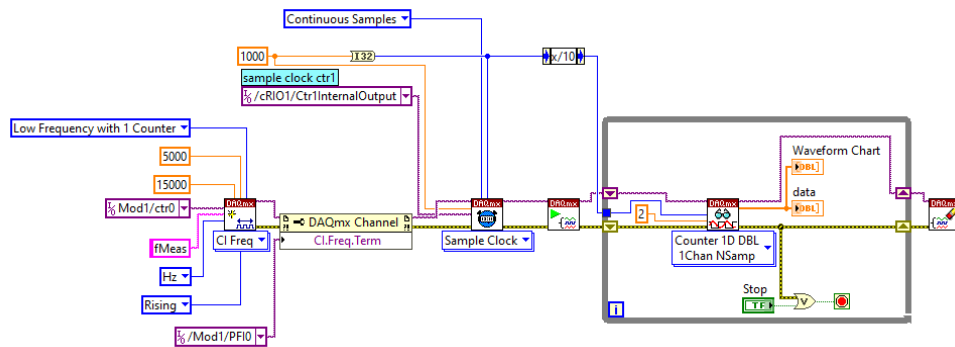


Figure 4.10: Internal common clock output

4.3 Test bench LabView environment

LabView is a programming language based on parallel processes. Parallel programming is conceptually different from any other type of language, since the flow of data does not follow one stream at a time, but several at once. This section presents the LabView program developed for drive control and that for sensor data acquisitions.

Before getting into a deep explanation of the programs, it is necessary to dwell on a fundamental step: device management. The inverter that drives the motors is connected via EtherCAT protocol to the cRIO. In order to control the drives, they must be detected by the system first. It follows NI modules connection. As can be seen in Figure 4.11, there are five data acquisition cards connected to the chassis. Only after all the instruments are connected and working the control VIs can be drafted.

Once all devices are ensured to be connected and working, you can proceed to the startup procedure.

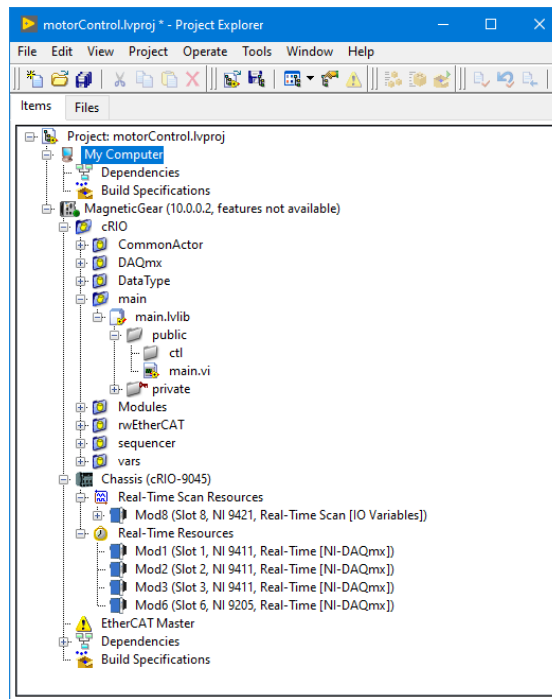


Figure 4.11: cRIO onboard project configuration and connections

This basically consists of a few simple steps, which are necessary to be able to start the control VI and the acquisition VI in an operational way. First of all, it is necessary to connect the pc to the cRIO. Once the connection is established, the operational status of the motors can be commanded to the inverter. After these steps have been taken, there are two main VIs to analyze: the main VI and the syncAcq VI.

The first VI to be analyzed is the main VI. This is designed to contemporaneously control both motors through a real-time EtherCAT protocol. Like any LabView VI, it consists of front panel and block diagram.

The front panel, 4.12, is divided by columns, which represent the layers of logic regarding motor control. In the first column is the "Stop" button, which allows the program to be safely stopped. This makes sure that the program is terminated without errors and without leaving the system memories full.

The second column is the error column. At the top is the emergency button that commands the contactor inside the switchboard to de-energize the entire system. The error window, on the other hand, takes care of showing the error code instead, in the event of a malfunction of the drives. A list of the exit-error codes is provided below.

The third column is the one that deals with the actual "control" of the motors.

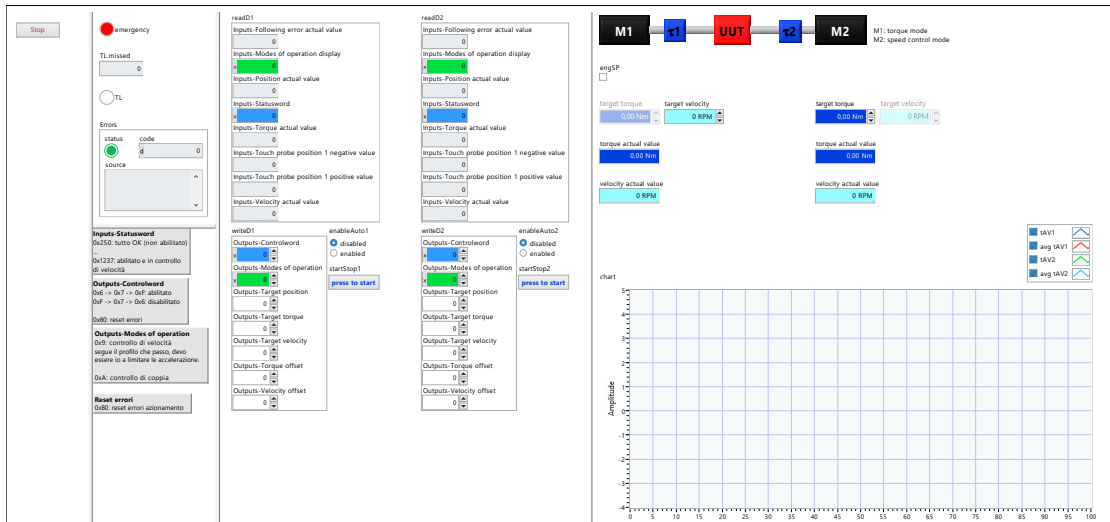


Figure 4.12: Motor control - main VI, front panel

For each motor there are 2 windows: the top window shows the instantaneously measured parameters while in the bottom window you can enter the desired values. Even though motors control is already possible from these windows, it might be tough, so a fourth column has been inserted to simplify this process. A legend is provided at the top to reflect the working "side". In the middle part there are four boxes for each engine: two for reading the current parameters and two for setting custom values. As can be seen, two boxes are grayed. Obviously it is impossible to simultaneously control two motors in torque or speed because this would make the system hyperstatic. Therefore the program makes it possible to choose to which motor apply the torque control and sets the other accordingly to be controlled in speed. A graphical box is also present, in order to provide a history of the measured values respectively to the entered ones.

There is one last aspect to consider: how to perform motor startup. a double safety measure has been included to prevent accidental motor startup. There are two boxes: "enableAuto1" and "enableAuto2" that define whether the motor is enabled or not. The two buttons immediately below, on the other hand, trigger the motors to actually be powered. Nothing, however, can be set in motion unless the status of the "engSP" checkbox is also changed. Once these three steps have been taken care of, motors can actually rotate.

Concerning about the block diagram shown in Figure 4.13, it is the embodiment of the front panel just analyzed. It is mainly divided into two macro-blocks. The first block refers to the third column of the front panel: the data entered for both engines is enclosed within a local variable "write". same holds for other signals not directed to the motors, such as the stop button, the emergency button

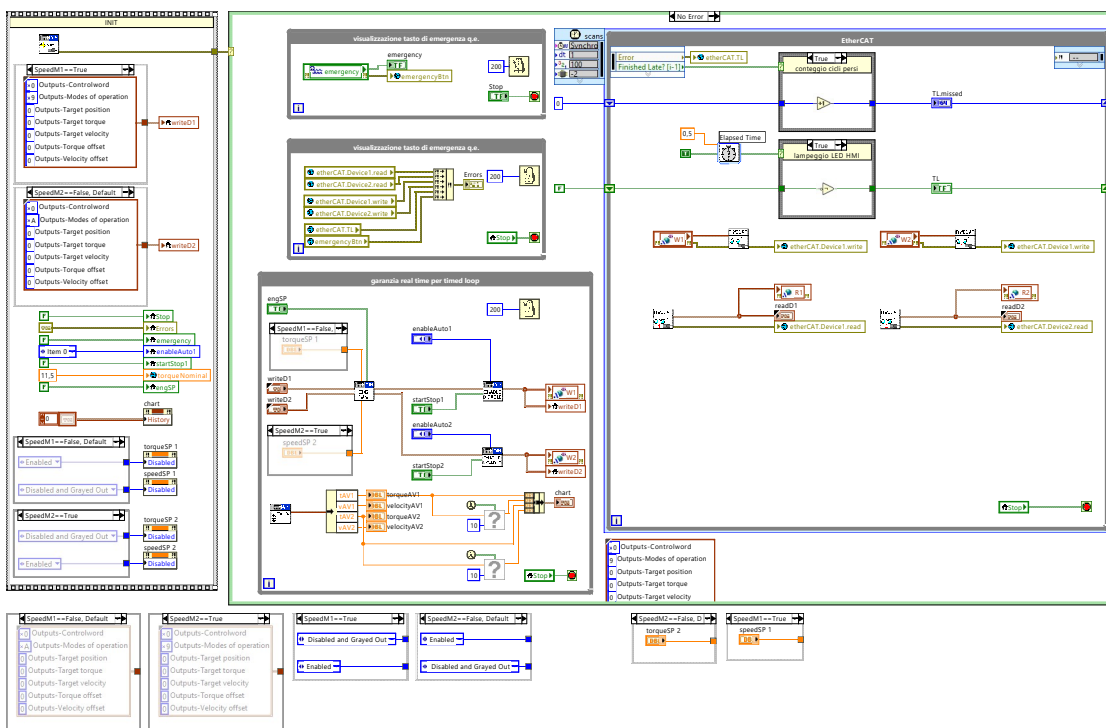


Figure 4.13: Motor control - main VI, block diagram

and the security controls set upstream the motor startup. As can be seen at the bottom of the first box, a control has been placed to disable torque or speed control respectively to the selected configuration.

The second block is the beating heart of the project. Its normal operation is described in the "No Error" case. This consists of four while running cycle structures in parallel. In addition to the first two on the upper left, dedicated one to the emergency handling case and one to real-time error checking, there are two others: on the right one undertakes the handling of data transmission through the EtherCAT protocol, on the bottom left the other deals with reading the received data and entering the parameters to be sent to the drives.

In case an error occurs the program ensures the "exit with error" procedure.

The second fundamental VI to be analyzed is the Synchronous acquisition one. This is designed to simultaneously acquire the sensors signals in order to be shown into a graphical panel.

Compared to the VI intended for motor control, this one is conceptually simpler: it must acquire data from two torque transducers and two encoders and do so simultaneously. In the 4.2.4 section, it was discussed how signal synchronization can be achieved. In this case, an external clock from the board connected on



Figure 4.14: Acquisition - syncAcq VI, front panel

module 6 (the NI9205 in particular) is used to synchronize all acquisitions. This is a particularly efficient method and ensures the temporal relationship between the acquired data.

The front panel shown in Figure 4.14, summarizes the purpose of this VI: obtain speed and torque data, all at the same time. The first column shows the measurement inputs. At the top is shown the module that provides the "Sample Clock" to the system, along with its frequency. At the bottom, on the other hand, there are four rows with two boxes each. Here the module suitable for providing the measurement input and the counter to be used can be chosen. The second column places graphical representations of the data and of the frequency analysis of their Fourier series decomposition.

For what concerns the block diagram in Figure 4.15, it must handle the four measurement inputs plus a fifth one used as master clock. This is all done within a while loop that terminates once a given number of samples has been acquired; see Section 4.2.3. The data are initially processed individually, and then brought together and plotted into the front panel. Acquisition is continuous and no gap of data is present. This is possible thank to the external master clock which decouples the acquisition counters by the clock.

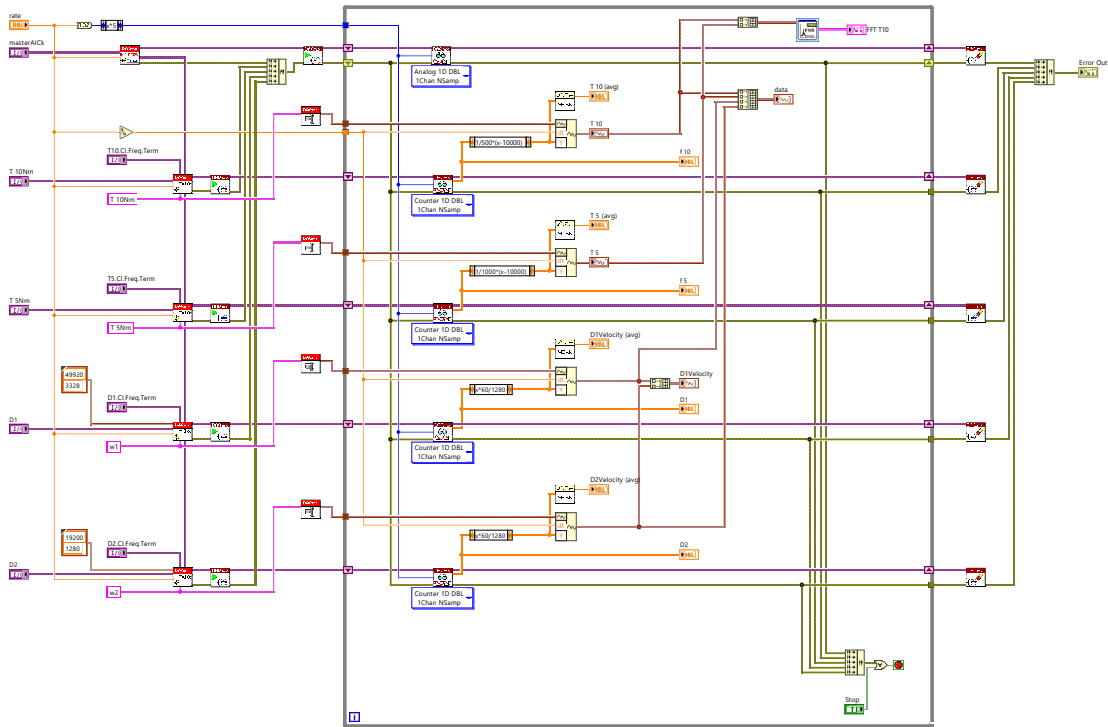


Figure 4.15: Motor control - syncAcq VI, block diagram

4.4 Emf sensing coils

The emf induced by the rotating magnetic field produced by magnets is an additional quantity that can be incorporated within the NI measurement system using the NI9205 module. Regarding magnetic measurements on magnets, it is not possible to make a true energy characterization since it is only possible to know one of the two fundamental magnetic quantities. Thanks to the Faraday-Neumann-Lenz law, (4.3), the relationship between variable magnetic field and induced voltage at the ends of a N windings coil is known.

$$V = -\frac{d\lambda(\vec{B})}{dt} \quad (4.3)$$

This formula is fundamental for sensing a variable magnetic flux, done by simply measuring the voltage across a wire. Formula can be further extended to multiple windings of a coil, by simply considering the flux linkage $\lambda_B = N \cdot \Phi_B$.

It is immediate, once known few geometrical factors of the coil such as the number of windings N and the cross sectional area A_T and A_R , to obtain a measure

of the magnetic flux density \vec{B} from the measured voltage, as shown in (4.4).

$$|\vec{B}| = \frac{|\Phi_B|}{A_x} = \frac{1}{A_x} \cdot \left| \int_0^t \frac{V}{N} dt \right| \quad (4.4)$$

Notice that the acquired data are discrete, but the formula still holds. Numerical integration can be as well performed in post processing on digitally filtered data. An example on how to digitally acquire the voltage waveform is shown in Figure 4.16.

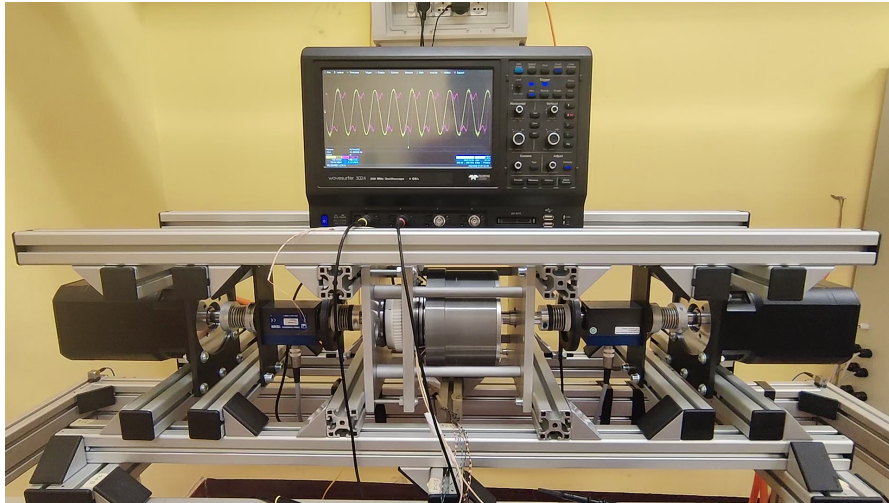


Figure 4.16: Example of sensing voltage acquisition

Each peak acquired corresponds to a "snapshot" of the flux of a specific magnetic pole of the sun ring. This means that the waveform has periodicity $T = \frac{2\pi}{pp}$, referring to Table 2.1, and changes with respect to the gear engaged. This is an interesting property since it allows in post-processing to obtain, with a limited amount of data, a 2π electrical degree view of the trend of magnetic fluxes within the system.

Chapter 5

Static tests

The testing phase is crucial for the magnetic gear prototype. This chapter describes the entire procedure followed to effectively test the gear.

As previously mentioned in Section 4.3, it is not possible to impose either side of the gear only speed or only torque because this would make the system hyperstatic. Therefore, what is typically done is to impose first on one side, and then on the other, a set of torque and speed values on the two motors. This makes it possible to analyze the operation of the transmission whether it is used as a multiplier or a torque reducer. Before proceeding, it is deemed necessary to define a wording convention to be able to recognize the side being discussed. It is either possible to use the gear as speed or torque multiplier as well as reducer, basing on the applied configuration. It depends on which side of the MG those quantities are applied.

- **Speed/Torque Multiplier:** Speed is applied on the ring side, torque on the sun side
- **Speed/Torque Reducer:** Speed is applied on the sun side, torque on the ring side

This difference in prototype usage may be relevant in testing, since the usage relationship may not be symmetrical; in other words, different results may be obtained based on whether the prototype is used as a multiplier or a reducer. In addition, there are two different gear ratios to consider:

- Gear 1 $\tau_{r/s} = 2.6$
- Gear 2 $\tau_{r/s} = 1.57$

Given the amount of functionality to be analyzed and investigated, it is retained to be necessary to carefully plan the tests to which the gear will be subjected. The process of defining a priori the tests to be performed on the bench is called "design of experiment", or rather DOE.

5.1 DOE

Regarding the static tests, DOE is structured in such a way to make multiple steady-state acquisitions covering all the operating points of the MG. The method used can be likened to two nested cycles. In the first iteration a torque value is imposed, and the speed is varied in small steps until an arbitrarily placed limit is reached. In the next iteration the torque applied increases slightly while the speed is made to vary within the same limits. Loop keeps running until the maximum bearing points of the MG are reached.

Initially, a "no load" test is carried out, which has a dual purpose: to see the behavior of the quantities of interest in terms of thermal dynamics and in the meantime to preheat the mechanism. By carrying out subsequent speed rise-fall tests, thermal steady state is reached.

Since there is no way to put a thermal sensor inside the gear, a magnet's characteristics can be exploited for this purpose: magnets follow a demagnetization curve that depends mainly on the applied magnetic "load"; however, they are also strongly subject to temperature. The higher the temperature rises, the less residual induction they are able to provide. This dependency of magnets' B_r on temperature can be exploited to get an idea of how much thermal stress this mechanism undergoes during use. This phenomena is also supposed to impact on efficiency.

As a final consideration, the operation of the magnetic gear is desired to be investigated by approximately always exploiting the same operating points. Thus, to couple the multiplier and reducer operation, it is necessary to translate the imposed values of speed and torque with respect to the engaged gear.

The tests to be performed are then structured as follows:

- Gear 2
 - Multiplier setup
 - * No-load test, speed rise-fall-rise
 - * Speed variation test $n=[60:60:720]$ rpm
 - * Torque variation test $T=[0.5, 0.75, 1.0, 1.15]$ Nm
 - Reducer setup
 - * No-load test, speed rise-fall-rise
 - * Speed variation test $n=1.57 \times [60:60:720]$ rpm
 - * Torque variation test $T=[0.78, 1.17, 1.57, 1.96]$ Nm
- Gear 1
 - Multiplier setup

- * No-load test, speed rise-fall-rise
- * Speed variation test $n=[60:60:720]$ rpm
- * Torque variation test $T=[0.3, 0.45, 0.6]$ Nm
- Reducer setup
 - * No-load test, speed rise-fall-rise
 - * Speed variation test $n=2.6 \times [60:60:720]$ rpm
 - * Torque variation test $T=[0.78, 1.17, 1.57, 1.96]$ Nm

To avoid confusion, Table 5.1 is provided, values imposed relatively to the gear and to the corresponding operating point based on the multiplier and reducer configuration are explained in detail.

	Multiplier		Reducer		
	Ring Speed [rpm]	Sun Torque [Nm]	Sun Speed [rpm]	Ring Torque [Nm]	
Gear 2	60	0.5	94.3	0.78	
	120	0.75	188.6	1.17	
	180	1	282.9	1.57	
	240	1.15	377.1	1.96	
	300		471.4		
	360		565.7		
	420		660		
	480		754.3		
	540		848.6		
	600		942.9		
	660		1037.1		
	720		1131.4		
	Gear 1	60	0.3	156	0.78
		120	0.45	312	1.17
180		0.6	468	1.57	
240			624	1.96	
300			780		
360			936		
420			1092		
480			1248		
540			1404		
600			1560		
660			1716		
720			1872		

Table 5.1: Table of the DOE tests performed respectively to the MG possible configurations

5.2 Measurements results

This section reports the data measured by the bench sensors and acquired by the NI system by means of the cRIO. The measurements obtained investigate every possible operating point of the MG, as explained in Section 5.1.

First, the unloaded tests are performed. In such a way the pre-heating process of the MG, which is essential for some reliable loaded test, is done. This is followed by tests with an applied load in the form of a in order to finally evaluate the overall efficiency of the system. A point of interest within this analysis is to understand what is the actual contribution of mechanical and electromagnetic losses in the MG.

As explained at the beginning of the Chapter, a notation is used in the section to simplify the reading:

- **Torque/Speed Multiplier:** Torque T_1 is applied on the sun side, speed ω_2 on the ring side.
- **Torque/Speed Reducer:** Torque T_2 is applied on the ring side, speed ω_1 on the sun side.

5.2.1 Magnetic Flux Acquisition

Before proceeding with the presentation of test results, it is important to make a small digression regarding magnetic fluxes. As mentioned in Section 4.4, a total of six coils were applied around three ferromagnetic poles, each 120° , of the carrier. By doing so, it is possible to have a reliable measurement of the fluxes involved within the mechanism during each of its operating points.

From these coils we obtain a "radial" and a "tangential" flux measurement, depending on the direction of flux respectively to the rotating axis of the MG. The waveform and peak flux value are indicative of the operating state: the lower the peak, the greater the "magnetic" load the magnet must carry; the more distorted the waveform, the greater the losses due to harmonics.

In addition, there are two Gears to be analyzed with a different gear ratio. The measured fluxes are definitely periodic, since the rotating magnets are always the same. It is therefore possible to have a 360° electrical view of the state of the fluxes during operation.

Figure 5.1 shows the magnetic flux with no load applied data measured on Gear 1 and 2, respectively. This should correspond to the condition of maximum peak value and lowest harmonic distortion of both radial and tangential flux.

As can be easily seen, a construction error was made within a polar pair of Gear 1. This does not benefit the operation of the MG and is responsible for an eventual reduction in performance in terms of tightness and efficiency.

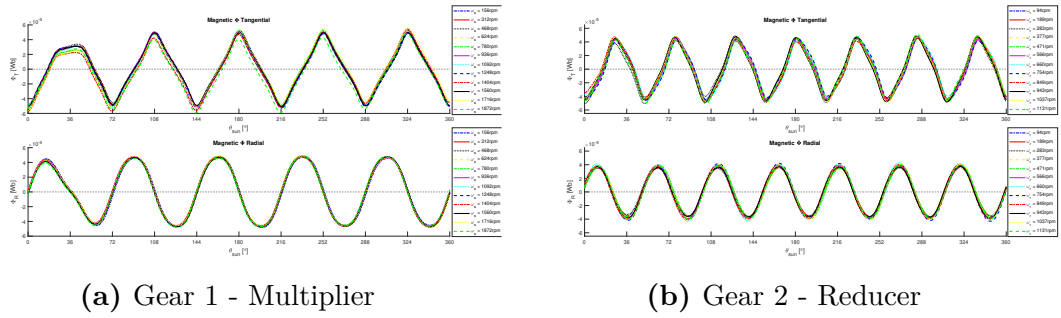


Figure 5.1: Radial and Tangential Flux, No torque load applied

Figure 5.2 shows the magnetic flux under the worst stress possible condition. Data are measured on Gear 1 and 2, respectively. This should correspond to the lower peak value and highest harmonic distortion condition, for both radial and tangential flux.

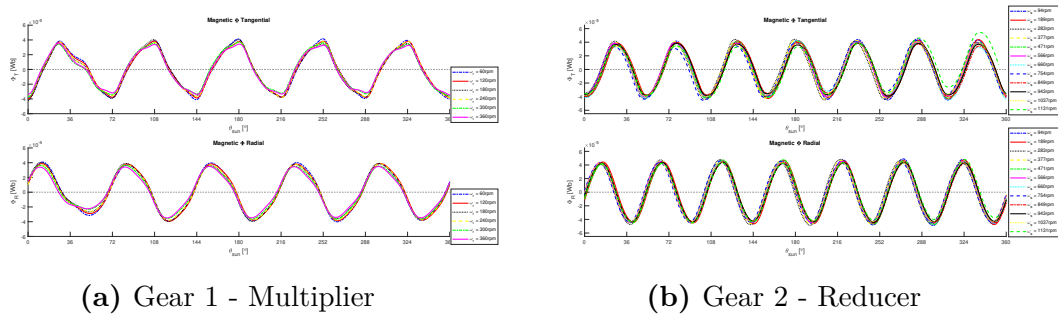


Figure 5.2: Radial and Tangential Flux, Maximum torque load applied

5.2.2 No-load tests

No-load tests are crucial to the study of the mechanism since they give an idea of whether the leakage contributions belong to the electromagnetic or mechanical world. The mechanical contribution to system losses is expected to predominate. It should also be dependent on the utilization configuration of the MG.

This is due to the different radial size of the two transmission wheels: in order to be firmly engaged on an axis, but at the same time free to rotate, bearings must be used. It is possible to decouple the loss contributions of the two bearings by exploiting a property of the no-load test: by imposing speed on one side and zero torque on the other, the torque transducer placed on the speed-driven side will always see zero torque. For example: applying speed ω_1 on the Sun side, the torque measured on the same side must be 0 (by definition); on the Ring side there is no

torque T_2 imposed, so the torque transducer measures a torque that must be due to losses on the Ring side bearing.

The larger the bearing, the higher the measured loss contribution on its "side" is expected to be. Since the Ring wheel' diameter is larger with respect to the Sun wheel's one, the measured Torque loss on the former should be higher.

In Figure 5.3, MG operation in multiplier configuration is shown. A total of four tests were performed: up, down, up and up. Note that there is no resistant torque applied in this test, so the resistant torque seen in the graph is "lost" within the mechanism. In other words, the "no-load" losses of the mechanism are shown.

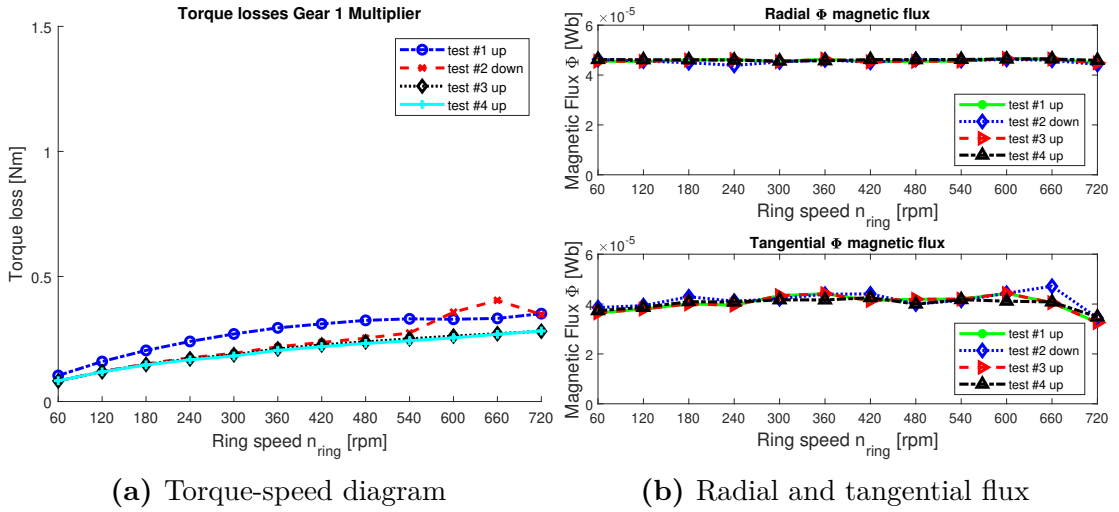


Figure 5.3: Measured results, No-load applied, Gear 1 ,Multiplier configuration

As can be seen, with each iteration, the lost torque curves "go down." The fluxes follow the same pattern, although in a less pronounced manner. This variation can be attributed to the change in temperature within the mechanism: the further into the thermal regime one goes, the lower the losses seem to be.

In test #2 there seems to be a slight point of departure from linearity. The radial flux do not seem to be affected while the tangential flux seem to want to suggest dependence.

Same preliminary considerations apply to Figure 5.4, in which the no-load test for gear 2 in multiplier configuration is shown. This time the following tests were performed: up, down, up and up.

There is also a downward trend as far as Gear 2 is concerned. One would think that the lost torque would also be lower than in Gear 1, but the slightly decreasing values recorded are only due to a different gear ratio. Flux on the contrary are a bit more disordered with lower values. However, the discrepancies measured during some tests seem to fall back during the next tests.

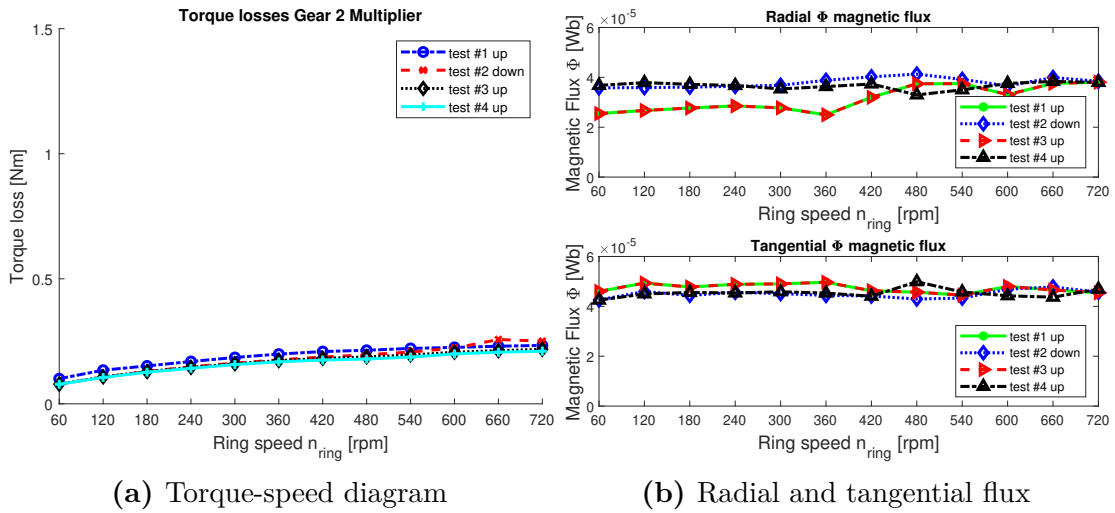


Figure 5.4: Measured results, No-load applied, Gear 2, Multiplier configuration

It is then time for measurements in reducer configuration, Gear 1 results are shown in Figure 5.5. In this case, it appears that bearing losses are higher with respect to the previous case. This is because, as anticipated earlier, we are analyzing leakage contributions on a larger diameter bearing in this case. Growth in bearing size results in greater losses.

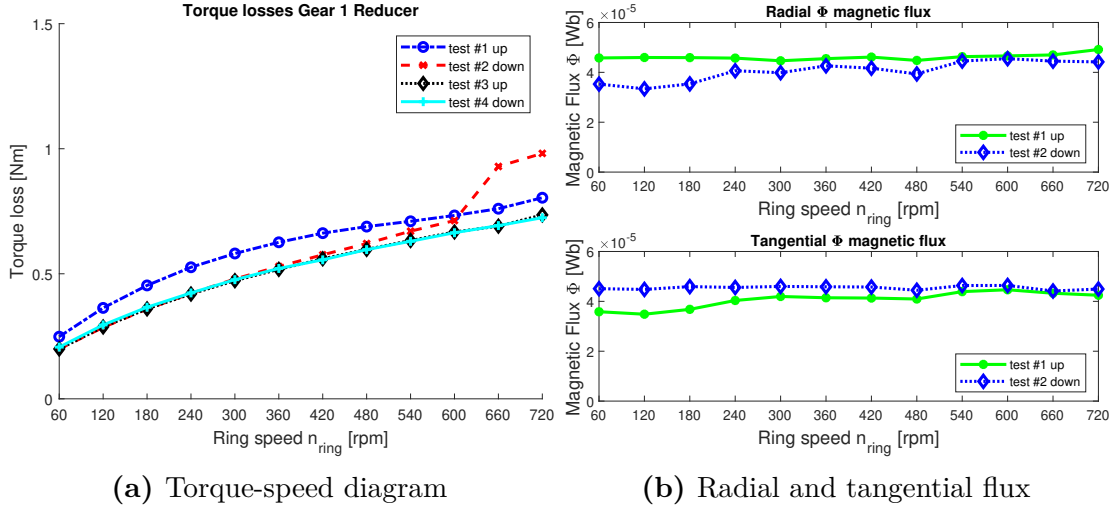


Figure 5.5: Measured results, No-load applied, Gear 1 ,Reducer configuration

The loss trend again seems to be decreasing as the tests go on. One test deviates in endpoints from the other tests. However, this does not seem to be anything of concern since it remains an isolated case. Flux also seem fairly stable around

$40\mu Wb$.

Gear 2 is similarly analyzed in Figure 5.6.

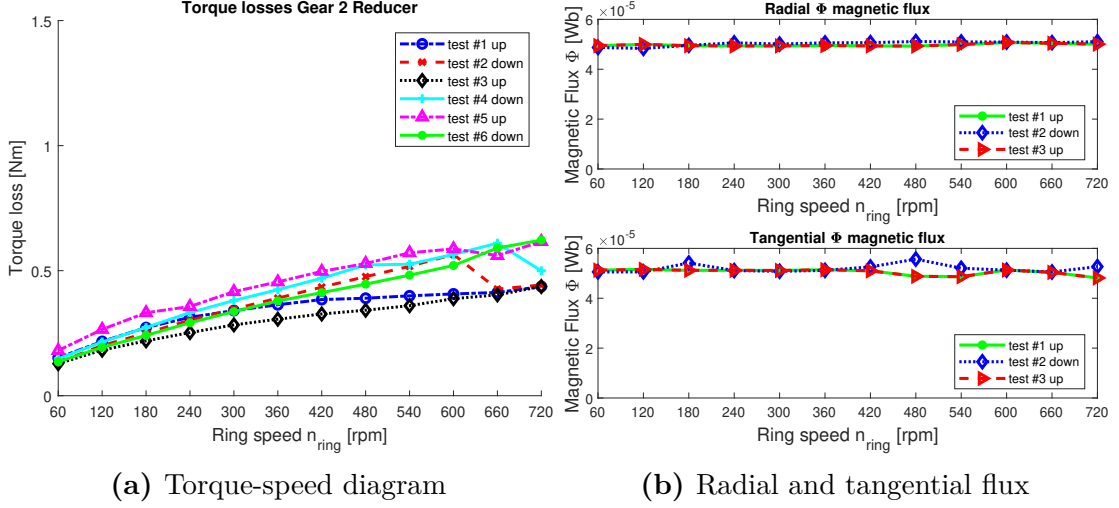


Figure 5.6: Measured results, No-load applied, Gear 2 ,Reducer configuration

The greater amount of testing on this configuration gives a wider range of results to analyze. With regard to torque, it seems in this case that the losses are in contrast to previous cases. However, points of non-linearity are seen on the final measurements, this would suggest that this trend of increasing losses with testing was caused by a problem on the bearings that led to seeing more losses. The fluxes on the other hand are very stable. Both around $50\mu Wb$, they seem to be slightly affected by variations on the final measurements.

In general, the trend of the loss curves seems to be going downward, which is absolutely reassuring looking forward to the load tests, during which efficiency is determined.

5.2.3 Loaded tests

In these load tests, the approach used is different. The torque-speed curve measured on either side of the MG is no longer very indicative of its efficiency during operation. Therefore, global efficiency plots of the mechanism derived from the formula (5.1) are shown in this section. Ring speed is as well no longer relevant, but rather the efficiency plot might be based on the speed difference between rotors.

$$T_{out} \cdot \omega_{out} = \eta \cdot T_{in} \cdot \omega_{in} \quad \longrightarrow \quad \eta = \frac{T_{out} \cdot \omega_{out}}{T_{in} \cdot \omega_{in}} \quad (5.1)$$

Remains relevant and useful instead the analysis of the magnetic fluxes within the MG. From an energy perspective, it is not possible to exclude the loss contribution

of the magnets within the transmission, since a second magnetic component in addition to the flux density B is not known. The behavior of magnets in general is known: given a demagnetization curve and a load curve, they can be related to estimate the behavior under load of the magnet and therefore of its value of supplied induction B under load. This means that as the working conditions of the magnet change, assuming the same cross section area of the sensing coil, the measured flux density B_{meas} may vary. If demagnetization curves of the magnets were available, it would be possible to trace the energy lost by knowing only the induction; since only the residual induction is known for this particular model of magnets, this is not possible.

Therefore, in this section tangential and radial flux of the magnets are analyzed in relation to the overall system efficiency. It is expected that the greater the strain imposed on the MG, the lower the flux detected, accordingly to its demagnetization curve. At the same time, the greater the power transmitted, the lower should be the influence of losses within the system, assuming them to be nearly constant.

Performed tests are described in the DOE, Section 5.1. Figure 5.7 reports the first results obtained. Measurements were performed by setting a certain Torque value, refer to the figure, and acquiring subsequent values of speed. In this case torque T_1 is applied on the Sun Wheel and speed ω_2 on the Ring Wheel.

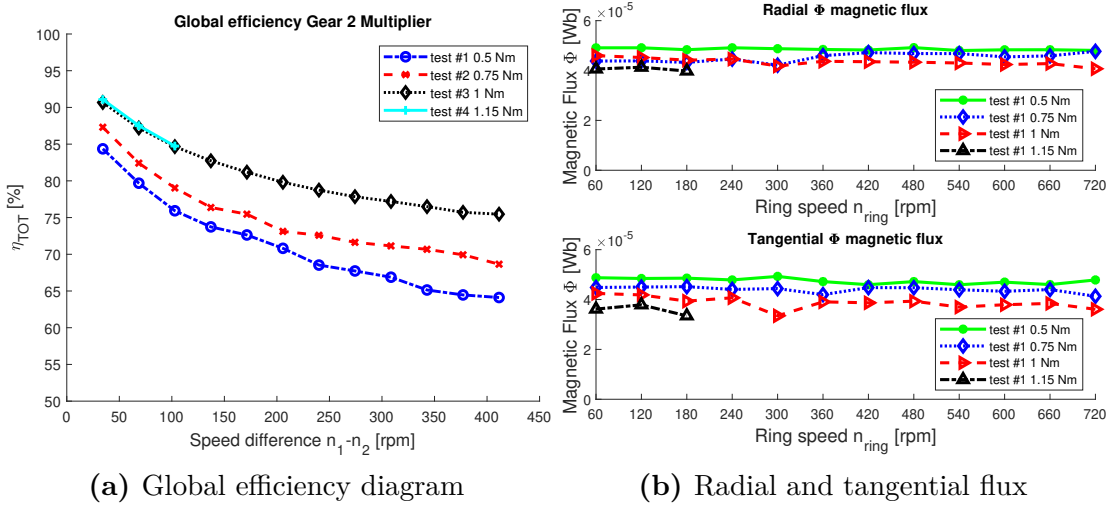


Figure 5.7: MG's performance, T_1 torque on Sun side, Gear 2, Multiplier configuration

As can be easily seen, as the applied load increases, the efficiency goes up significantly. This is because, as mentioned, bearing losses can be considered almost constant. The limiting curve seems to be reached with the last two tests with the higher torque, in fact the efficiency points seem to be overlapping. The fluxes also

seem to behave as expected: moving between values on the order of $50 \div 40 \mu Wb$, they drop slightly as the load increases. This indicates that the working point of the magnets is moving along the demagnetization curve.

For the next test shown in Figure 5.8 the same considerations apply, but now are related to gear 1. In order to analyze the mechanism around the same work points, so that the tests can be correlated, the torque values T_1 applied to Sun have to be calculated considering the different gear ratio.

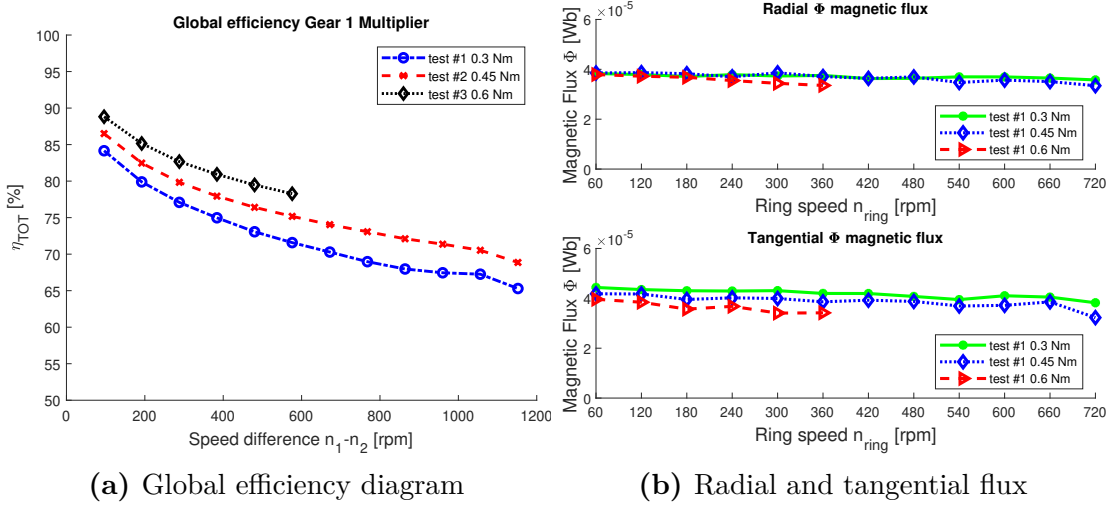


Figure 5.8: MG's performance, T_1 torque on Sun side, Gear 1, Multiplier configuration

The results seem consistent with the ones seen previously: growth in efficiency as the applied load increases and a consequent slight reduction in flux due to the provided induction decrease by the magnets. The efficiency curve at maximum load is slightly lower than that obtained for Gear 2 but the steadily decreasing trend as speed increases seems to conform. Somewhat more pronounced is the flux decay as speed increases in this case.

In contrast, the opposite configuration is now presented. The MG's use as a torque reducer involves applying a T_2 on the Ring and ω_1 on the Sun. It is expected to find congruent results with respect to the previous case, since the chosen working points are equivalent. Case with Gear 2 applied is shown in Figure 5.9.

In this case the maximum efficiency obtained seems to be higher with respect to the multiplier's case. The monotone decreasing trend is similar to what obtained previously. Same decreasing situation for fluxes: as the load increases the flux decreases following the magnet demagnetization curve.

Concerning next test shown in Figure 5.10 the same considerations apply, but now are related to gear 1. In order to analyze the mechanism around the same

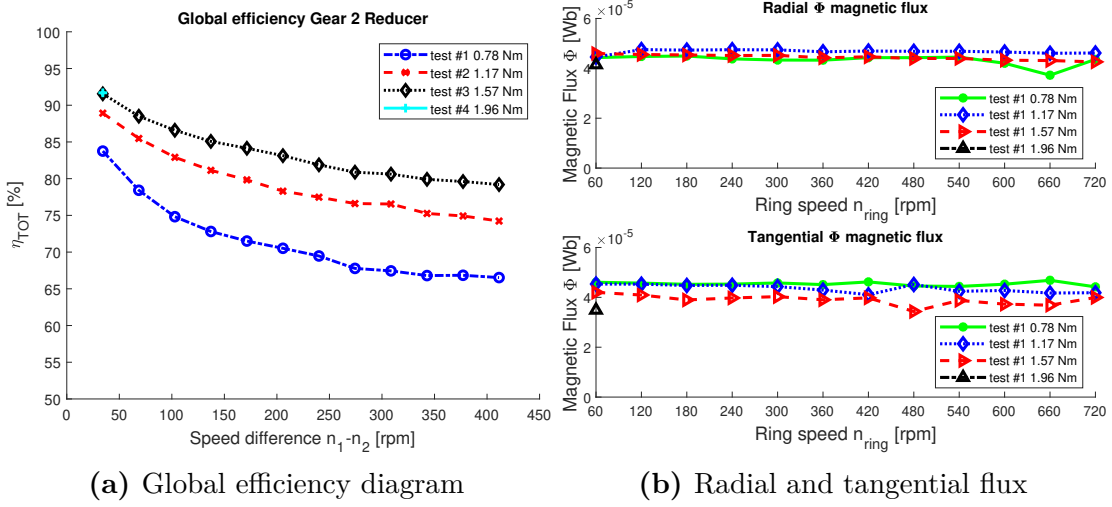


Figure 5.9: MG's performance, T_2 torque on Ring side, Gear 2, Reducer configuration

work points, the torque values T_2 applied to the Ring are set accordingly to the transmission coefficient.

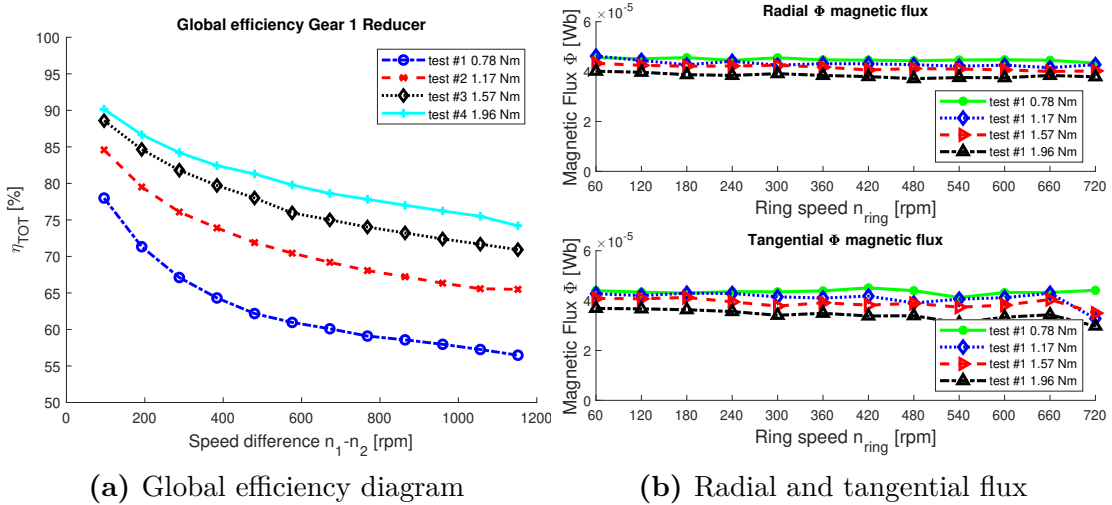


Figure 5.10: MG's performance, T_2 torque on Ring side, Gear 1, Reducer configuration

Here, too, the results are similar. The calculated performance values for Gear 1 also seem higher compared to using it as a multiplier. However, they remain lower than those obtained with the Gear 2 in the same configuration. This is certainly due to the construction problem highlighted in Figure 5.1.

Chapter 6

Dynamic tests

The dynamic operation of the MG is a topic of great interest. This is not only from the academic point of view, but also looking forward to commercialize the product for industrial applications. In addition, this type of contact-less gears have an important feature regarding the safety: it is possible to exploit the MG as a natural torque limiter in case the torque exceeds a given value, to avoid damage to the transmission in case of malfunction.

The idea of these tests is to extrapolate a time-frequency analysis in such a way to introduce an information about the temporal location of a certain oscillation contained in the signal. This involves making an acquisition during the dynamic operation of the MG. At that point, in post-processing phase, many small time windows can be acquired. Those have to be short enough to consider the quantities as static so that a frequency analyses can be performed. The FFT method makes it possible to carry out the final result of this double loop operation: a graph in which the resonances of the system are shown.

6.1 LabView control code editing

The labview code developed so far is not sufficient to make dynamic acquisitions. This can only set stationary speed or torque values on both motors indifferently.

The goal of the program modification then is:

- Being able to implement a torque or speed ramp on either motor during normal operation
- Being able to do continuous data acquisition so that even large changes can be analyzed

6.1.1 Ramp implementation

The first step in modifying the code concerns implementing a ramp. The previous code uses a real-time system with an EtherCAT communication protocol, so a loop can be nested inside the one already present which takes care of preparation of the values to be sent to the motor control. The inner loop must be faster with respect to the outer one. The outer cycle checks for variations into the input parameters every 200 ms and the time that must elapse within the small loop must be a multiple of the outer loop to ensure synchronization.

In order to simplify the view and understanding, a simplified VI is provided in Figure 6.1.

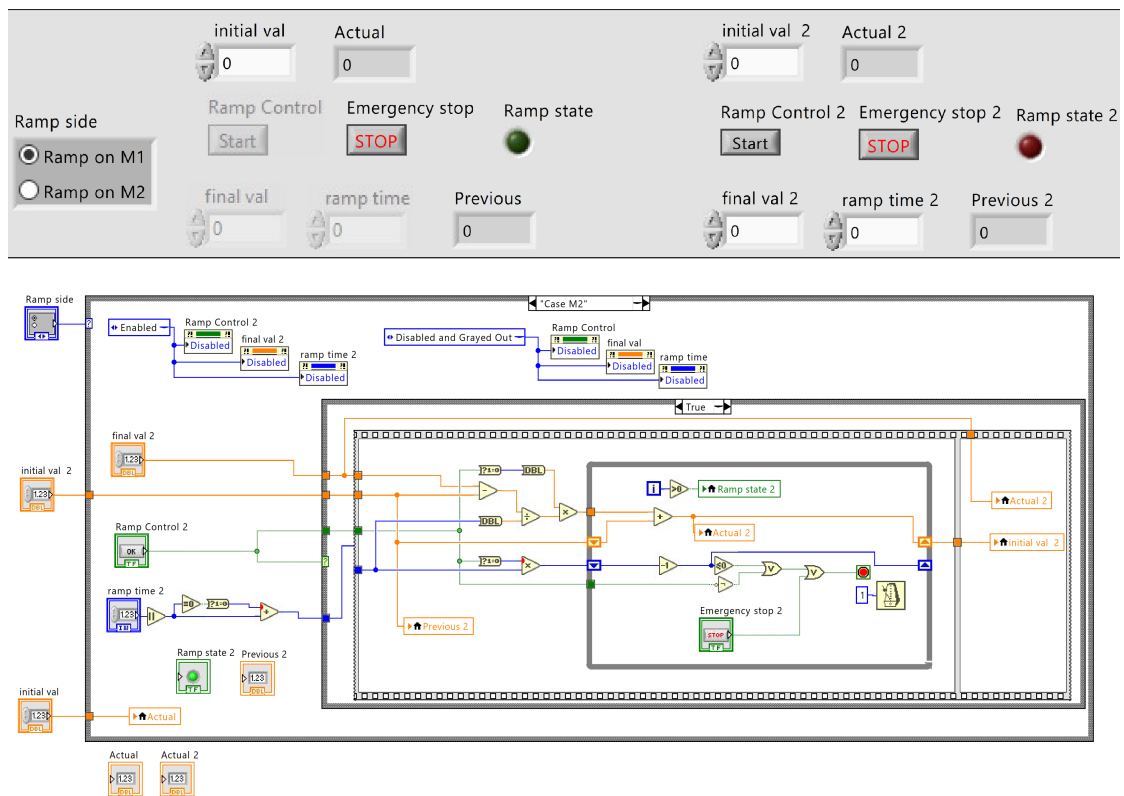


Figure 6.1: Ramp VI simple model. Front panel (up) and block diagram (down)

As can be seen, this VI is divided mainly into two parts: the one dedicated to motor 1 and the one for motor 2. The two boxes "Initial val" and "Actual" represent the two commands already present within the labview program for motor control. The whole system is based to go in and modify this input automatically so that the response is no longer stationary.

First of all in the code there is a choice of which motor to use for the ramp, one

automatically excludes the other. The next step is to choose two characteristic parameters: final value and ramp duration. These two can be entered inside "final val" and "ramp time," respectively. Once executed a ramp operation, it is possible to keep track of the starting value of the last operation thanks to the "Previous" box. Finally, start and emergency stop buttons are implemented, with attached operational status LED.

In the block diagram, you can see above the mechanisms that disable or enable the functionality of the controls based on the use case. All the controls are placed on the left side. Finally within the innermost loop is the change of the value to be set for the motor. Note that once the ramp is started the motor will change from what is written in the "initial val" box so it is absolutely necessary that when exiting the cycle (even in case of emergency stop) the last value applied be set as the starting value for static motor use. Last caveat concerns data entry: obviously, it is not allowed to enter a negative time interval. It is however possible to make negative ramps by setting values lower than the start as final value, also negative. The division of the steps is done according to the ramp time set, every millisecond to have the highest possible resolution.

6.1.2 Continuous acquisition on file

Once the code for editing data entry has been completed and made functional, there is another obligatory step: acquisition. The current code is very simple and simply takes care of inserting the data acquired from the NI system within a graph. The next step is to enlarge the code so that it is able to acquire the data continuously while writing it to a data file to be used later for the post-processing phase. The implemented simplified model is shown in Figure 6.2.

The problem of continuous data acquisition is mainly a problem of buffer size: the buffer is a very fast but at the same time a very low-capacity memory. In order to use it continuously, it must be constantly emptied. It is necessary to be careful during this process because data loss may occur during this "emptying" process. As explained in Section 4.2, it is possible to implement "circular" use of the buffer by making sure that the data acquisition clock is not lost in the meantime, which means to make use of an external clock to trigger data acquisition. By doing so, data acquisition and data flow are decoupled.

At this point it is also possible to use just a simple Express VI to cyclically append the measured data into a file. It is important to understand that this system, once started acquires data continuously until the PC's memory is exhausted, so particular care must be taken when using it. In this case, it was decided to implement a simple "Stop" button to end the acquisition process safely.

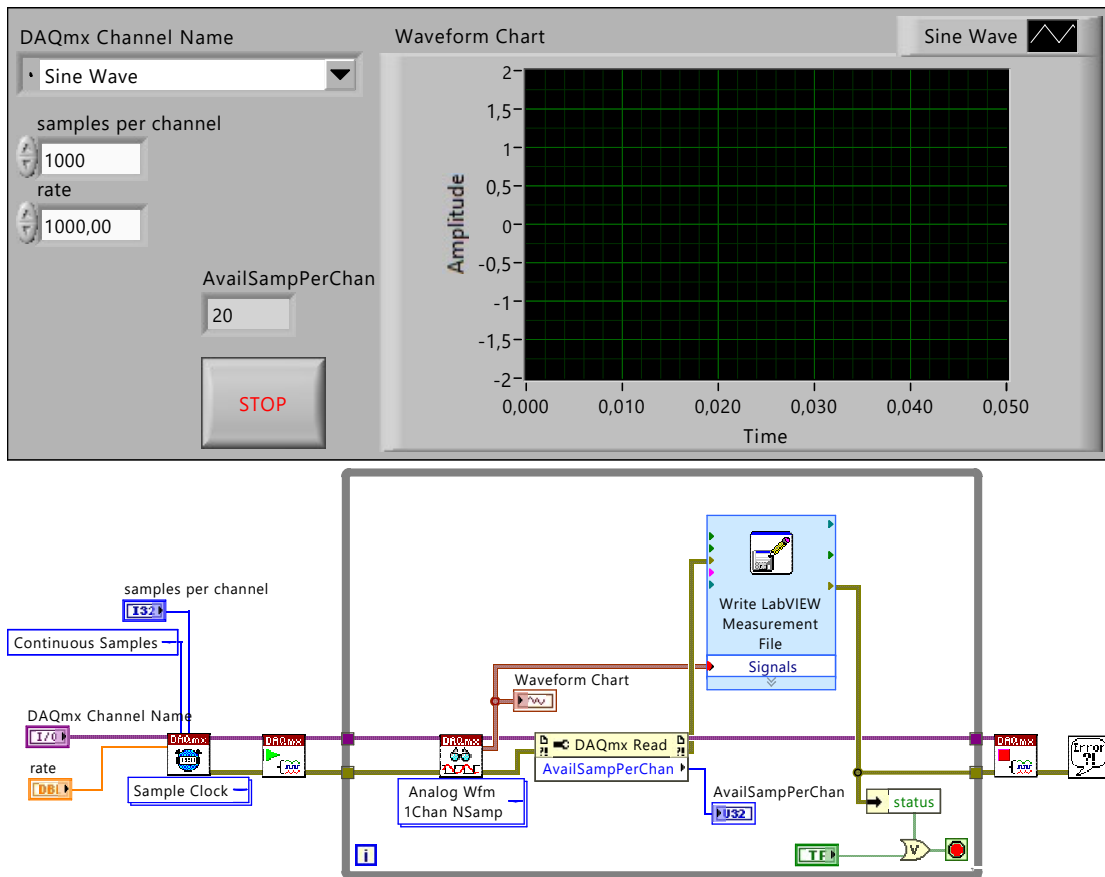


Figure 6.2: Continuous acquisition VI simple model. Front panel (up) and block diagram (down)

6.2 Expected results

As anticipated earlier, thanks to these code changes it is now possible to perform dynamic tests on the MG. Therefore, since it is not meaningful to impose at the same time a speed and torque ramp, the possibility is not allowed by the VI. By means of the ramp and step test, it is now possible to analyze the frequency response and thus the stability of the mechanism. Within a static system without acceleration, it was not possible to evaluate the inertial contribution, which was also subject to optimization during the design phase. Now with the new acquisition system, however, it is possible to derive those data even from a simple step test. Apparently the most relevant measurement is the torque one, in response to a speed ramp. By means of this test, it is possible to derive a time-frequency diagram: it is sufficient to make a long time acquisition, divide the data obtained into small

"quasi-static" portions, and analyze the harmonic contribution of the measured quantities. Using the FFT method a "colorbar" diagram can be derived. It might be expected to obtain horizontal lines, corresponding to the resonance frequencies of the system, and oblique lines, which concern the critical speed of the rotor instead.

Chapter 7

OpenReserarch

This chapter is totally dedicated to the traceability of the MG design. It is important in a scientific study the reliability of the data and the attribution of a source, so that the results can be replicate and the conclusions drawn shareable. For this reason, within this chapter, the MG design carried out at the "Politecnico di Torino" is shown in its entirety: from the geometric design parameters to the data obtained from the measurements that are in fact the proofs of its operation. The cornerstone of this chapter is therefore to give a repeatable model and the results associated with it.

7.1 Magnetic gears geometry

The PoC of MG concerns a novel method for motion transmission that no longer relies on mechanical gears but rather on magnetic-type interaction forces. The main purpose is to reduce power losses and wear on the mechanism due to mechanical components, in order to increase the global efficiency. Many models have been presented in the literature, the one analyzed in this study belongs to the category of coaxial mechanical transmissions. The reason of this choice is specifically due to the interest into maximizing as much as possible the exploitation of the magnets involved into the transmission; the primary effect therefore is an increase, compared to other literature's models, of transmitted torque density with a consequent reduction of inertia, which plays a key role for what concerns the dynamic field. [1] A specific MG configuration is analyzed in this section configured in such a way its transmission ratio between ring and sun wheel is $\tau_{r/s} = 11/7 \approx 1.571$. Geometric parameters are listed in Figure 7.1.

The inner rotor is the high-speed one, while the outer rotor runs at lower speed. Ferromagnetic poles (central rotor) are fixed and modulate the magnetic fields produced by the inner and outer rotors in such a way to create spatial harmonics

Parameter	Value
R0	22 mm
R1	30 mm
R2	36.75 mm
R3	37.75 mm
R4	48 mm
R5	49 mm
R6	54 mm
R7	62.5 mm
Axial length L_1	10 mm
Axial length L_2	17 mm
Axial length L_3	12 mm
Effective air gaps	2 mm

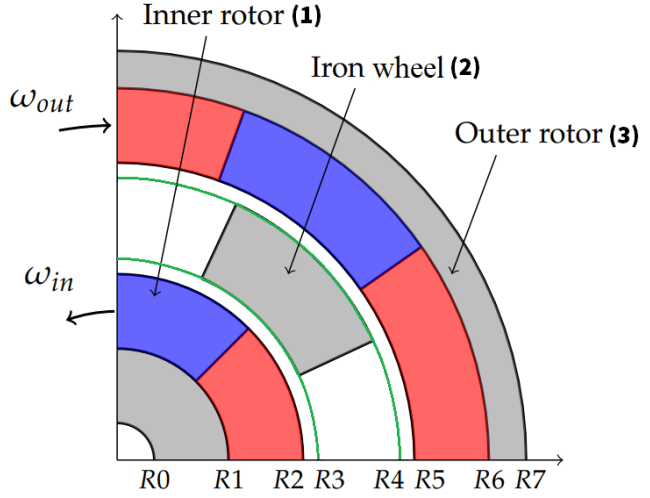


Figure 7.1: Geometric configuration of MG

all along the air gaps. The magnetic fields modulated through the steel poles interact with the magnetic field on the other side to transmit motion. Magnets' configuration is described in Table 7.1.

Parameter	Value
Inner pp n_s	7
Outer pp n_r	11
Iron poles n_f	18
Transmission ratio $\tau_{r/s}$	1.571

Table 7.1: MG magnets configuration and transmission ratio configuration

A final noteworthy aspect concerns the materials used. Chosen materials represent a key aspect for both mechanical sealing and magnetic flux linkage. The mechanical-electrical dualism is not a trivial matter: magnetic materials may be very poorly resistant to mechanical stresses; mechanically suitable materials may suffer from induced eddy currents that could lead to overheating of the object, causing it to deteriorate in efficiency or even breakage. Adopted materials are listed in Table 7.2

Of paramount importance is the use of a magnetic steel alloy for the yokes, which allows the magnet fluxes to close relatively smoothly without being excessively attenuated. In this case it is not possible to make a choice of "grain oriented" material since the flux passage direction is not set. The same applies to the wheel

Component	Material	Characteristics
Wheel yokes	M-15 Steel	$Rp_{0.2} = 620 \text{ MPa}$, $\sigma = 284 \text{ GPa}$
Magnetic poles	NdFeB	$B_r = 1080 \text{ mT}$
Carrier wheel	Resin	$\mu \approx \mu_0$
Iron poles	M270-35A	laminated, 39×foils, 0.35 thickness
Carrier bushers	Brass	$\mu \approx \mu_0$

Table 7.2: MG used materials

with ferromagnetic poles. For what concerns the carrier wheel, which contains the iron poles, is made of resin, a non-magnetic material. This is done in order to force the magnetic flux to go through the iron poles; spatial harmonics can be this way modulated within the wheels. Same holds for the bushers embedded into the wheel.

7.1.1 Magnetic wheels

The inner rotor, also called the "sun wheel", is the one that rotates at the highest speed in the system, since it has the smallest radius. Outer rotor, or "ring wheel", is slower but still torque is increased. The wheels turn in the opposite direction. Wheel rotation verse is the opposite one respect to the other, due to the intermission of the middle rotor, "carrier wheel", as shown in Figure 7.1.

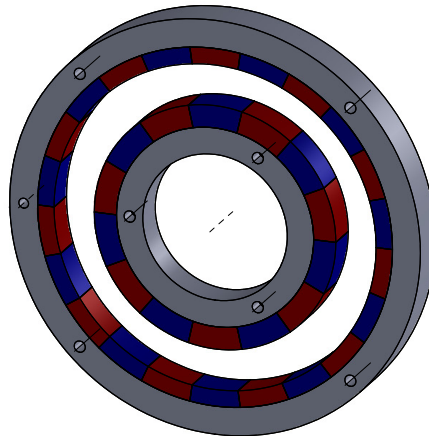


Figure 7.2: Magnetic wheels construction example

The assembled model shown in Figure 7.2 describes the totality of the aspects described so far:

- 7 pairs of magnetic poles on the inner rotor
- 11 pairs of magnetic poles on the outer rotor
- Two centrally aligned magnetic yokes on which the magnets are housed

As described in Figure 7.1, these two do not have the same axial dimension: the outer wheel is slightly larger. This is done in such a way to allow firm seating of the magnets while maintaining its same size relatively to the lower wheel. In other words, tangential distance between inner and outer magnetic poles has to be kept the same. Complete dimensioned tables are provided in the Appendix A.

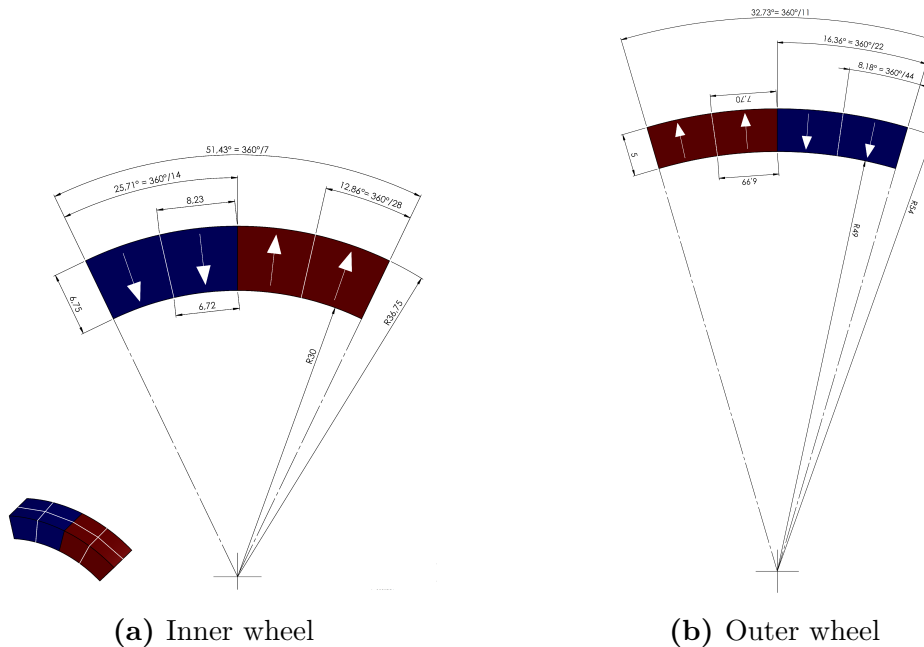


Figure 7.3: Magnetic wheels dimensioned table and magnet partitioning

The magnetic poles are distributed over the entire circular section as shown in Figure 7.3. The number is fixed so simply divide the circumference by 7 and by 11 to know the angular portion of a polar pair. The radius of the wheels at the same time is known so it is immediate to know the actual amount of magnet needed.

Another key construction aspect concerns magnets: it is very difficult to "bend" magnetic material while maintaining its characteristics. The countermeasure adopted in Figure 7.3 is to partition the intended volume of magnetic material into smaller smaller portions easier to craft.

7.1.2 Ferromagnetic wheel

The middle rotor has the task of modulating between the two magnetic wheels containing it. Contained within it are the laminated ferromagnetic poles described in Figure 7.4. For mechanical sealing reasons, the ferromagnetic poles have been encased inside the resin wheel. This caused the effective air gap between the wheels seen by the magnetic flux to increase.

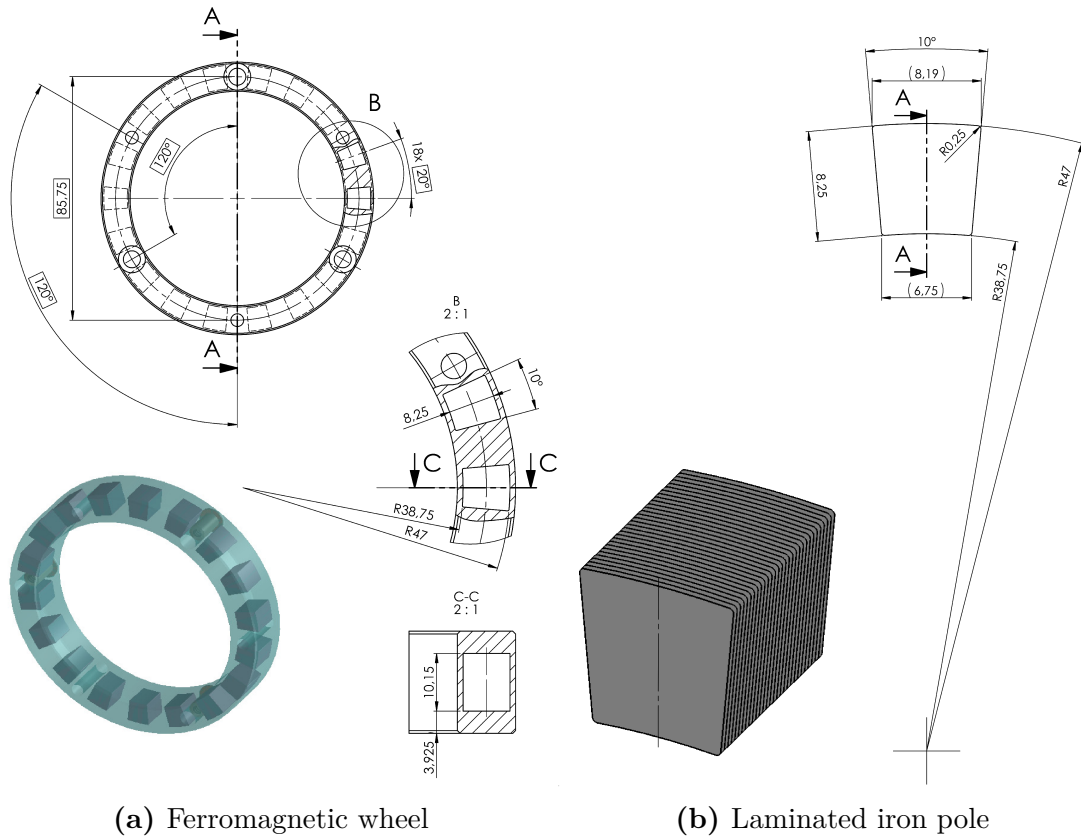


Figure 7.4: Carrier dimensioned table and ferromagnetic poles lamination

To limit magnetic flux leakage into air, the distance between the wheels should be as small as possible. For purely constructional reasons it was not possible to maintain the 1 mm air gap expected, as can be seen in Figure 7.4. Effective air gap is therefore equal to 2 mm between the wheels.

On the other hand, this is the longest wheel axially among the three. As shown in Table 7.1, the thickness of this wheel is greater than that of the other 2. This has a twofold advantage: the poles are able to collect the flux that would otherwise have been dispersed laterally and at the same time they saturate less easily. Neither

to say that eddy currents have to be taken into account, which implies the iron poles lamination.

To summarize, referring to Figure 7.4, it can be said that:

- The carrier has 18 ferromagnetic poles, composed of 39 foils each 0.35mm thick.
- Total wheel length is equal to 17mm, 5mm longer with respect the magnetic wheels
- Effective air gap relatively to magnetic flux is of 2mm, for mechanical reasons
- Plastic non-magnetic material is used to encapsulate the iron poles

Complete dimensioned tables are provided in the Appendix A.

7.2 FEMM model

Complete dimensioned tables useful to build the model are provided in the Appendix A.

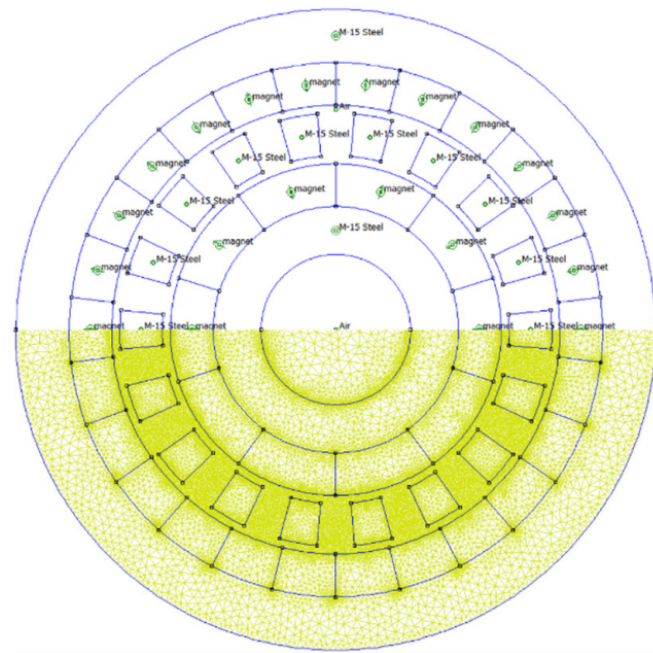


Figure 7.5: 2D planar finite elements MG model mesh plot

Once the geometry is completely known this can be parameterized and studied using the finite element calculation software Femm for electromagnetic problems.

This is a crucial step since it is the step immediately preceding the construction of the prototype. Within this last control step, it must be verified that the design has been done correctly and that all the chosen parameters are correct. It is furthermore an important step in order to understand the actual potential of the MG such as torque density and magnetic flux density.

As can be seen in Figure 7.5 a 2D planar model is proposed. For this to be as reliable as possible, it is necessary to include within the software the specifications of the materials that make up the mechanism: from the steel yokes, to the magnets hooked onto them, to the ferromagnetic poles that modulate the flux. For what concerns non- magnetic materials it is not necessary to implement a custom magnetization curve: those behave very similarly to air. List of the materials is provided in Table 7.2.

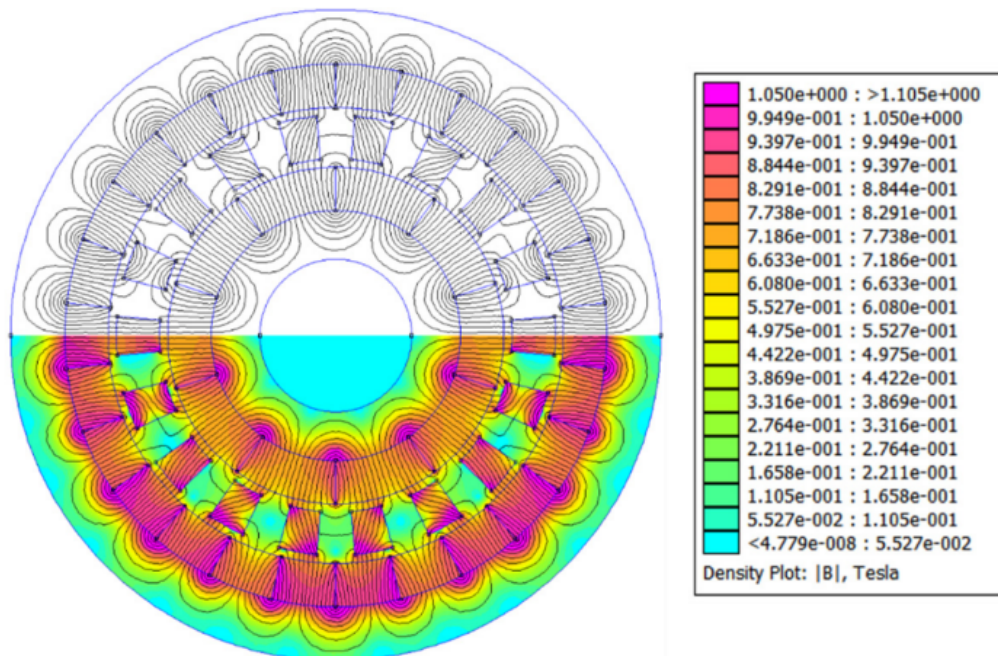


Figure 7.6: 2D planar finite elements MG model solution

The most difficult part of these kinds of models is making a good mesh. This must be a compromise between numerical burden on the computer and at the same time accuracy of the results. As shown in Figure 7.5, the mesh made is mixed: at the points of greatest interest, such as air gaps and edges, it is finer; for the other inner points it is more relaxed. Doing so it is given a very good approximation of the operation in a relatively short time. This aspect is also crucial from an optimization perspective, for which it may be necessary to iterate the same model

many times to obtain satisfactory results.

The solution of this simulation is shown in Figure 7.6. In the upper part of the figure, the flux lines and their passage are highlighted in blue. In the bottom part, via a colorbar, the saturation level of the magnetic materials is shown. As was desirable, the points most prone to saturation are the edges between the magnets and the ferromagnetic poles. It can be appreciated, however, that it appears from the simulation that the Sun wheel magnets are less stressed than the Ring. At the same time, as was desirable, the steel yokes appear to be affected only in the portions most in contact with the magnets.

Results shown in Table 7.3 were carried out by finite elements simulation.

Femm simulation results	Value	Unit
Torque inner rotor (sun) T_{sc}	[2.09 3.02]	Nm
Torque outer rotor (ring) T_{cr}	[5.44 4.74]	Nm
Torque carrier T_c	-[7.53 7.76]	Nm
Weight $m_M G$ (single stage)	0.62	kg
Torque density T_ρ	3.36	Nm/kg

Table 7.3: Magnetic gear femm simulated capability results

7.3 Measurements

All measurements data are available on the *PoCMagnGearbox* GitHub repository. [18]

The results of the acquisitions of Torque versus Velocity and Magnetic Flux versus Time are presented in this section. For the former, a National Instruments acquisition system and electro-mechanical sensors were exploited; for the latter, a digital oscilloscope connected to flux coils placed around the ferromagnetic poles was used. A total of six coils were placed on three ferromagnetic poles, spaced of 120° each. On each pole are then applied two coils: one to evaluate the Radial Flux, with respect to the rotating axis of the mechanism, and one for the Tangential Flux.

This section describes the tests performed on the transmission ratio described in Section 7.1. It will henceforth answer to the name of Gear 2.

First of all a consideration about the MG's configuration: it is not possible to impose either side of the gear only speed or only torque because this would make the system hyperstatic. Therefore, what is typically done is to impose Torque on one side, and a set of speed values on the other side. This makes it possible to

analyze the operation of the transmission whether it is used as a torque multiplier or reducer. Before proceeding, it is deemed necessary to define a wording convention to be able to recognize the side being discussed.

- **Torque/Speed Multiplier:** Torque T_1 is applied on the sun side, Speed ω_2 on the ring side.
- **Torque/Speed Reducer:** Torque T_2 is applied on the ring side, Speed ω_1 on the sun side.

To avoid confusion, Table 7.4 is provided, values imposed relatively to the gear and to the corresponding operating point based on the multiplier and reducer configuration are explained in detail.

	Multiplier		Reducer	
	Ring Speed [rpm]	Sun Torque [Nm]	Sun Speed [rpm]	Ring Torque [Nm]
Gear 2	60	0.5	94.3	0.78
	120	0.75	188.6	1.17
	180	1	282.9	1.57
	240	1.15	377.1	1.96
	300		471.4	
	360		565.7	
	420		660	
	480		754.3	
	540		848.6	
	600		942.9	
	660		1037.1	
	720		1131.4	

Table 7.4: Table of the DOE tests performed respectively to the MG possible configurations

Two types of tests are carried out: no-load and load tests. No-load tests are critical to characterize the leakage contributions within the mechanism. The no-load condition is assumed to be the one for which the magnets are subjected to the least load. Since the energetic loss contributions due to the magnets can be neglected, the torque losses can be considered to be due to mechanical friction on the bearings.

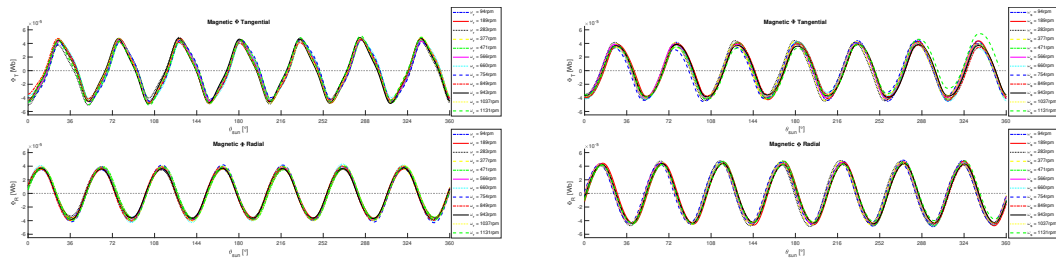
7.3.1 Magnetic Flux Acquisition

Before proceeding with the presentation of test results, it is important to make a small digression regarding magnetic fluxes. The waveform and peak flux value are

indicative of the operating state: the lower the peak, the greater the "magnetic" load the magnet must carry; the more distorted the waveform, the greater the losses due to harmonics.

The measured fluxes are periodic, since the rotating magnets are always the same. It is therefore possible to have a 360° electrical view of the state of the fluxes during operation.

Figure 7.7 shows the measured Magnetic Flux on Gear 2. Two cases are reported as example: the no Torque load applied case and the high Torque load one. The no-load case should correspond to the condition of maximum flux peak value and lowest harmonic distortion for both radial and tangential flux. On the other side, the high load case should imply a lower peak value and an higher harmonic distortion condition.



(a) No Torque load applied

(b) High Torque load applied

Figure 7.7: Radial and Tangential Flux, Gear 2, Reducer configuration

7.3.2 No-load tests

No-load tests are crucial to the study of the mechanism since they give an idea of whether the energy loss contributions belongs to the electromagnetic or mechanical world.

The mechanical contribution to system losses is expected to predominate, therefore it might also be dependent on the used MG's configuration. This is due to the different radial size of the two transmission wheels: in order to be firmly engaged on an axis, but at the same time free to rotate, bearings must be used. It is possible to decouple the loss contributions of the two bearings by exploiting a property of the no-load test: by imposing speed on one side and zero torque on the other, the torque transducer placed on the speed-driven side will always see zero torque. For example: applying speed ω_1 on the Sun side, the torque measured on the same side must be 0 (by definition); on the Ring side there is no torque T_2 imposed, so the torque transducer measures a torque that must be due to losses on the Ring side bearing.

The larger the bearing, the higher the measured loss contribution on its "side" is expected to be. Since the Ring wheel' diameter is larger with respect to the Sun wheel's one, the measured Torque loss on the former should be higher.

In Figure 7.8, MG operation in multiplier configuration is shown. Since no resistant torque applied in this test, so the resistant torque seen in the graph is "lost" within the mechanism. In other words, the "no-load" losses of the mechanism are shown. The following tests were performed: up, down, up and up.

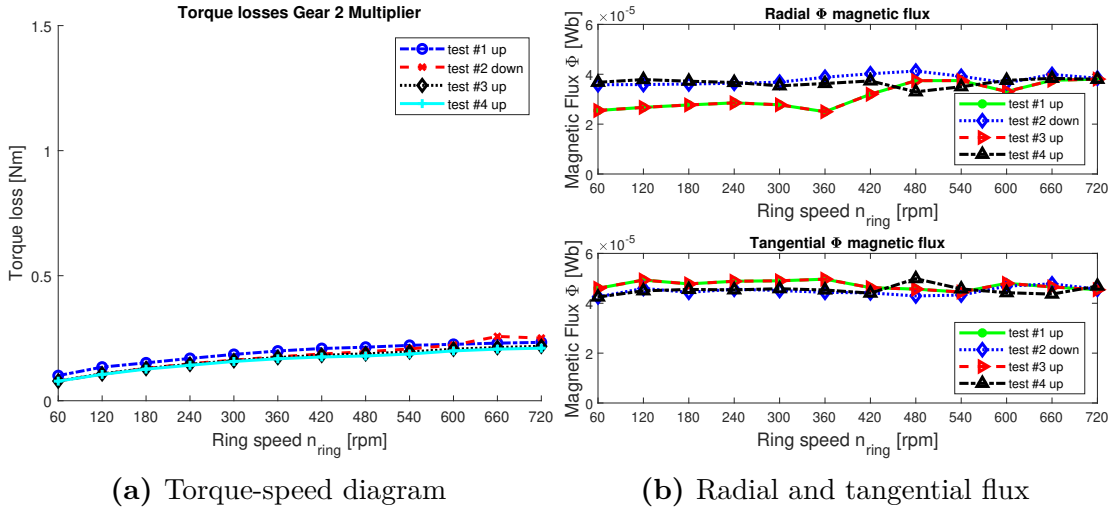


Figure 7.8: Measured results, No-load applied, Gear 2, Multiplier configuration

As can be seen, at each iteration, the lost torque curves "goes down." Flux follows the same pattern, although in a less pronounced manner. This variation can be attributed to the change in temperature within the mechanism: the further into the thermal regime one goes, the lower the losses seem to be. Radial Flux is a bit messy on test #1 and #3, above all on lower values. However, the discrepancies measured during some initial tests seem to fall back during the next ones.

It is then time for measurements in reducer configuration, Gear 2 results are shown in Figure 7.9. In this case, bearing losses appear to be higher with respect to the previous case. This is because, as anticipated earlier, it's been analyzing leakage contributions on a larger diameter bearing in this case. Growth in bearing size results in greater losses.

The greater amount of testing on this configuration gives a wider range of results to analyze. With regard to torque, it seems in this case that the losses are in contrast to previous cases. However, points of non-linearity are seen on the final measurements, this would suggest that this trend of increasing losses with testing was caused by a problem on the bearings that led to seeing more losses. Fluxes on the other hand are very stable. Both around $50\mu Wb$, they seem to be slightly

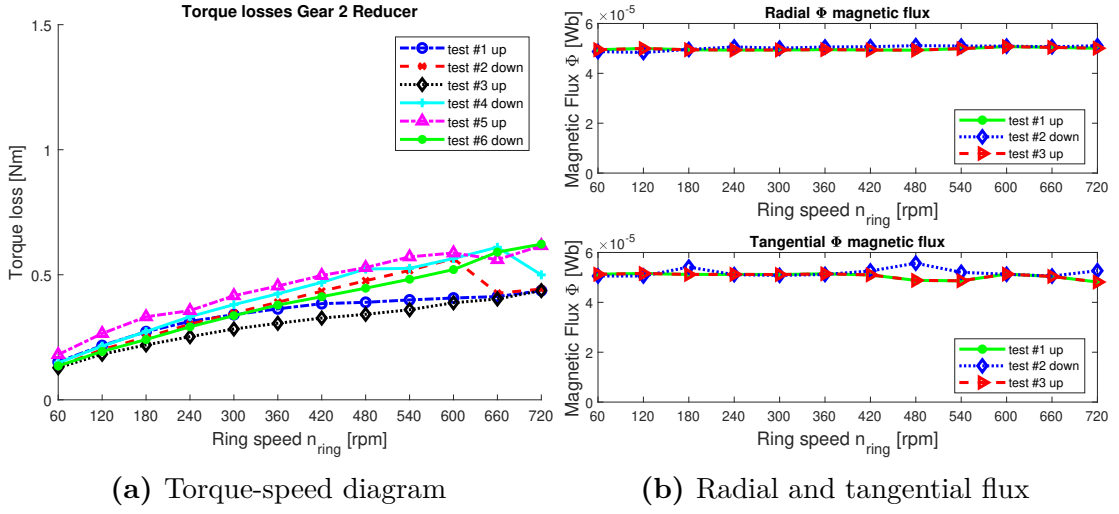


Figure 7.9: Measured results, No-load applied, Gear 2 Reducer configuration

affected by variations on the final measurements.

7.3.3 Loaded tests

In these load tests, the approach used is different. The torque-speed curve measured on either side of the MG is no longer very indicative of its efficiency during operation. Therefore, global efficiency plots of the mechanism derived from the formula (7.1) are shown in this section. Ring speed is as well no longer relevant, but rather the efficiency plot might be based on the speed difference between rotors.

$$T_{out} \cdot \omega_{out} = \eta \cdot T_{in} \cdot \omega_{in} \quad \longrightarrow \quad \eta = \frac{T_{out} \cdot \omega_{out}}{T_{in} \cdot \omega_{in}} \quad (7.1)$$

It remains relevant and useful instead the analysis of the magnetic fluxes within the MG. From an energy perspective, it is not possible to exclude the loss contribution of the magnets within the transmission, since a second magnetic component in addition to the flux density B is not known. The behavior of magnets in general is known: given a demagnetization curve and a load curve, they can be related to estimate the behavior under load of the magnet and therefore of its value of supplied induction B under load. This means that as the working conditions of the magnet change, assuming the same cross section area of the sensing coil, the measured flux density B_{meas} may vary. If demagnetization curves of the magnets were available, it would be possible to trace the energy lost by knowing only the induction; since only the residual induction is known for this particular model of magnets, this is not possible.

Therefore, in this section tangential and radial flux of the magnets are analyzed in relation to the overall system efficiency. It is expected that the greater the strain imposed on the MG, the lower the flux detected, accordingly to its demagnetization curve. At the same time, the greater the power transmitted, the lower should be the influence of losses within the system, assuming them to be nearly constant.

Performed tests are described in the DOE, Table 7.4. Figure 7.10 reports the first results obtained. Measurements were performed by setting a certain Torque value, refer to the figure, and acquiring subsequent values of speed. In this case torque T_1 is applied on the Sun Wheel and speed ω_2 on the Ring Wheel.

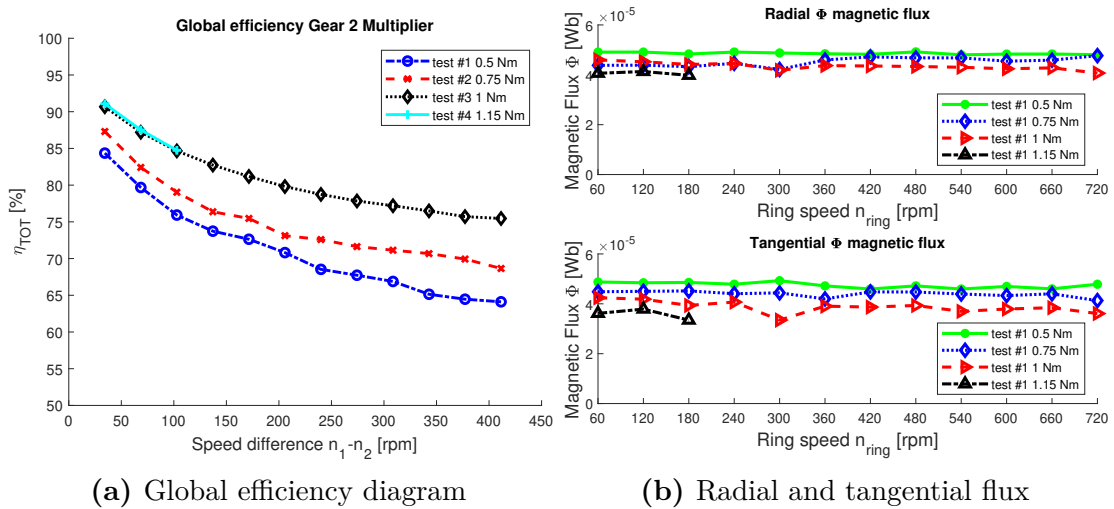


Figure 7.10: MG's performance, T_1 torque on Sun side, Gear 2, Multiplier configuration

As can be easily seen, as the applied load increases, the efficiency goes up significantly. This is because, as mentioned, bearing losses can be considered almost constant. The limiting curve seems to be reached with the last two tests with the higher torque, in fact the efficiency points seem to be overlapping. The fluxes also seem to behave as expected: moving between values on the order of $50 \div 40 \mu Wb$, they drop slightly as the load increases. This indicates that the working point of the magnets is moving along the demagnetization curve.

In contrast, the opposite configuration is now presented. The MG's use as a torque reducer involves applying a T_2 on the Ring and ω_1 on the Sun. It is expected to find congruent results with respect to the previous case, since the chosen working points are equivalent. Case with Gear 2 applied is shown in Figure 7.11.

In this case the maximum efficiency obtained seems to be higher with respect to the multiplier's case. The monotone decreasing trend is similar to what obtained previously. Same decreasing situation for fluxes: as the load increases the flux

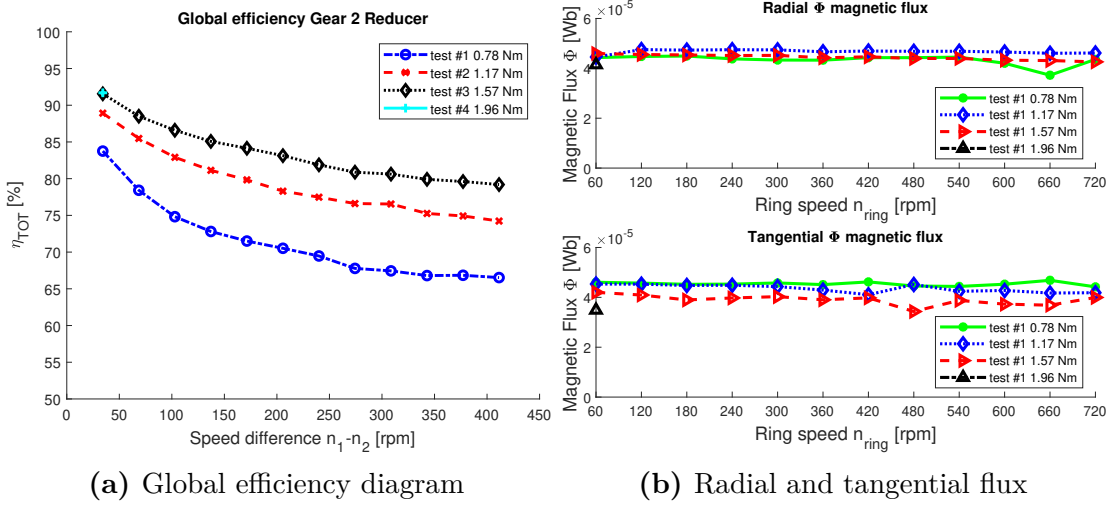


Figure 7.11: MG's performance, T_2 torque on Ring side, Gear 2, Reducer configuration

decreases following the magnets' demagnetization curve.

Finally, the influence of temperature on the induction drop of the magnets is considered negligible in these load tests. No-load tests were lead before applying the Torque load in order to "preheat" the mechanism. Hence it is assumed that the temperature remained constant during the test, barring specific overheating that may have occurred during the trial.

7.4 Conclusions

In this article, a novel configuration of a concentric-type magnetic gear is presented. It is a challenging technology which exploits the method of transmitting mechanical quantities of the wheels, but at the same time improves the flux by introducing magnets. This new method of power transmission, thanks to the contact-less operation, have high efficiency and reliability, intrinsic overload protection and very few maintenance issues. The designed configuration makes use of three wheels: a magnetic Sun and Ring and a ferromagnetic Carrier in the center to modulate the two emitted fluxes. The construction aspects, parameters, and material characteristics from any point of view are described in order to make the prototype replicable in construction and results. Purely constructive aspects which involved a limitation of the functionalities with respect to the designed model are also analyzed. A finite element analysis is described, along with the mesh method, geometry and material properties implemented. This made it possible to carry out analytical results upon which the construction of a test bench was based. Once

the data acquisition system was set up, measurements were made, the results of which are reported and made public. The tests were carried out following a precise DOE, aimed to investigate the actual potential and limitations of the mechanism produced. Finally, an analysis of the data acquired in the load and no-load tests of the prototype is provided. Magnetic gear technology is still quite immature and still needs several stages of validation and optimization before it could be asserted in the industrial world. To date, the high costs of design and materials exploited do not make it easily marketable, but this technology is certainly a warranty for a world moving more and more towards sustainability and ultra-high-efficiency systems.

Chapter 8

Conclusions

Multiple aspects were analyzed in this work. Starting with theoretical ones related to the mechanism of operation of the MG, following with considerations regarding the prototype on which to carry out the studies.

It went then deeper with the actual design of the test bench in every aspect: from the choice of sensors, to the electrical wiring and the choice of acquisition systems. An overview regarding the main concepts that dominate data acquisition within a National Instruments system could not be missed, with all the considerations kept while writing code for motor control and data capture.

Following to a write-up of the DOE, static operation tests of the MG were therefore carried out. By doing so, it was possible to determine the actual operation of the transmission, isolate its loss contributions, and derive overall performance values. Few possible new areas of study for the prototype are also presented. The importance of a dynamic analysis is discussed and furthermore a modification of the LabView code, capable to perform dynamic tests on the MG, is proposed.

The article is concluded by presenting an OpenResearch Document. The development of Magnetic Gear is still in its infancy, so it is necessary to put up a united front with other teams of developers to move the project forward and ensure that as many optimization and validation steps as possible are taken. On those basis, it is important to ensure the repeatability of the study and the reliability of the data source.

The aim is to make this innovative method of motion transmission marketable as soon as possible so that everyone can benefit from it.

Appendix A

PoC MG construction tables

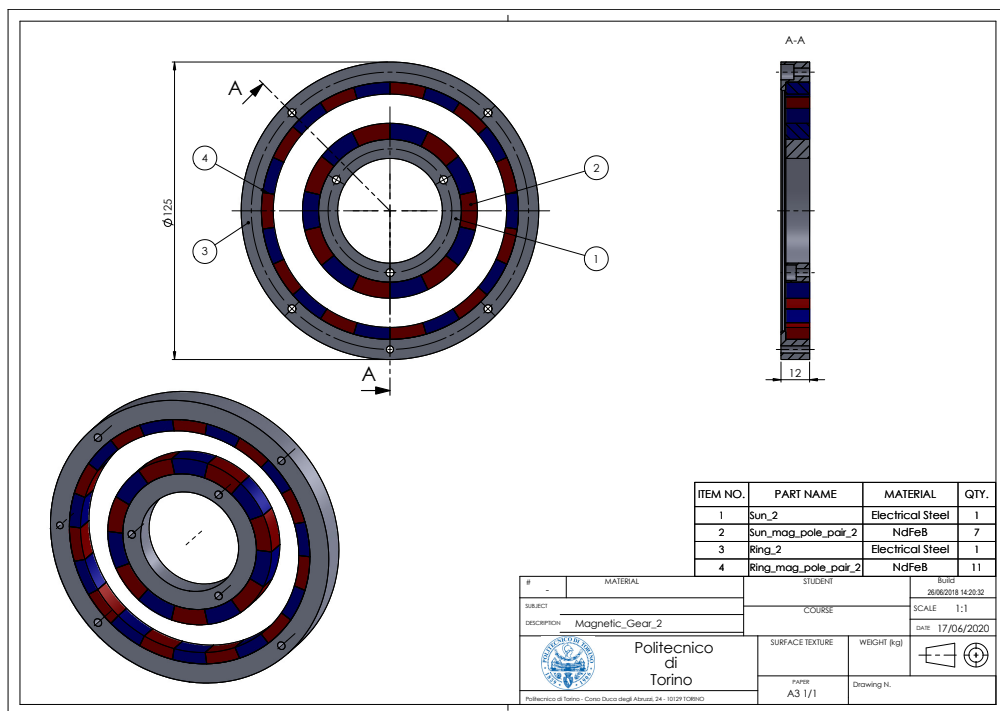


Figure A.1: PoC Magnetic Gear dimensioned tables page 1

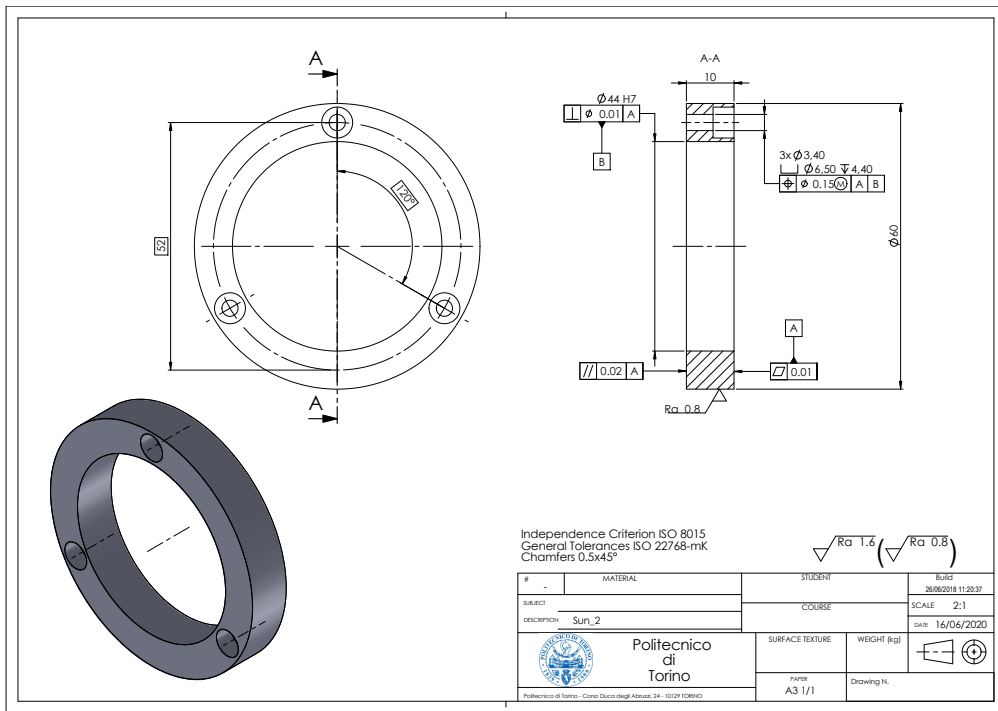


Figure A.2: PoC Magnetic Gear dimensioned tables page 2

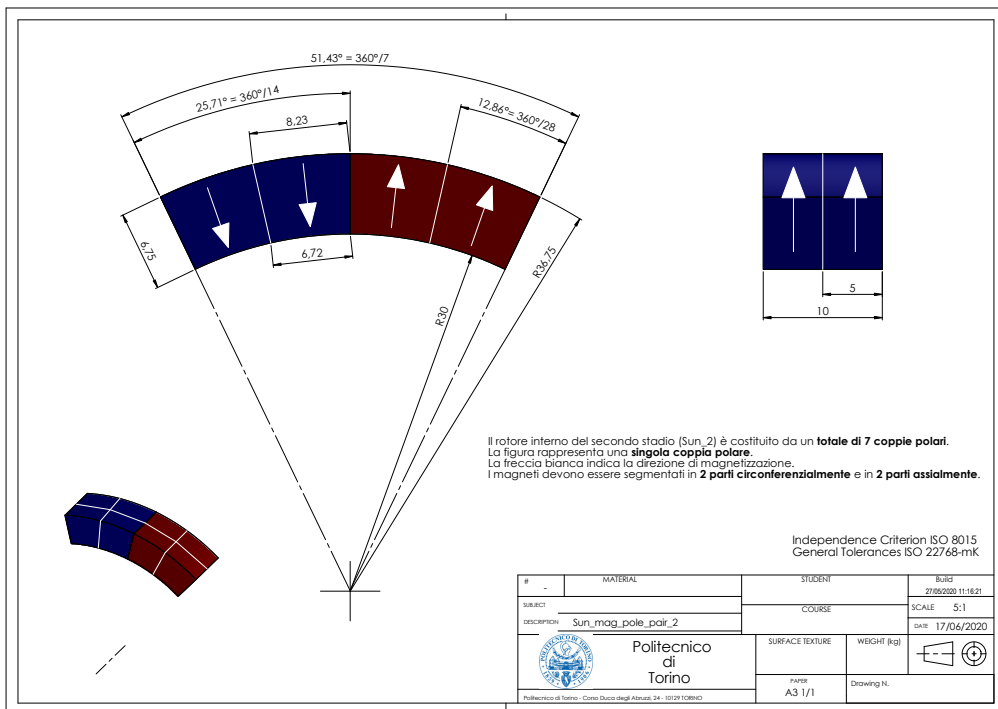


Figure A.3: PoC Magnetic Gear dimensioned tables page 3

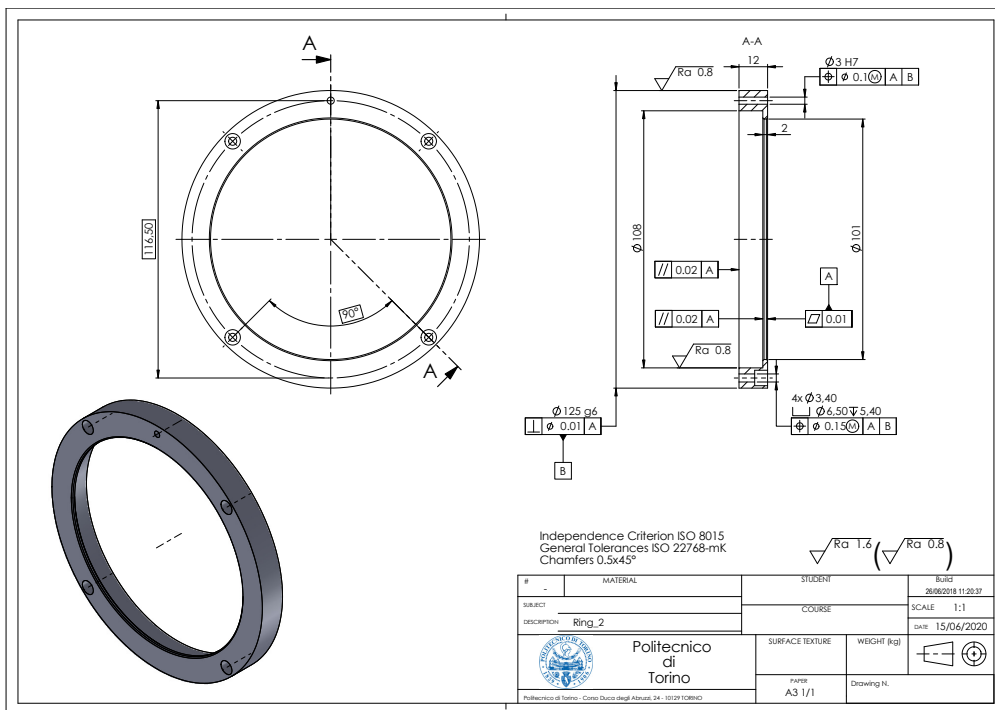


Figure A.4: PoC Magnetic Gear dimensioned tables page 4

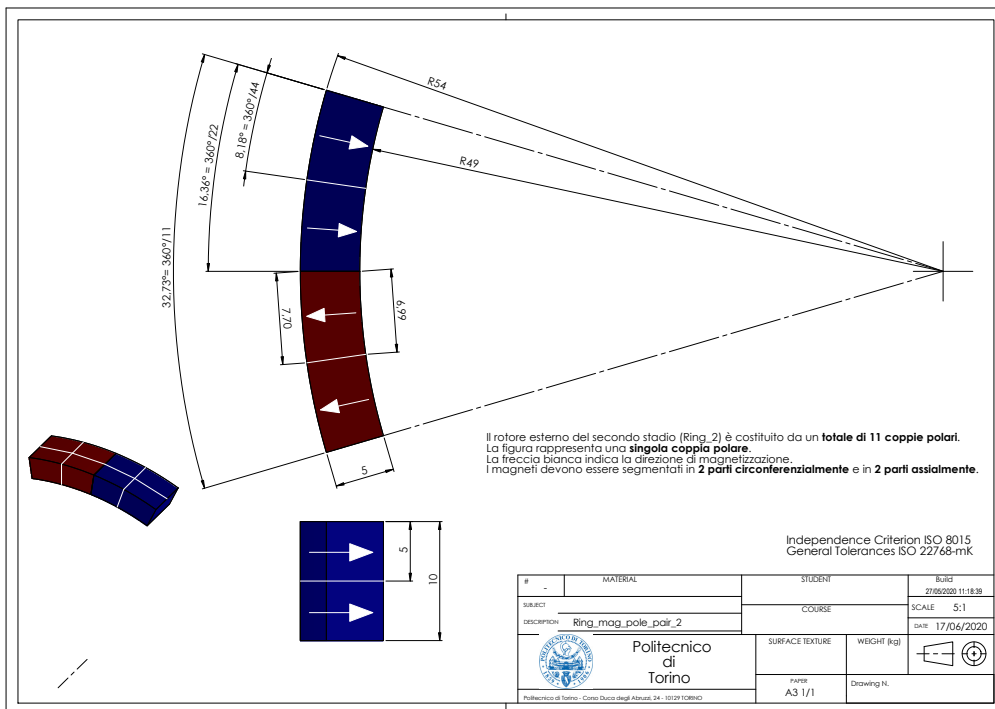


Figure A.5: PoC Magnetic Gear dimensioned tables page 5

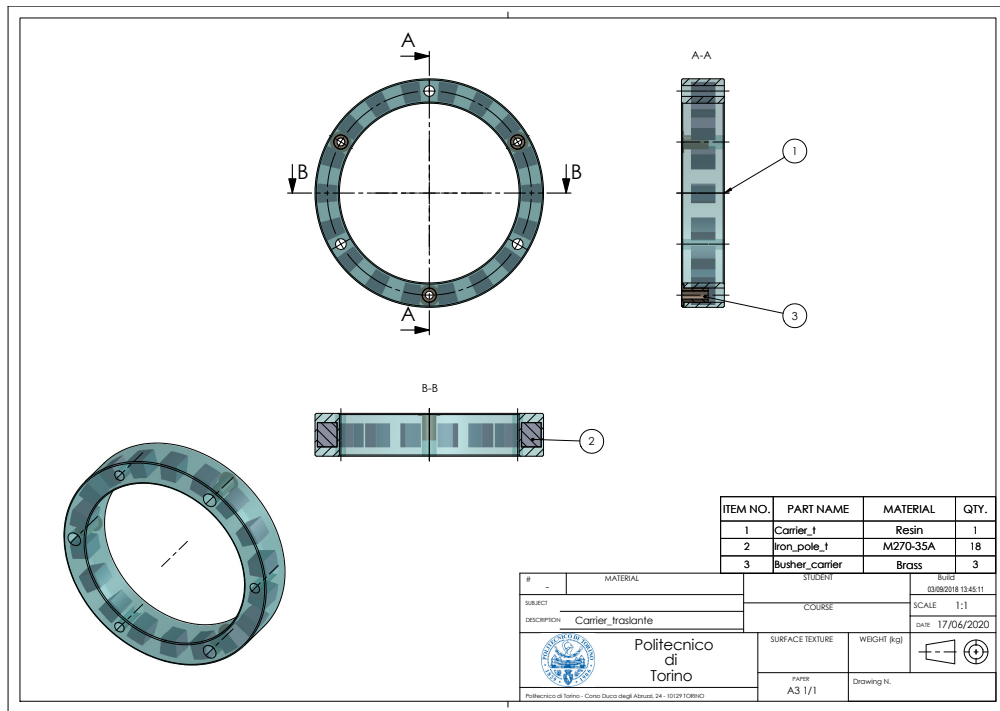


Figure A.6: PoC Magnetic Gear dimensioned tables page 6

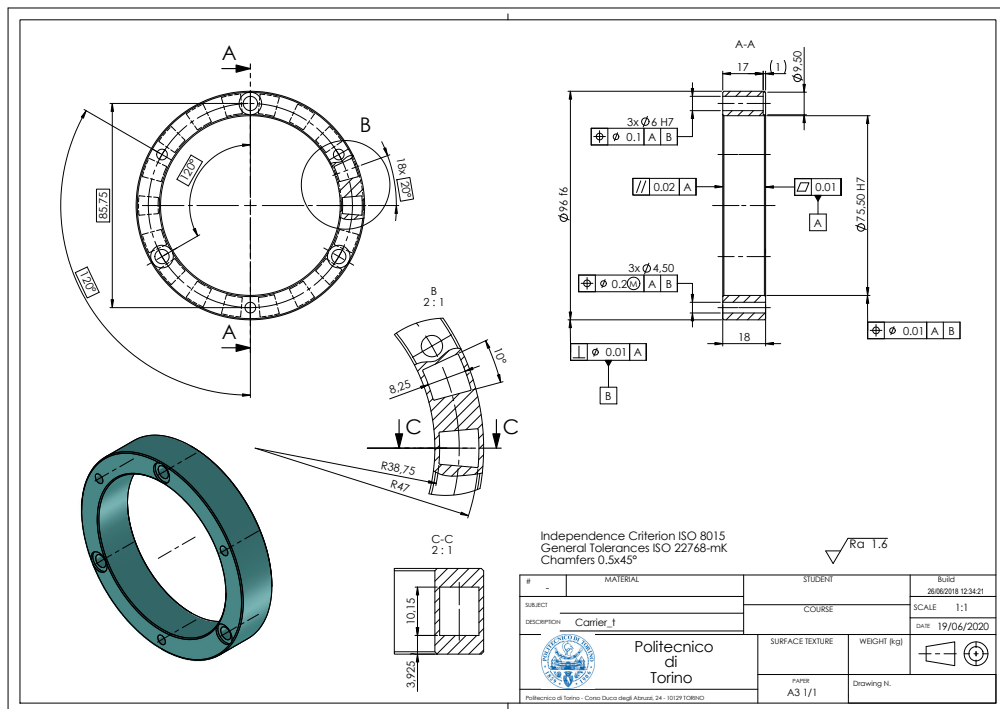


Figure A.7: PoC Magnetic Gear dimensioned tables page 7

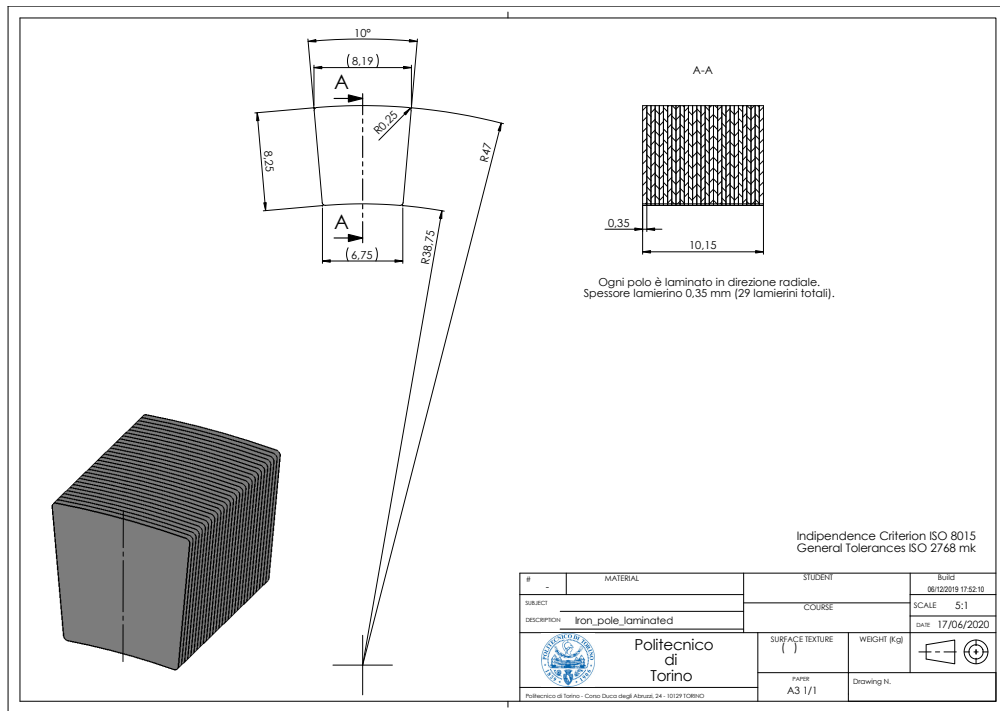


Figure A.8: PoC Magnetic Gear dimensioned tables page 8

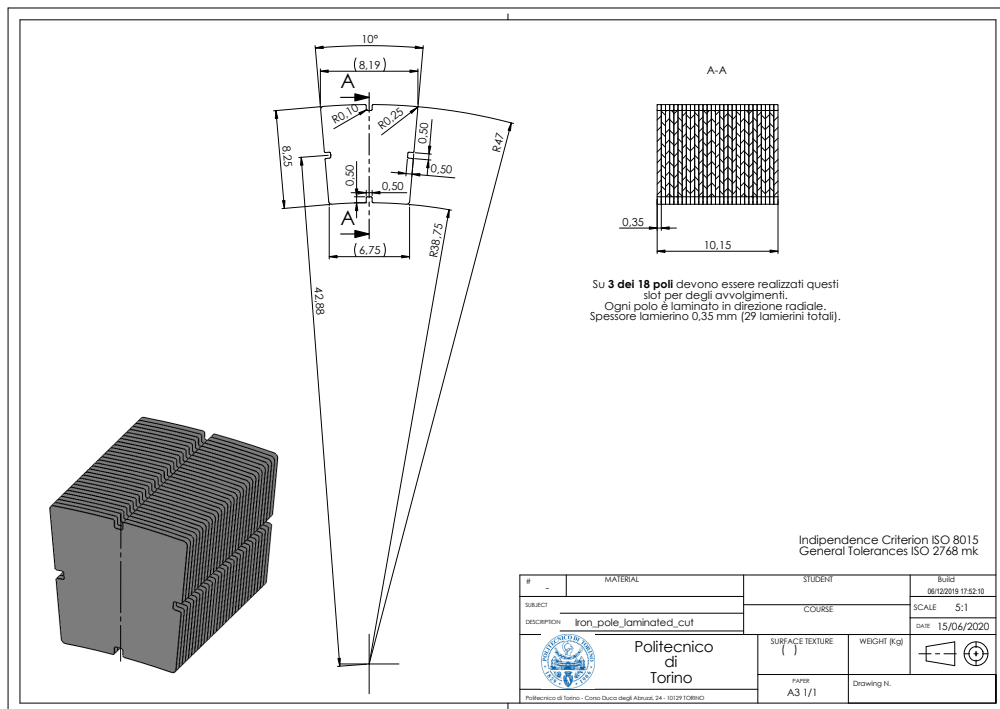


Figure A.9: PoC Magnetic Gear dimensioned tables page 9

Appendix B

Software versions

- NI LabView 2018
- SolidWorks 2015
- i-project 6
- Matlab R2019a
- Autocad Electrics 2020
- Arduino IDE 1.8.10
- Femm 4.2

Bibliography

- [1] S. Gerber P.M. Tlali R-J Huang. «Magnetic Gear Technologies: A Review». In: *IEEE* (2014) (cit. on pp. 2, 67).
- [2] Howe D. Atallah K. Calverley S.D. «Design, analysis and realisation of a high-performance». In: *IEEE Proc. Elect. Power Appl.* 151(2) (2004) (cit. on p. 5).
- [3] K. Atallah and D. Howe. «A Novel High-Performance Magnetic Gear». In: *IEEE Proc. Elect. Power Appl.* 37(4) (2001) (cit. on p. 6).
- [4] C.Ragusa M.Filippini P.Alotto. «Magnetic Loss Analysis in Coaxial Magnetic Gears». In: (Nov. 2019) (cit. on pp. 9, 10).
- [5] Maurizio Repetto Luca Dimauro Elvio Bonisoli. «Magnetic gear prototype and test bench». In: (Apr. 2020) (cit. on p. 10).
- [6] David Meeker. *Finite Element Method Magnetics User Manual*. URL: <https://www.femm.info/wiki/manual> (cit. on p. 12).
- [7] L.Dimauro V.Cirimele. «Multi-objective Optimisation of a Magnetic Gear for Powertrain Applications». In: (2019) (cit. on p. 14).
- [8] *SVTM A 03 servo motors*. 03-11.5-107. Rev. 2.3. Servotecnica. May 2019 (cit. on p. 18).
- [9] *Servo Drives KE/KW, Compact Power Supplies KE, KES, KEN, Compact Inverters KW, KWD*. pdk 028932. AMKASYN. 2019 (cit. on p. 19).
- [10] *Torsiometro ad albero*. T21WN. part n. B04806-03-I00-01. HBM (cit. on p. 21).
- [11] *RLS LM10 incremental magnetic encoder system*. LM10D01-15. Rev. 15. Renishaw. May 2018 (cit. on p. 22).
- [12] *42 mm sq. stepping motors*. 103H5208-5210. Rev. C. Sanyo Denki Co. Ltd. Aug. 2012 (cit. on p. 26).
- [13] *Stepping divers*. US1D200P10. Sanyo Denki Co. Ltd. (cit. on p. 26).
- [14] *Correlated digital module for cRIO*. NI9411. National Instruments (cit. on p. 37).

- [15] *Digital input for 24V signals module for cRIO*. NI9421. National Instruments (cit. on p. 37).
- [16] *Analog input module for cRIO*. NI9205. National Instruments (cit. on p. 37).
- [17] *Data Acquisition Using NI-DAQTMmx and LabVIEW*. 326543A-01. LabView 2016. National Instruments. Jan. 2017 (cit. on pp. 38–40, 42).
- [18] La Bella Nicola, Dimauro Luca, Oggeri Stefano, Repetto Maurizio, Bonisoli Elvio, and Squillari Paolo. *Open Research Magnetic Gear Polito PoC*. Version 1.0. Apr. 2022. URL: https://github.com/PoCMagnGearbox/Polito_PoC_Magn_Gearbox_Measured_Data.git (cit. on p. 74).